Technische Universität München

Lehrstuhl für Nanoelectronik

Modeling of Leakage Currents in High-k Dielectrics for Future DRAM Application

Dan Horia Popescu

Vollständiger Abdruck der von der Fakultät für Elektrotechnik und Informationstechnik der Technischen Universität München zur Erlangung des akademischen Grades eins

Doktor - Ingenieurs

genehmigten Dissertation.

Vorsitzender:	Univ.-Prof. Dr. sc. techn. Gerhard Kramer
Prüfer der Dissertation:	1. Univ.-Prof. Paolo Lugli, Ph.D.
	2. Univ.-Prof. Dr. rer. nat. Franz Kreupl

Die Dissertation wurde am 08.01.2015 bei der Technischen Universität München eingereicht und durch die Fakultät für Elektrotechnik und Informationstechnik am 14.07.2015 angenommen.

To my parents and friends

Abstract

For the last 50 years, the continuous downscaling of integrated circuit devices has led to ever higher packing densities and thus smaller and faster electronic components. But the success of integrating ever more CMOS devices on shrinking wafer sizes has to be firstly attributed to the unique properties of silicon and its native oxide SiO_2. During recent years however, some technological limits have been reached and the semiconductor industry was forced to search for new material systems in order to keep the miniaturization trend - coupled with cost reduction and performance optimization - going.

One specific problem that requires attention is the search for adequate high-*k* dielectrics to replace the silicon oxide, both for the transistor and capacitor applications, since undesired leakage currents through these new thin film dielectrics represent a severe problem. In this paper we have investigated the leakage current vs. voltage characteristic of high-*k* thin film capacitors over a large temperature range. Fabricated samples, consisting of a 10 nm thin $SrTiO_3$ (STO) layer as a dielectric material and $SrRuO_3$ (SRO) as electrodes, have been examined. Employing a novel, fully self-consistent, kinetic Monte Carlo simulator, which takes into account trap assisted tunneling and trap relaxation effects, we analyze the behavior of the leakage current for the varying temperature and bias conditions.

Once validated, our simulation model offers useful insights in the underlying physics and helps us identify the main processes responsible for the large reported leaking currents. A sensitivity analysis is performed to determine the impact of different material parameters on the leakage current and several solutions for reducing the undesired currents are presented. Key parameters that are otherwise hard to measure with experimental methods have been extracted; they serve then as input for our modified drift-diffusion (DD) simulations. Finally, within the DD framework, a feasibility analysis for a full 3D one-transistor-one-capacitor (1T1C) DRAM cell is performed with promising results.

Contents

List of Symbols

A	Area
$A_{\prime}^{*}\, \delta_{\prime}\, \eta$	Empirical parameters used to compute the surface roughness scattering mobility degradation term within the Lombardi mobility model
A_{ij}^{K}	Entry in the left-hand side matrix $A_{\prime}$ for a triangulation cell $K_{\prime}$ within the finite elements formalism
A_0	Richardson constant
A_c	Effective Richardson constant
A_{exg}	Total exciton generation rate
A_{ij}	Entry in the left-hand side matrix A within the finite elements formalism
Ag	Silver
Al_2O_3	Aluminum oxide
Ar^+	Argon cation
Au	Gold
$B(x)$	Bernoulli function
$B_{\prime}\, C_{\prime}\, N_{A0\prime}\, N_{D0\prime}\, N_{0\prime}\, N_{2\prime}\, \lambda_{\prime}\, k$	Empirical parameters used to compute the acoustic phonon mobility degradation term within the Lombardi mobility model
$BaTaO_2N$	Barium-tantalum oxynitride
$Ba_xSr_{1-x}TiO_3$	Barium-strontium titanate
$BiTaO$	Bismuth tantalate
C	Capacitance
$C_{r\prime}\, C_{S\prime}\, P_{C\prime}\, N_{A0\prime}\, N_{D0}$	Empirical parameters used in the calculation of the doping dependent mobility according to the Masetti mobility model
$CeAlO_3$	Cerium aluminum oxide
Cu	Copper
D	Diffusion coefficient
D_n	Electron diffusion coefficient
D_p	Hole diffusion coefficient
D_{ij}	Parameter used to compute the three dimensional coefficient κ_{ij}
E	Energy
E_i^-	Specific energy of an electron in a state i within the Multistate configuration framework
E_C	Conduction band edge

E_D	Energetic depth of the trap state inside the insulator within the kinetic Monte Carlo framework
E_V	Valence band edge
E_e	Energy of an electron in an electrode
E_g	Bandgap energy of a semiconductor
E_i	Base energy of a specific state within the Multistate configuration framework *equivalentto*
E_i	Intrinsic Fermi energy of a semiconductor
E_B	Energy barrier seen by a charge carrier
$E_{F,n}$	Electron quasi-Fermi energy
$E_{F,p}$	Hole quasi-Fermi energy
$E_{f,l/r}$	Fermi function of the left (right) injecting contact
E_{trap}	Trap level energy level
F	Force
$F(x)$	Probability distribution function within the kinetic Monte Carlo framework
F^+	Charged oxygen vacancy
F^0	Neutral oxygen vacancy
$F^{-1}(m)$	Inverse of the probability distribution function for random number m
F_i^K	Entry in the right hand side vector of a function, for a triangulation cell K, numerically approximated using the finite elements method
F_i	Entry in the right hand side vector of a function, numerically approximated using the finite elements method
$F_{1/2}$	Fermi integral of order 1/2
$F_\perp$	Transverse electric field at the insulator-semiconductor interface within the Lombardi mobility model
F_{hfs}	Critical electrical field at which the high field saturation is activated within the extended Canali mobility model
F_{ref}	Reference electric field within the Lombardi mobility model
$G_{C,\nu}(u,l,\epsilon)$	Generation rate at position u due to an electron tunneling process from position l with energy ϵ
G_n	Electron generation rate in semiconductors
G_p	Hole generation rate in semiconductors
$GdAlO_3$	Gadolinium aluminate
H_i	Inner energy of state i within the Multistate configuration framework
I_p	Modified Bessel function of order p
J	Arbitrary flux within the finite volume formalism
J_n	Electron current density
J_p	Hole current density

K	Total number of charges (positive or negative) associated to a state within the Multistate configuration framework
K	Wave number of a electron inside a defect state
K_r	Total number of charges associated to a reservoir within the Multistate configuration framework
L	Average exciton diffusion length
Mo	Molybdenum
MoO_3	Molybdenum trioxide
N_D^+	Density of ionized donor atoms
N_A^-	Density of ionized acceptor atoms
N_C	Conduction band effective density of states
N_E	Density of states in a metal electrode
N_V	Valence band effective density of states
N_n	Number of electrons that interact in a transition within the Multistate configuration framework
N_{occ}	Number of grid points already occupied by a photo-generated exciton
N_p	Number of holes that interact in a transition within the Multistate configuration framework
N_{ref}	Reference doping concentration for the doping dependent carrier lifetimes in the Shockley-Read-Hall recombination model
O	Oxigen
$P(\Delta\epsilon)$	Probability of accepting a configuration with $\Delta\epsilon$ energy difference between initial and final state
P	Elastic tunneling probability of a charge carrier into a defect state
$P(X_1, \ldots, X_N; t)$	Probability of finding X_1 particles of the species $S_1, \ldots, X_N$ particles of the species S_N in our volume V of interest at a given time t
$P(\tau, \mu)d\tau$	Probability at time t that the next Rm reaction will occur within the differential time interval $(t+\tau, t+\tau+d\tau)$
$P(n, t)$	Probability of finding the system under observation in state n at time t
$P(x)$	Probability density function within the kinetic Monte Carlo framework
$P(y)dy$	Probability that the random number x will be found between y and $y+dy$
P_p	Multiphonon transition probability
$P_0(\tau)$	Probability that no reaction will occur between the times $(t, t+\tau)$
$P_1(\tau)$	Probability that an arbitrary transition will occur in the time interval $(t+\tau, t+\tau+d\tau)$

$P_2(\mu\|\tau)$	Probability that the next transition will be precisely R_μ
Pt	Platinum
R	Arbitrary generation term within the finite volume formalism
R_{net}^{SRH}	Shockley-Read-Hall net recombination rate
R_0	Coefficient for the inelastic phonon-assisted trap-to-trap transition rate within the kinetic Monte Carlo framework
R_μ	Transition rate from one state to another state within the kinetic Monte Carlo framework
$R_{C,\nu}(u, l, \epsilon)$	Recombination rate at position u due to an electron tunneling process from position l with energy ϵ
R_n	Electron recombination rate in semiconductors
R_p	Hole recombination rate in semiconductors
Ru	Ruthenium
RuO_x	Ruthenium oxide
S	Huang-Rhys factor
S_N	Species N of particles
Si	Silicon
SiO_2	Silicon oxide
Si_3N_4	Silicon nitride
Sr	Strontium
$SrRuO_3$	Strontium ruthenate
$SrTa_2O_6$	Strontium tantalate
$SrTiO_3$	Strontium titanate
T	Temperature
$T(E_x)$	Energy dependent transmission coefficient for a direct tunneling process to point x
T_{DD}^{el}	Elastic trap assisted tunneling rate within the kinetic Monte Carlo framework
T_{ED}^{el}	Elastic tunneling probabiltiy of an electron from the electrode into a defect state
T_{DD}^{inel}	Inelastic trap assisted tunneling rate within the kinetic Monte Carlo framework
T_{ED}^{inel}	Inelastic tunneling probabiltiy of an electron from the electrode into a defect state
T_r	All allowed charge carrier transitions associated to a reservoir within the Multistate configuration framework
$T_{CC,\nu}(l, \epsilon)$	Interface transmission coefficient for a particle at point l of the ν-th shifted conduction band with energy ϵ

$T_{CC,\nu}(u,\epsilon)$	Interface transmission coefficient for a particle at point u of the $\nu-$th shifted conduction band with energy ϵ
$T_{CC,\nu}(x,\epsilon)$	Interface transmission coefficient for a particle at point x of the $\nu-$th shifted conduction band with energy ϵ
T_{PF}	Transition rate for a thermally activated electron, trapped in a defect state, to reach the conduction band of the dielectric within the kinetic Monte Carlo framework
T_{ex}	Average exciton diffusion time
T_{ij}	All allowed transition t between state i and j within the Multistate configuration framework
T_n	Transmission coefficient
Ta	Tantalum
TaN	Tantalum nitride
Ta_2O_5	Tantalum pentoxide
Ti	Titanium
TiN	Titanium nitride
TiO_2	Titanium oxide
U_i	The electrostatic potential in grid node i
U_{nm}	Potential energy difference between final and initial state
V	Electrostatic potential
V_D	Drain voltage
V_G	Gate voltage
V_S	Source voltage
V_T	Trap interaction volume
V_{oc}	Open circuit voltage of an organic solar cell
W	Wolfram
$W(n \rightarrow m)$	Probability that a transition from state n to state m will take place in the unit time interval
$X(t)$	Updated number of particles for the randomly picked (τ,μ) pair
$X_i^{(k)}(t)$	k^{th} Moment of the probability density function
X_N	Number N of particles
Z	Number of equidistant time subintervals τ/δ
ZnO	Zinc oxide
Δ	Laplace operator
ΔE	Dissipated energy for a number n of emitted phonons
ΔE_{PF}	Frenkel barrier lowering term within the kinetic Monte Carlo framework
ΔE_{SE}	Schottky barrier lowering term within the kinetic Monte Carlo framework
$\Delta_i(t)$	Variance of the probability density function

$\Gamma_{C,\nu}(u, l, \epsilon)$	Direct tunneling probability to point u of the ν-th shifted conduction band for a particle from the initial point l with energy ϵ
Γ_C	Electron reflection coefficient to the conduction band
Λ	Quantum correction potential term for the confined charge carrier densities within the density gradient model
Λ_B	De Broglie wavelength
Λ_n	Quantum correction potential term for the electron density within the density gradient model
Λ_p	Quantum correction potential term for the hole density within the density gradient model
Ω_i	Simulation domain according to the finite volume discretization scheme
Φ_{SRO}	Workfunction of the SRO electrode
$\Phi_j\psi_j(\mathbf{x})$	Product of the expansion coefficients and the finite element shape function
$\Psi(z_0)$	Electron wave function at position z_0
Ψ_0	Electron wave function at position 0
Θ	Heaviside function
α	Dimensionless tunneling parameter
$\alpha, \beta, \beta_0, \beta_{exp}$	Empirical parameters used in the calculation of the field dependency for the electron and hole mobilities within the extended Canali mobility model
$\alpha, \beta, \mu_{const}, \mu_1$	Empirical parameters used in the calculation of the doping dependent mobility according to the Masetti mobility model
$\alpha, \beta, \vartheta, \eta, \xi$	Empirical parameters used for the computation of the quantum correction potential term within the density gradient model
$\bar{E}_C$	Average conduction band energy
$\bar{E}_V$	Average valence band energy
$\bar{\mathbf{x}}$	Normalized value of x, $\mathbf{x}/z^*$
$\bar{z}^j$	Normalized value of z in step j, z^j/z^*
β	Thermodynamic beta , $1/k_BT$, within the Multistate configuration framework
δE_{ij}	Energy difference between to neighboring grid nodes
δt	Transition time interval within the kinetic Monte Carlo framework
ϵ	Relative dielectric permittivity
$\epsilon(E)$	Field dependent permittivity within the kinetic Monte Carlo framework
ϵ_A	Absolute error in the Bank and Rose scheme

ϵ_R	Relative error in the Bank and Rose scheme , default $\epsilon_R \equiv 10^{-5}$
ϵ_0	Vacuum permittivity
ϵ_{opt}	Optical dielectric permitivitty constant
η	Efficiency of the organic solar cell
η_{ehr}	Electron/hole recombination efficiency
η_{exs}	Exciton dissociation efficiency
γ	Exponent of the power-law for the doping dependent term in the Shockley-Read-Hall recombination model
γ_n	Auxiliary function used to express electron density when Fermi statistics are assumed
γ_p	Auxiliary function used to express hole density when Fermi statistics are assumed
$\hbar$	Planck′s constant over 2π
$\kappa_{C,\nu}(r,\epsilon)$	Local wave number of a particle at position r and energy ϵ
κ_{ij}	Coefficient of the control volume according to the finite volume discretization scheme
λ	Numerical parameter used in the solution of the system of coupled partial differential equations g, has a default value as close as possible to 1
$\|\nabla\Phi_n\|$	Gradient of the quasi-Fermi potential
$\mathring{A}$	Angstrom
μ	Discrete set of possible transitions or reactions $\mu \in (1,\ldots,M)$ between system states within the kinetic Monte Carlo framework
$\mu(F)$	Field dependent mobility according to the extended Canali mobility model
$\mu(\Omega_i)$	Control volume according to the finite volume discretization scheme
μ_{ac}	Acoustic phonon mobility degradation term within the Lombardi mobility model
μ_{dop}	Doping dependent charge carrier mobility according to the Masetti mobility model
μ_{low}	Low field mobility according to the extended Canali mobility model
$\mu_{min1/2}$	Reference mobilities in the Masetti mobility model
μ_n	Electron mobility in semiconductors
μ_p	Hole mobility in semiconductors
μ_{sr}	Surface roughness scattering mobility degradation term within the Lombardi mobility model
∇	Nabla operator
ν **or** a_0	Attempt-to-escape phonon frequency
ω	Optical phonon frequency

$\partial\Omega_i$	Boundary of the simulation domain according to the finite volume discretization scheme
$\phi_h(\mathbf{x})$	Approximate function for the electrostatic potential
π	Pi constant
ψ	Test function within the finite elements formalism
ρ_T	Charge density contributed by traps and fixed charges
σ	Trap state cross-section
$\sum_\mu h_\nu c_\mu \delta t$	Sum of first order probabilities for all R_μ reactions
τ	Time evolution variable within the kinetic Monte Carlo framework
τ_c	Doping-, field- and temperature-dependent carrier lifetime in the Shockley-Read-Hall recombination model
τ_n	Electron lifetime in the Shockley-Read-Hall recombination model
τ_p	Hole lifetime in the Shockley-Read-Hall recombination model
τ_{dop}	Doping-dependent term of the carrier lifetime in the Shockley-Read-Hall recombination model
τ_{hop}	Average exciton hopping time
$\tau_{lifetime}$	Average exciton lifetime
τ_{max}	Maximal carrier lifetime in the Shockley-Read-Hall recombination model
τ_{min}	Minimal carrier lifetime in the Shockley-Read-Hall recombination model
$\tau_{separation}$	Average exciton separation time
$\mathbf{A}$	Matrix form of the left-hand side of a function -product of the expansion coefficients and the finite element shape function- calculated using the finite elements method
$\mathbf{F}$	Vector form of the right hand side of a function, numerically approximated using the finite elements method
$\mathbf{Z}$	Canonical partition function , sum of all the Z_i within the Multistate configuration framework
$\mathbf{x}_q^K$	The q^{th} quadrature point on cell K within the finite elements method
a	Acceleration
a_0	Lattice constant
a_{col}	Electron/hole collection rate at a contact
a_{exd}	Exciton decay rate
a_{exg}	Exciton generation rate at a grid node
a_{exh}	Exciton hopping rate

a_{exs}	Exciton dissociation rate
a_{hop}	Electron/hole hopping rate
a_{inj}	Electron/hole injection rate at a contact
a_{rec}	Electron/hole recombination rate
c	Capture rate within the Multistate configuration framework
c_{ij}^{+}	Rate constant for the inelastic phonon-assisted trap-to-trap transition under phonon absorption within the kinetic Monte Carlo framework
c_{ij}^{-}	Rate constant for the inelastic phonon-assisted trap-to-trap transition under phonon emission within the kinetic Monte Carlo framework
$c_{C\prime inelastic}^{n}$	Phonon-assisted capture rate from an electron tunneling from an electrode into a trap
c_0	Auxiliary function used to calculate the inelastic electrode-defect state tunneling probabiltiy
c_μ	Transition rate parameter within the kinetic Monte Carlo framework
c_{ij}	Capture rate between initial state i and final state j within the Multistate configuration framework
dQ	Differential charge of a capacitor
dU	Differential voltage of a capacitor
d_{ij}	Parameter used to compute the two dimensional coefficient κ_{ij}
e	Emission rate within the Multistate configuration framework
eV	Electron volt
e_{ij}	Emission rate between initial state i and final state j within the Multistate configuration framework
$f(E_e)$	Fermi-Dirac energy distribution of an electron inside an electrode
$f(T)$	Temperature dependent function used in the evaluation of the carrier lifetime in the Shockley-Read-Hall recombination model
$f_{B\prime}\, f_{BE}$	Bose-Einstein distribution
g	System of coupled partial differential equations , consisting of $g_1(u, v, w)$-$g_2(u, v, w)$ according to the Bank and Rose scheme
$g(z_0)$	Root of the system of coupled partial differential equations , consisting of $g_1(u, v, w)$-$g_2(u, v, w)$ according to the Bank and Rose scheme
$g(z)$	First derivative of g the system of coupled partial differential equations according to the Bank and Rose scheme

$g_1(u, v, w)$	Normalized Poisson equation according to the Bank and Rose scheme , where u is the electrostatic potential and v and w are the electron and hole quasi Fermi levels
$g_2(u, v, w)$	Normalized electron continuity equation according to the Bank and Rose scheme , where u is the electrostatic potential and v and w are the electron and hole quasi Fermi levels
$g_3(u, v, w)$	Normalized hole continuity equation according to the Bank and Rose scheme , where u is the electrostatic potential and v and w are the electron and hole quasi Fermi levels
g_c	Degeneracy factor
$g_c(F)$	Field enhancement factor used in the calculation of the field-dependent carrier lifetime in the Shockley-Read-Hall recombination model
g_i	Degeneracy factor of a state i within the Multi-state configuration framework
g_m	Transconductance
h	Planck′s constant
h_μ	Number of particles found in volume V, at the time t, which can undergo a R_μ transition
$h_\mu c_\mu \delta t$	First order probability that an R_μ reaction will take place in volume V in the time interval t
$h_t c_t$	Updated $h_\mu c_\mu$ for the randomly picked (τ, μ) pair
$j_{CC}(l)$	Tunneling current density
j_{DT}	Direct tunneling current density
j_{FN}	Fowler-Nordheim tunneling current density
j_{ij}	Variable used to discretize the Poisson and electron/hole continuity equation according to the finite volume discretization scheme
j_{sat}	Material dependent saturation current density
j_{sc}	Short circuit current density of an organic solar cell
j_{se}	Schottky emission current density
k	Wavenumber
k_0	Wave number of an electron in an electrode
k_B	Boltzmann′s constant
l	Number of emitted phonons
l	geometrical extent in x/y/z direction
l_{ij}	Parameter used to compute the one dimensional coefficient κ_{ij}
m	Mass
m_n	Electron effective mass
m_p	Hole effective mass
m_0	Electron mass

m_C	Conduction band tunneling mass
m_e	Electron mass in a metal electrode
m_i	Electron mass in a an insulator
m_t	Phonon-assisted electron tunneling mass
n	Electron density in semiconductors
n_1	Trapped electron density in the Shockley-Read-Hall recombination model
n_i	Intrinsic carrier density
$o(\delta)$	bla bla
p	Hole density in semiconductors
p	Momentum
p_1	Trapped hole density in the Shockley-Read-Hall recombination model
p_μ	Product of h_μ and c_μ
q_i	The electric charge in grid node i
r_D	Electron localization radius
r_{ij}	Variable used to discretize the Poisson and electron/hole continuity equation according to the finite volume discretization scheme
r_{ij}	Distance between to neighboring grid nodes
s_i^*	Equilibrium occupation probability of state i within the Multistate configuration framework
s_i	Occupation probability of a specific state i state i and j within the Multistate configuration framework
t	Thickness
v	Velocity
$v(0)$	Electron velocity at position 0
$v(z_0)$	Electron velocity at position z_0
v_+	Velocity of the an electron in confined zone
v_-	Velocity of the an electron in the unconfined side of the barrier
v_ν	Electron velocity in the confined and free region
$v_{sat,0}$	Temperature independent term of the saturation drift velocity of charge carriers within the extended Canali mobility model
$v_{sat,exp}$	Temperature dependent exponent of the saturation drift velocity of charge carriers within the extended Canali mobility model
v_{sat}	Saturation drift velocity of charge carriers within the extended Canali mobility model
v_{th}	Charge carrier thermal velocity
w_q^K	The q^{th} quadrature weight on cell K within the finite elements method
x	Variation of z from step z^j to z^{j+1}

z	Auxiliary function, product of the Huang Rhys factor and the square root of the Bose-Einstein distribution within the kinetic Monte Carlo framework
z^j	Initial guess of the z_0, the root of the system $g(z_0) \equiv 0$
z^*	Normalization factor for $z(u, v, w)$
z^{j+1}	Numerical approximation of z_0, the root of the system $g(z_0) \equiv 0$, in the $j+1$ step
z_{ref}	Reference value for $z(u, v, w)$ to ensure stability

List of Abbreviations

1T1C	One Transistor One Cell
AC	Alternative Current
ALD	Atomic Layer Deposition
AVD	Atomic Vapor Deposition
BEOL	Back End of Line
BHJ	Bulk Heterojunction
CB	Conduction Band
CBO	Conduction Band Offset
CMOS	Complementary Metal Oxide Semiconductor
CVD	Chemical Vapor Deposition
D/A	Donor/Acceptor Interface
DC	Direct Current
DD	Drift Diffusion
DoF	Degree of Freedom
DRAM	Dynamic Random Access Memory
EOT	Effective Oxide Thickness
EQE	External Quantum Efficiency
FE	Finite Element
FEOL	Front End of Line
FOM	Figure of Merit
FRM	First Reaction Method
FV	Finite Volumes
GAO	$GdAlO_3$
GUI	Graphical User Interface
HF-DFT	Hartree-Fock Density Functional Theory
HKMG	High-k Metal Gate
HOMO	Highest Occupied Molecular Orbital
IC	Integrated Circuit
ILD	Interlevel Dielectric
IQE	Internal Quantum Efficiency
ITO	Indium Tin Oxide
ITRS	International Technology Roadmap for Semiconductors
IV	Current Voltage Characteristic
IVT	Current Voltage Temperature Characteristic
kMC	Kinetic Monte Carlo
LCAO	Linear Combination of Atomic Orbitals
LDD	Low Drain Doping

LOCOS	Local Silicon Oxidation
LUMO	Lowest Unoccupied Molecular Orbital
MBE	Molecular Beam Epitaxy
MD	Molecular Dynamics
MIM	Metal Insulator Metal
MIS	Metal Insulator Semiconductor
MMC	Metropolis Monte Carlo
MOCVD	Metal Organic Chemical Vapor Deposition
MSC	Multistate Configuration
MUX	Multiplexer
NMOS	N Channel MOS Transistor
OSC	Organic Semiconductor
P3HT:PCBM	Poly(3-HexylThiophene):Phenyl-C61-Butyric acid Methyl ester
PC61BM	[6,6]-Phenyl-C61-Butyric acid Methyl ester
PC71BM	[6,6]-Phenyl-C71-Butyric acid Methyl ester
PCBA	[6,6]-Phenyl-C61-Butyric Acid
PDE	Partial Differential Equations
PDTSTPD	Poly[(5,6-dihydro-5-octyl-4,6-dioxo-4H-thieno[3,4-c]pyrrole-1,3-diyl)[4,4-bis(2-ethylhexyl)-4H-silolo[3,2-b:4,5-b;]dithiophene-2,6-diyl]]
PEDOT:PSS	Poly(3,4-EthyleneDioxyThiophene) PolyStyrene Sulfonate
PF	Poole Frenkel
PTB7	Poly(4,8-bis[(2-ethylhexyl)oxy]benzo[1,2-b:4,5-b]dithiophene-2,6-diyl3-fluoro-2-[(2-ethylhexyl)carbonyl]thieno[3,4-b]thiophenediyl)
PVD	Physical Vapor Deposition
RAS	Row Address Strobe
RF	Radio Frequency
SEM	Surface Electron Microscopy
SENSE	Sentaurus Structure Editor
SRH	Shockley-Read Hall
SRO	$SrRuO_3$
STI	Shallow Trench Isolation
STO	$SrTiO_3$
TAT	Trap Assisted Tunneling
TCAD	Technology Computer Aided Design
TEM	Transmission Electron Microscopy
WKB	Wenzel Kramers Brillouin
ZAZ	$ZrO_2Al_2O_3ZrO_2$

1 Introduction

Motivation

Over the last decades, the downscaling of integrated circuit devices following Moor's law [1] has led to ever higher packing densities and thus smaller and faster electronic components. Driven by cost reduction and performance optimization, the semiconductor industry has made some amazing progress, with the most noticeable advances for the complementary metal oxide semiconductor (CMOS) transistors and logic circuits.

It has to be noted however that this success of integrating ever more CMOS devices on shrinking wafer sizes has to be firstly attributed to the unique properties of silicon and its native oxide SiO_2. With the discovery, development and improvement of the Czocharalski process, virtually defect free crystalline silicon ingots can be fabricated and then sliced to wafers [2]. The thickness of the thermally grown SiO_2 can be controlled with high precision and the result is a high quality dielectric layer [3], with a very smooth interface to the silicon region, where most of the charge carriers will flow.

Besides CMOS transistors also passive devices – like metal-insulator-metal (MIM) capacitors for RF and analog/digital circuits – have been in the spotlight of research engineers, in order to improve their price/performance aspect [4–7].

The dynamic random access memory (DRAM), which can be found in every personal computer today, has not made an exception from the miniaturization trend mentioned above. This type of memory has some undisputed advantages over other architectures: simple layout – only one transistor and one capacitor –, high speed and reliable operation.

Nevertheless, this simple integrated circuit (IC) seems to be facing some technological challenges over the last few years. The storage capacitor of the DRAM cell, traditionally consuming most of the cell wafer area needed some profound design and geometry changes [8] in order to keep the cell performance and reliability assured, while the thickness of the dielectric layer has been gradually reduced.

An approach that proved successful for the last DRAM generations is the vertical integration of these storage capacitors on the wafer, using deep trench architectures [9,10]. Nevertheless, this innovation was not sufficient to keep the pace with the ever shrinking device sizes; new problems arose with the increasing tunneling currents through the thin dielectric layer – until a few years ago silicon dioxide – of the cell capacitor. The need for new material systems eventually became obvious.

In Figure 1.1 the strict DRAM requirements for the next years are presented, taken from the International Technology Roadmap for Semiconductors (ITRS) 2013 Edition. As one can see, some cells are colored red starting with 2016, which means that no manufacturable solution is yet known. One requirement that has been troubling research engineers over the last years is the need to ever decrease the equivalent effective oxide thickness or EOT. This parameter enables us to estimate the thickness of a dielectric layer when compared with SiO_2, in order to keep the same capacitance density. Since the permittivity of SiO_2 is $k = 3.9$ [11], one can write for a MIM structure of thickness t and with a permittivity k_{high-k}:

$$EOT = t_{high-k}\frac{k_{SiO_2}}{k_{high-k}} \tag{1.0.1}$$

Introducing higher-k dielectrics allowed the manufacturers to keep thick insulating layers while maintaining the charge retention capabilities of their devices. Although the integration of these new materials caused some unexpected problems in the fabrication process, like the formation of defect-rich interfacial layers or Fermi-level pinning near the electrodes [13–15] some first successes could be recorded; the optimization of the fabrication techniques in orders to obtain high quality dielectric films is still an important research topic for many companies in the semiconductor business [16,17]. Two currently used materials for DRAM

Year of Production	*2013*	*2014*	*2015*	*2016*	*2017*	*2018*	*2019*	*2020*
Logic Industry "Node Range" Labeling (nm) [based on 0.71x reduction per "Node Range" ("Node" = ~2x Mx)	"16/14"		"11/10"		"8/7"		"6/5"	
MPU/ASIC Metal 1 (M1) ½ Pitch (nm) (contacted)	40	32	32	28.3	25.3	22.5	20.0	17.9
Half Pitch (Contacted line) (nm)	28	26	24	22	20	18	17	15
DRAM cell size (μm^2) [2]	0.00470	0.00406	0.00346	0.00194	0.00160	0.00130	0.00116	0.00090
DRAM storage node cell capacitor dielectric: equivalent oxide thickness EOT (nm) [3]	0.55	0.5	0.4	0.3	0.3	0.3	0.3	0.3
DRAM storage node cell capacitor voltage (V) [4]	0.53	0.53	0.5	0.5	0.5	0.48	0.45	0.45
Equivalent Electric field of capacitor dielectric, (MV/cm) [5]	9.64	10.60	12.50	16.67	16.67	16.00	15.00	15.00
DRAM cell FET structure [6]	RCAT+Fin	RCAT+Fin	RCAT+Fin	VCT	VCT	VCT	VCT	VCT
DRAM Cell Transistor Gate material (Burried/Planer/Vertical+Gate material)	Buried/TiN	Buried/TiN	Buried/TiN	Vertical/TiN	Vertical/TiN	Vertical/TiN	Vertical/TiN	Vertical/TiN
DRAM cell FET dielectric: equivalent oxide thickness, EOT (nm) [7]	5	4.5	4.5	4.5	4	4	4	4
Maximum Word line (WL) level (V) [8]	2.7	2.6	2.6	2.6	2.6	2.4	2.4	2.4
Negative Word line (WL) use [9]	yes	yes	yes	yes	yes	yes	yes	yes
Equivalent Electric field of cell FET device dielectric (MV/cm) [10]	5.40	5.78	5.78	5.78	6.50	6.00	6.00	6.00
Cell Size Factor: a [11]	6	6	6	4	4	4	4	4
Array Area Efficiency [12]	0.55	0.55	0.55	0.55	0.55	0.55	0.55	0.55
Minimum DRAM retention time (ms) [13]	64	64	64	64	64	64	64	64
DRAM soft error rate (fits) [14]	1000	1000	1000	1000	1000	1000	1000	1000
V_{int} (support FET voltage) [V] [15]	1.2	1.2	1.1	1.1	1.1	1.1	1.1	1.1
Support nMOS EOT [nm] [16]	2.2	2.2	2	1.8	1.8	1.8	1.6	1.6
Support PMOS Gate Electrode [17]	P+Poly/W	P+Poly/W	P+Poly/W	TiN	TiN	TiN	TiN	TiN
Support Gate Oxide [18]	SiON	SiON	SiON	HfSiON	HfSiON	HfSiON	HfSiON	HfSiON
Support min. L_{gate} for NMOS FET, physical [nm] [19]	55	48	42	38	38	38	38	35
Support I_{sat-n} [µA/µm] (25C, $V_g=V_d=V_{int}$) [20]	400	400	400	450	450	450	450	450
Support min. V_{tn} (25C, $G_{m,max}$, V_d=55mV) [21]	0.40	0.40	0.40	0.40	0.40	0.40	0.40	0.40
Support I_{sat-p} [µA/µm] (25C, $Vg=V_d=-V_{int}$) [22]	175	175	175	200	200	200	200	200
Support min. V_{tp} (25C, $G_{m,max}$, V_d=55mV) [23]	-0.40	-0.40	-0.40	-0.40	-0.40	-0.40	-0.40	-0.40
Gb/1chip target	4G	8G	8G	8G	8G	16G	16G	16G

Manufacturable solutions exist, and are being optimized

Manufacturable solutions are known

Interim solutions are known

Manufacturable solutions are NOT known

Figure 1.1: 2013 ITRS prediction for the DRAM market. Table taken from [12]

cells are HfO_2 and ZrO_2, with k values of 15 and 40 respectively [18–20]. These permittivity values are 4 to 10 times larger than that of SiO_2 and suffice to scale down e.g. the physical dimensions for the gate of a CMOS transistor, while maintaining a high capacitance. In fact Intel has introduced the HfO_2 as early as 2007 in productions for its new 45 nm high-k metal gate transistor generation [21].

Yet the ITRS predicts an equivalent oxide thickness (EOT) below 0.4 nm for the sub 20 nm minimum feature size DRAM memories [12], a value that cannot be reached with the above mentioned dielectrics, since they can only be scaled down to approx. 0.6 EOT.

The search for a next generation DRAM cell dielectric therefore still goes on. Among other candidates, showing promising results is the perovskite-based dielectric $SrTiO_3$ [22], with k values of more than 100 [23, 24] and remarkable EOT as low as 0.2. Several experimental studies have been performed for the STO high-k dielectric, proposing different materials as electrodes for the metal insulator metal (MIM) capacitors [25–27]. One conductive oxide can be highlighted as an appealing choice for the capacitor electrodes, namely $SrRuO_3$, since it is lattice matched to STO and a high conductivity has been reported [23, 28].

Although the SRO/STO/SRO structure could have the potential to become the next higher-k material system to be implemented in the DRAM capacitors at industry scale, some issues have to be addressed and improved first. While the dielectric constant and EOT reported in literature are well suited to fulfill the predictions of the ITRS, the main problem for STO films remains the large leakage current.

It is thus necessary to have a deep understanding of the leakage mechanisms in this new and promising material system, in order to reduce it for large scale applications. This is in fact the main aim of the present work, to develop a better understanding of the physics for novel high-k dielectric materials.

As in many other fields of the semiconductor industry, whenever the reasons of an unpredicted behavior are unclear or there is a need for further performance optimization, a simulation study can provide useful insights. Additionally, simulation studies can be useful for extracting physical parameters that are otherwise hard or even impossible to measure. When opting for a simulation

study, several frameworks are available to researchers and could be arbitrarily summarized as follows:

1. Quantum mechanical methods – like Non Equilibrium Green's Function [29–31]
2. Semi classical methods – like Monte Carlo [32–34]
3. Modified drift diffusion/hydrodynamic methods – usually commercial simulators [35–37]

In this current study we choose the latter two methods in order to identify the main reasons for increased leakage in thin STO MIM capacitors, since a quantum mechanical approach would be extremely time and resource consuming, with limited options of applying the findings on realistic devices like DRAM cells. Simulations are first carried out using the in-house kinetic Monte Carlo [38–40] framework; this methodology enables us to identify the dominant transport mechanisms from a large number of possible candidates. It also allows us to find meaningful and adequate estimations for parameters that are either hard to measure or for which measurements give a too broad interval.

Overview

This work is organized in six Chapters. Besides the short motivation already presented in Chapter 1, the next chapters provide both an insight in the field of high-*k* dielectrics, the historical developments, state-of-the-art modeling techniques, etc. Also, the problems that state of the art devices - which use these novel materials - encounter, are presented and a physical explanation thereof is offered.

Chapter 2 is intended to offer some background information for readers not familiar with the topic of high-*k* dielectrics. It begins with a historical perspective, naming some milestones in the development and fabrication of such materials, starting with the early 50s. Also the most common fabrication techniques are shortly presented, with an emphasis on the method used to obtained the high-*k* samples that will be further analyzed in this thesis. Also, the basic operating principle of a DRAM memory cell is presented, since this is the main application for these special materials with high permittivity. Finally, an overview of the

state-of-the-art simulation methods, used to analyze and get a better understanding of the transport mechanisms through thin high-k dielectric films, is presented.

In the next Chapter, a stochastic simulation framework is used in order to get an insight of the dominant leakage mechanisms that are responsible for the undesired large currents in our fabricated capacitors, namely the SRO/STO/STO thin film capacitors. We opted for a kinetic Monte Carlo (kMC) approach, as opposed to currently used analytical or drift-diffusion based simulators, since it offers some unique features. No assumption on the nature of the measured leakage currents has to be made in advance, all possible physical transport mechanisms can be included in the framework and after a sufficient number of simulation runs the dominant channels can easily be identified. We also use the kMC approach in order to extract some physical parameters of the STO dielectric that are otherwise difficult to determine e.g. via measurements.

Chapter 4 focuses on a realistic implementation of a DRAM cell using a modified commercial TCAD framework. We use the findings of Chapter 3 regarding the dominant transport mechanisms, as well as some material parameters, as input for our drift-diffusion (DD) simulator. We can thus minimize the use of fitting parameters and offer a solid physical justification to the parameters and physical mechanisms included in the simulation. The modified DD simulator is also able to include complex transport mechanisms, as trap-assisted-tunneling, while offering some advantages over the kMC approach, namely: increased simulation speed, the possibility to model arbitrary 3D geometries and visualization and post-processing options. The performance of a deep trench DRAM memory cell that uses STO as dielectric is analyzed.

Chapter 5 presents the conclusions of this work, giving also a brief comparison of the advantages and disadvantages of the kMC and DD approach for simulating and analyzing leakage properties of DRAM capacitors. Finally, in the last Chapter, an outlook is presented, with some ideas on how the simulation procedure presented in this work could be improved and how the two approaches could even be self-consistently coupled, after some needed modifications will be performed.

2 Development of High-k Dielectrics

2.1 Historical Perspective

The field of high-k oxides may seem exotic and most of us would be tempted to believe that it has only recently emerged, as an alternative to the limitations of the Si/SiO_2 system but this is not true at all.

A first article [41] that reports on the growth of a TiO_2 thin film on a silicon substrate, using a technique called then "molecular layering", has been published in the USSR as early as 1969. Its authors – G.S. Sveshikova, S.I. Kol'tsov and V.B. Aleskovskii, all from the Leningrad Lensoviet Institute of Technology – can be considered among the pioneers of the technique now called atomic layer deposition (ALD). V.B. Aleskovskii proposed the idea of molecular layering in his PhD thesis "Matrix hypothesis and ways of synthesis of some active solid compounds" [42] already in 1952, with the first samples grown by this method reported by S.I. Kol'tsov in the early 60s.

Another remarkable achievement and milestone for the history of ALD and the early progress in the field of high-k is reported by the same group in their 1974 paper "Chemistry and technology of solids" [43]. It demonstrates, for the first time, what we nowadays call nanolaminates using SiO_2 and TiO_2 and outlines some concepts for the application of this technology to nanodevices.

For the western world the first successful ALD demonstration is largely attributed to Dr. Tuomo Suntola in 1974. A patent for this technology is issued in 1977 (US patent 4058430) and since then various other groups report on the growth of oxides, semiconductors and conductive oxides using this technique.

Although interesting for the research community, the fabrication of high-k materials and their possible applications were not appealing to the industry at first.

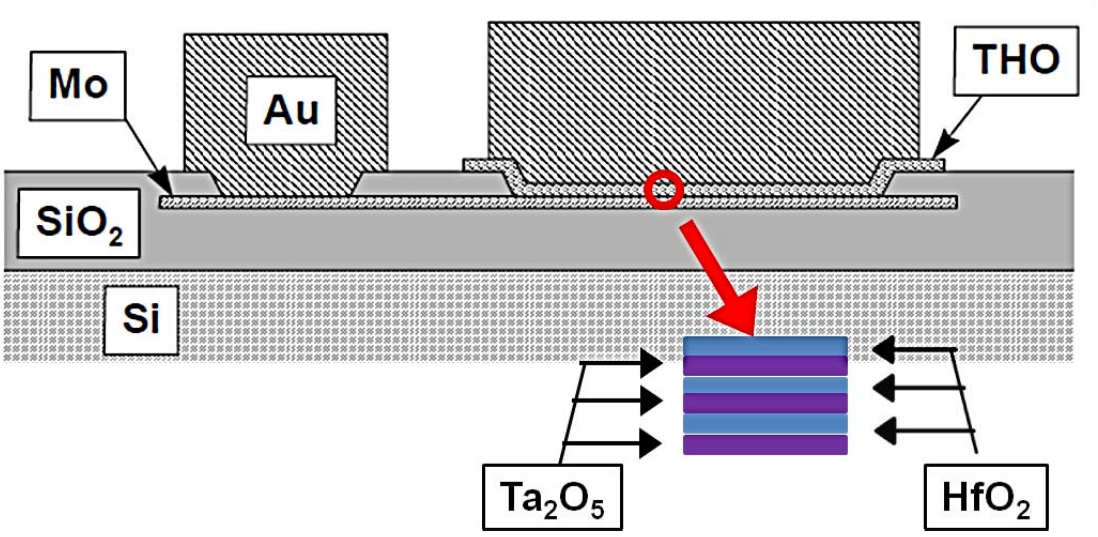

Figure 2.1: Cross-section of the first high-k nanolaminate MIM capacitor, using alternating Ta_2O_5 and HfO_2 dielectric layers (taken from [44]).

A first industrial patent was issued in Sweden only in 1992. The invention refers to a high-k Metal Insulator Metal (MIM) capacitor structure and the fabrication thereof. A nanolamitate structure is used as insulator between the two electrodes. Successive layers of Ta_2O_5 and HfO_2 are deposited one on top of each other, having a thickness of few nanometers. Ta_2O_5 is chosen for its very high permittivity while HfO_2 has very low leakage properties. This first industrial high-k application has a quality factor better than 500 and an average permittivity better than 15, some impressive figures of merit for the early 90s [44]. The cross-section of this MIM capacitor structure is shown below, in Figure 2.1.

But the semiconductor industry was still skeptical at first. No major chip manufacturer was ready to give up the benefits of the perfectly lattice matched, low defects interface between Si and SiO_2. Therefore some tricks have been adopted by most manufacturing companies to extend the use of SiO_2 for the deep sub-micron devices. The incorporation of nitrogen is maybe the most common example [45, 46]. A silicon oxide/nitride stack for the gate insulation of a MOSFET will result in a higher effective permittivity of the gate oxide layer, while still taking advantage of the good Si/SiO_2 interface in the channel region.

These incremental improvements however could not delay the introduction of some new material systems for long. The oxynitrides were simply not able to

reach a high enough *k* value, which limited their downscaling possibilities. Intense research then followed to find appropriate candidates for high capacitance and low tunneling current devices. Most of the group II, III, and IV oxides, lanthanides or even perovskites have been analyzed to this extend. Yet, the integration of these new high-*k* materials for standard CMOS applications proved to be a more complex task than expected. Most of these novel insulators do not fulfill the industry requirements in terms of leakage, reliability or CMOS compatible fabrication techniques.

The first high-*k* devices that eventually went into mass production were the metal-insulator-semiconductor (MIS) and MIM capacitors for CMOS integrated circuits (ICs) or DRAM memory cells. The reason therefore is obvious: the lower complexity of the MIM structure for DRAM applications compared to the gate stack of a three-terminal device like a MOS transistor. However, one has to mention that while the leakage criteria for a gate oxide of a typical MOS transistor are relaxed, about 10^{-2} A/cm^2 @ 1 V, they are a lot stricter for DRAM capacitors, with only 10^{-7} A/cm^2 @ 1 V allowed in order to keep the information stored between two refresh cycles.

Some important industrial breakthroughs can be mentioned when discussing the introduction of high-*k* films for capacitor applications. STMicroelectronics presented their first high-*k* 3D MIM capacitor in the year 2003 [47]; they used TiN as metal electrodes and a Ta_2O_5 dielectric layer to obtain a high capacitance device. Samsung followed a year after, presenting their 90 nm stacked DRAM MIS structure [48]. In Europe, Infineon introduced the deep trench DRAM capacitor in 2004; its main figures of merit where a feature size of 70 nm, Al_2O_3 as high-*k* dielectric and aspect ratios of 75 and more for the deep trench structure [49]. All these innovations helped the manufacturers of memory cells keep the pace with Moor's law, in the age of deep sub-micron gate lengths. Some of these important milestones in the development of high-*k* dielectrics are depicted in the Figure 2.2 and Figure 2.3.

Although the high-*k* option proved to be successful for high density capacitors since the early 2000s, one main field of applications was still missing: using high-*k* dielectrics for the gate insulation of CMOS transistors. There are several reasons for this situation: as already mentioned, silicon builds a perfect interface with its native oxide; using other materials as dielectric will decrease the quality

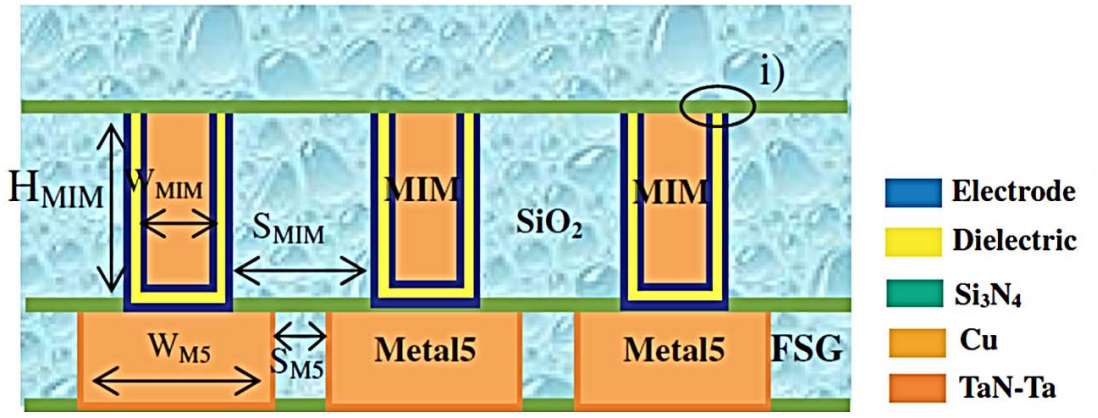

Figure 2.2: Schematic cross-section of the STMicroelectronics MIM capacitor, integrated in a 3D damascene architecture in order to increase the capacitance density (taken from [47]).

of the interface, introducing roughness, trapped charges or dipole layers near the channel interface. Changing the dielectric material will also affect the choice of the gate metallization, since polysilicon will not adhere to any insulator. Finally, the choice of the high-*k* material would also have to take into consideration the compatibility with standard CMOS fabrication techniques.

The solution could only be reported in 2007 by Intel [21]. That year they presented their heavily advertised 45 nm transistor chips; it was the first technological node that employed a high-*k* dielectric insulator and went into mass production with great success. A 3 nm thin HfO_2 layer was chosen as dielectric layer – with a dielectric constant of 25 – and a metal gate had to be employed due to the adhesion problems mentioned earlier. This approach of a high-*k* metal gate (HKMG) transistor proved to be, up to now, the best solution to help the semiconductor industry keep up the downscaling trend. A SEM image of the revolutionary 45 nm Intel HKMG transistor can be observed in Figure 2.4. The recent technology nodes revealed even more advances and novelties in the design of three terminal devices. One can mention the 2011 AMD technological node, featuring a 32 nm HKMG FinFET transistor [50] or the Intel 22 nm technological node, presented also in 2011 [51]. Introducing 3D structures for the control gate has significantly improved the device performance and helped reduce the CMOS power consumption, by lowering the supply and operating voltages. Due to this advances, the ITRS predicts no major difficulties for the near future for the next transistor technology nodes.

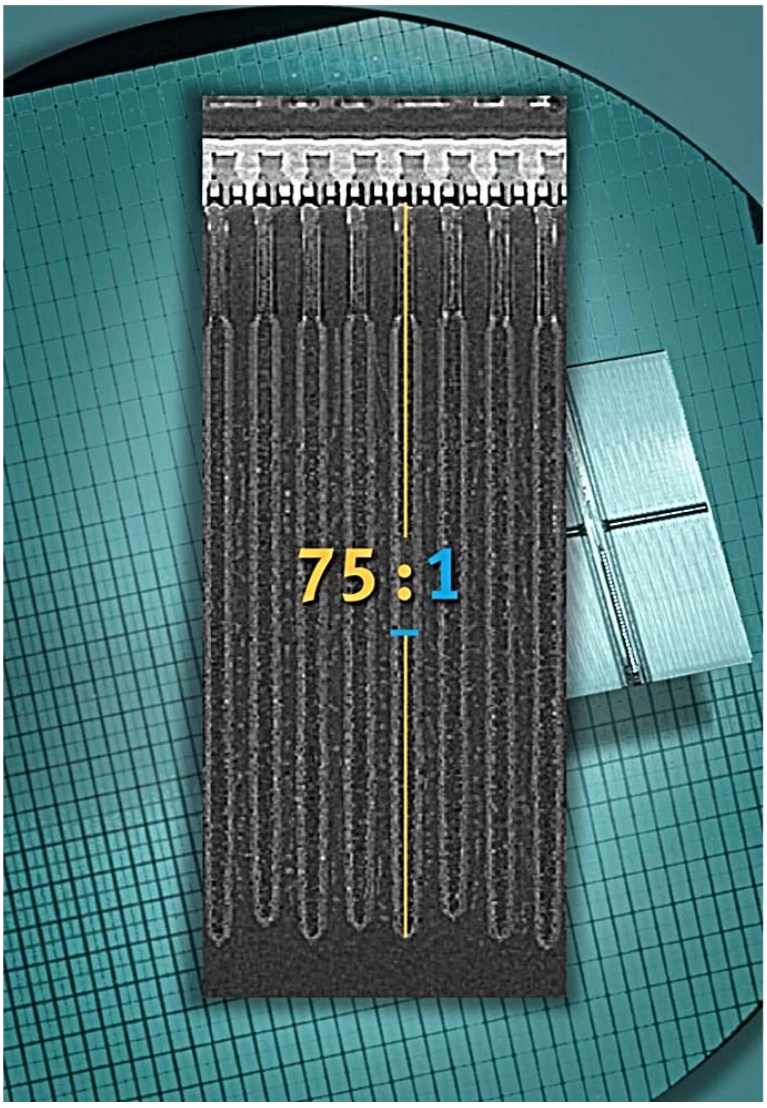

Figure 2.3: TEM picture of an early breakthrough in the field of high-*k* dielectrics, achieved by Infineon Technologies in 2004: a 70 nm DRAM cell, using a high-aspect ratio deep trench capacitor and Al_2O_3 as dielectric (taken from [49]).

Unfortunately, the situation is not that bright for DRAM memory cells and integrated MIM capacitors. As already mentioned in the previous chapter, no manufacturable solution is known to decrease the EOT of DRAM capacitors below 0.4 starting with 2016. The well-established high-*k* insulators used for CMOS transistors do not offer a dielectric constant high enough for the required equivalent oxide thickness; it is clear that HfO_2, ZrO_2 or Al_2O_3 are not suited for the next generation of higher-*k* dielectrics, for information storing applications. In order to reduce the current space requirements of IC capacitors, while keeping

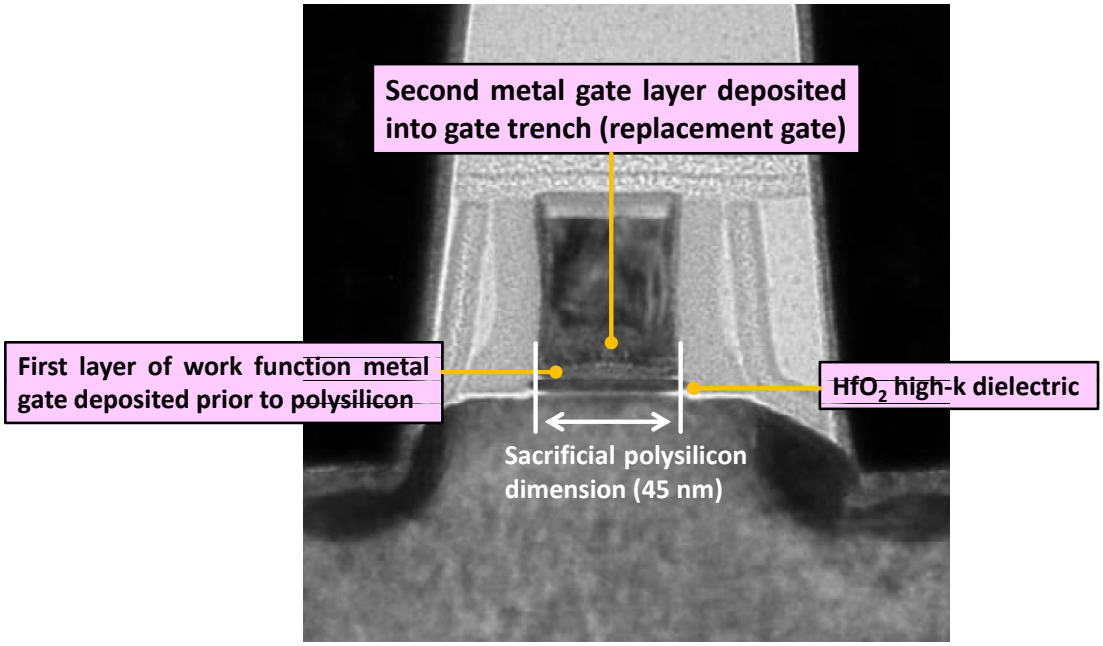

Figure 2.4: TEM picture of the first mass produced high-k metal gate (HKMG) 45 nm transistor, on strained silicon, by Intel (taken from [21]).

the performance unaffected, some new material systems have to be introduced soon.

2.2 Fabrication Techniques

In order to have a complete overview on the topic of high-k dielectrics, some words should be mentioned also on the techniques needed to grow these structures. Various fabrication methods for patterning thin layers are reported in literature [52–54]. In this section, we will first shortly describe the most important fabrication techniques currently used by research groups to grow their high-k samples – the most important research groups will be also presented in the next section – and then describe the methods employed for the fabrication of the high-k MIM capacitors that will be further analyzed and modeled in this work.

When trying to fabricate and pattern a high-k dielectric layer, independent of its application, one first has to choose a deposition technique suited for its dielectric layer and/or electrode materials. The most general classification that can be made for all currently reported deposition techniques is to divide them

in chemical vapor deposition (CVD) or CVD-like techniques and physical vapor deposition (PVD) or PVD-like techniques.

As the name already states, for CVD deposition, a volatile compound of the desired material will chemically react with other gases in the growth chamber to form a solid material on the surface of a substrate. Currently, the most used CVD techniques are metal organic chemical vapor deposition (MOCVD), atomic vapor deposition (AVD) and atomic layer deposition (ALD). The ALD method resembles very much to the classical CVD method, but in this case the chemical reaction is split into two half-reactions because the precursors are kept separate during the growth cycle. Some advantages of CVD methods are: affordable equipment price, no need for high vacuum or electric fields during growth phase, also holes or protuberances can be covered. On the downside, most reactants and byproducts generated after a CVD cycle are toxic, flammable or corrosive, high temperature is needed for growth and finally not all compounds can be grown using this method.

Opposed to CVD, where the source reactants are in gaseous form, for PVD methods one usually relies on solid or liquid source materials. Theses source atoms will enter the gaseous phase via a physical mechanism like evaporation or collision impact; usually no chemical reaction takes place in the gaseous phase. The most commonly used PVD methods are RF sputtering, molecular beam epitaxy (MBE) and evaporation. It has to be noted here that PVD techniques cannot be used to fill high aspect ratio structures and that the samples must be rotated permanently in high vacuum in order to achieve a uniform coating. As advantages for this method, we can conclude that a large variety of compounds can be grown with very exact thickness control and high adhesion. Also, the process temperature is lower and the byproducts usually environmental friendly.

Finally, we will give a short description of the high-k MIM capacitors used to analyze the leakage mechanisms in the STO layer. The SRO/STO/SRO thin film capacitors were grown in situ on oxidized silicon wafers by RF sputtering – a schematic of this fabrication technique is shown in Figure 2.5.

The reason why a PVD method has been chosen for the fabrication of our samples is straight forward: the number of stable precursors for the deposition of the

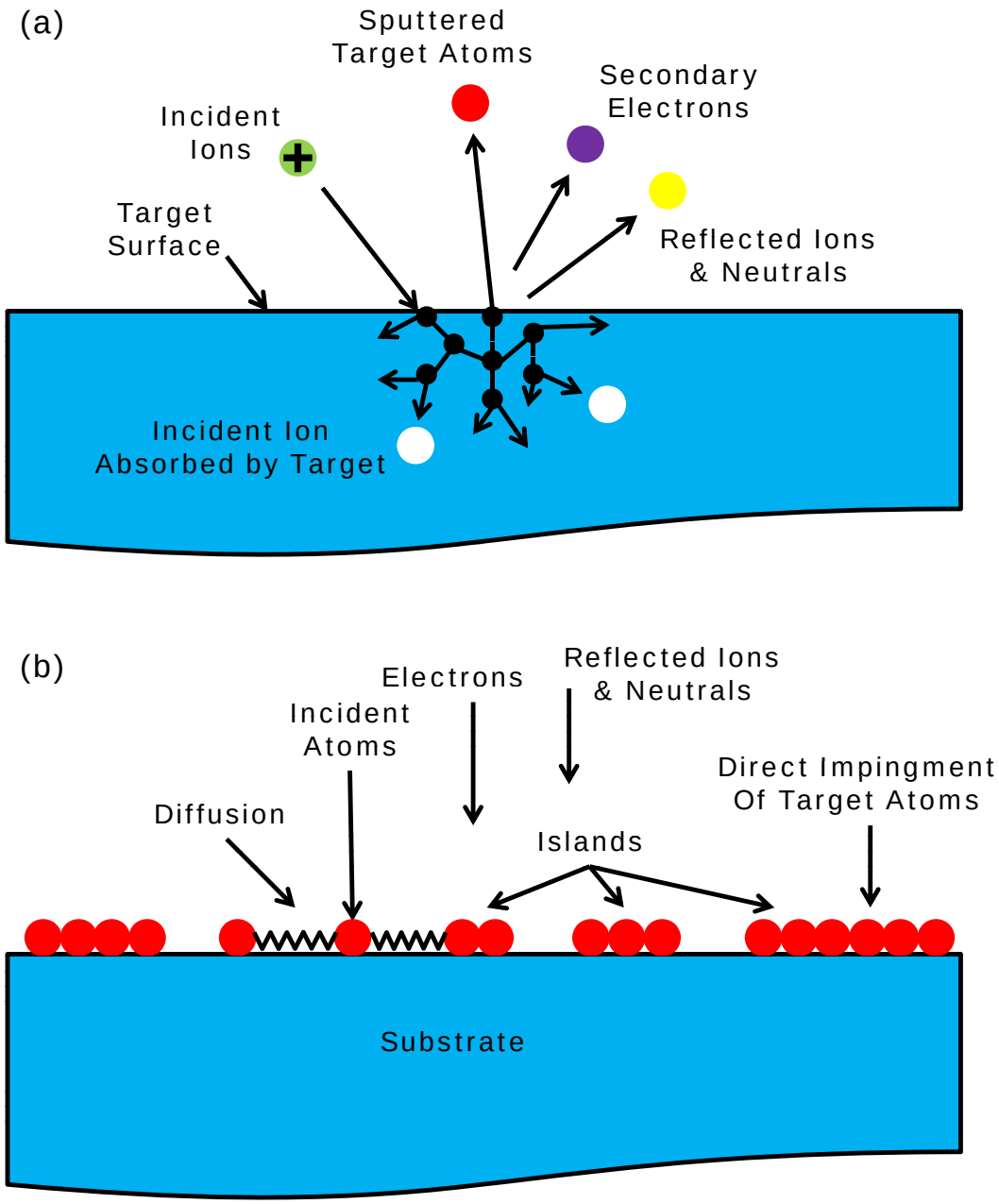

Figure 2.5: An illustration of the sputtering process: (a) Possible processes at the target site (b) Film formation on the substrate.

SRO electrodes and the STO dielectric layer is very limited. In order to ensure a good quality of the contact and insulating layers, a PVD technique was the only viable option.

For RF sputtering, a stoichiometric mixture of the source materials, SRO or STO, is placed inside a vacuum chamber together with the target oxidized silicon substrate. The chamber is flooded with an inert gas – Argon in our case – and a

RF electromagnetic wave – from the so called "RF gun" – is used to ionize the Argon gas. The sputtering reaction begins with a glow discharge and although only less than 1 per cent of the gas molecules will be ionized, this beam of Ar^+ ions is sufficient to dislocate the source material. These atoms can now flow towards the substrate, which is continuously rotating to ensure a uniform deposition.

Depending on the concentration and pressure of the inert gas in the vacuum chamber, the movement of the dislocated atoms from the target mixture can be described as ranging from a straight ballistic transport to a diffusive random walk. The choice of the inert gas is critical, since it will act as moderator for the source particles. For most of the cases, a slow movement of these particles is desired, so that most of them can reach the substrate and start nucleating on the surface; nevertheless, the compound material can also form on the target surface or in-flight, depending on process parameters. The atomic weight of the inert gas can therefore be important for efficient momentum transfer: for heavier source mixtures one would e.g. use Krypton instead of Neon.

The use of a RF gun offers some advantages over DC sputtering: power dissipation can be reduced and the charge build up that can occur when sputtering insulators or piezoelectric materials is avoided. Usually an RF matching network is used for the substrate and some magnets also help direct the sputtering beam more efficiently to the target and increase the ionization rates. For more details on this fabrication method, one can further read about the topic in e.g. [55].

The growth parameters were: substrate temperature of 550 °C under the pressure of $8 \cdot 10^{-3}$ mbar Ar. No adhesion layer was deposited prior to the growth of the SRO electrode on the SiO_2 surface, only standard prehandling processes were performed, including rinsing in acetone, isopropanol and finally water. The top electrode, grown of the same conductive oxide – SRO – as the bottom layer, has been patterned in a last processing step. For this procedure photolithography was used to deposit the Pt mask, followed by lift-off and dry etching. Further details and material properties of the fabricated MIM structures can be found in [24].

An observation has to be made, at this point, on the fabrication method: while it is clear that for any novel DRAM material system, atomic layer deposition

(ALD) is the only fabrication method that meets the industry standards for large area, high aspect ratio coverage, highly controllable thickness and high reproducibility, only very recently hybrid ALD-CVD methods for growing thin STO layers on top of SRO electrodes have been reported [28, 56].

2.3 DRAM Technology

Until now a brief overview on the historical development of the high-k devices has been given and the most frequently used fabrication methods have been presented. Also, the established applications for such materials have been mentioned, namely: nanometerscale FinFETs or planar transistors and high density capacitors for DRAM application.

Since for transistor application moderate k dielectrics like HfO_2 are enough to ensure a good performance while maintaining the downscaling trend, we will focus our study on the high density capacitor application for DRAM cells. For this reason the basic working principle of a DRAM memory cell will be shortly described below.

As one can see in Figure 2.6, the schematic of a DRAM cell is very simple and has suffered only minor changes over the last 30 years [57, 58]: one MOS transistor – referred to as the pass transistor – and one storage capacitor. The gate electrode of the pass transistor is contacted via the so-called word line, while the drain electrode is contacted using the bit line. Applying a voltage on the word line – if it is a NMOS device the voltage must be positive – will open the pass transistor and allow access to the storage capacitor. Information can then be stored as electrical charge by applying a voltage on the bit line – this is a typical write operation. To read the information stored in the capacitor, a voltage on the word line is used to open the pass transistor and the bit line is connected to a sensing circuit, to help determine if there was any charge stored in the memory block. It has to be noted that a DRAM block can only store one bit of digital information, since the read and write operations will only distinguish between two states of the memory element: either a charged capacitor – logical 1 – or a discharged capacitor – the logical 0.

The above described working principle is intended to give a basic overview on the operation mode of the memory block. An actual DRAM cell consists of

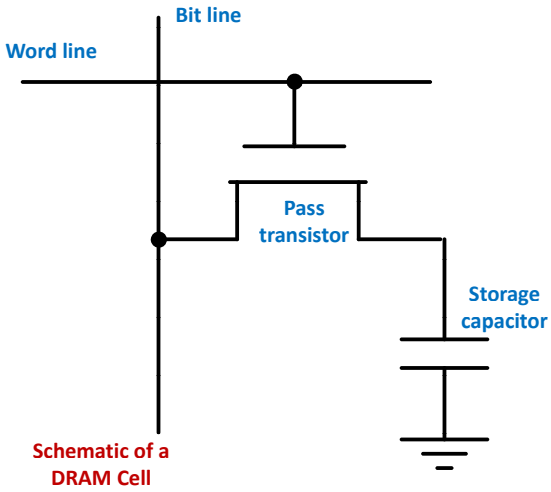

Figure 2.6: Schematic of a one-transistor-one-capacitor (1T1C) DRAM memory cell.

many such DRAM blocks, sharing together bit lines and word lines. With the help of demultiplexers the word line of an entire row of storage capacitor from such an array is accessed and the corresponding pass transistors opened. The logical output information is then lached and the bit of interested is accessed using column multiplexers. Another complication in a real implementation of a DRAM cell is the fact that actually each block can be connected to two bit lines for the read and write operation. These lines are precharged before the sensing operation to exactly half of the cell operating voltage. Depending if there was charge previously stored in the node, the voltage on one of the bit lines, which is connected to the drain of the pass transistor, will either increase or decrease. The sensing circuit will then detect the differential voltage drop between the reference bit line and the one that contacted the DRAM block. This differential voltage can then be amplified and sent to the output latch. After each read operation the value of the stored information bit is rewritten in the capacitor. A more complex schematic of a DRAM memory block is given in Figure 2.7.

If ideal storage capacitors and pass transistors could be used, the information of such a memory element would be stored indefinitely. However, there are several reasons why this is not the case: the subthreshold swing of the pass transistor can lead to charge leakage over time and thus information loss. Also the insulating dielectric of the storage capacitor can be leaky and allow charge to flow directly to the grounded electrode. Finally, another source for unreliable

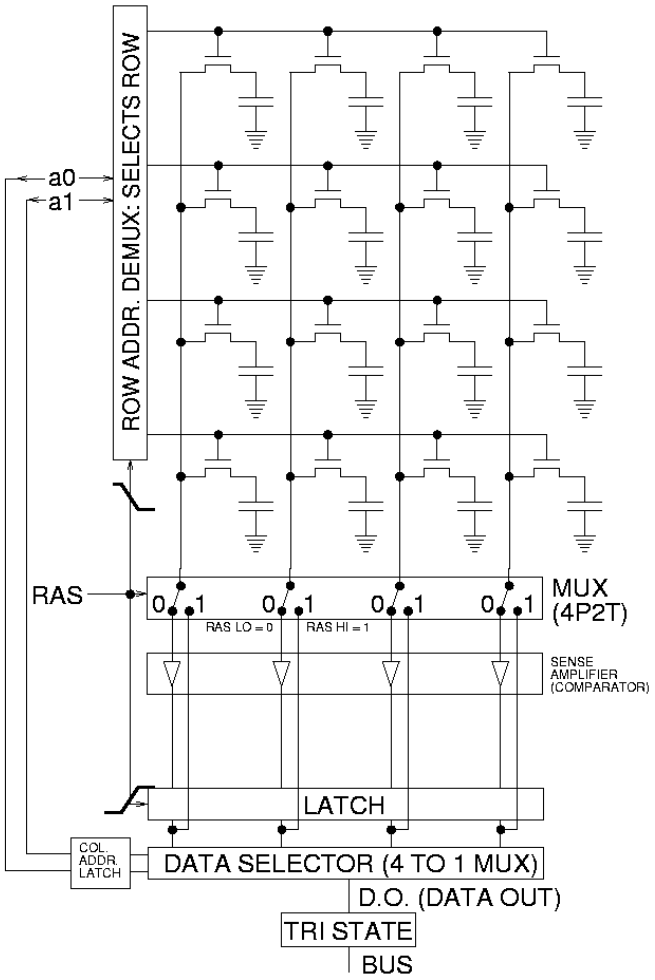

Figure 2.7: Schematic of a complex 256 kB DRAM memory block, including sensing and adressing circuitry (taken from [59]).

memory operation is the background cosmic radiation, mainly neutrons, which can modify the logic information stored. Such a scenario is often referred to as a single event upset, but its impact on the reliability of the DRAM block is not to noticeable.

This is why the information stored in a DRAM block needs to be periodically refreshed – explaining also the "dynamic" designation of this memory element. The current industry standard for the minimum retention time of information is 64 ms, so each refresh cycle must follow in a time interval of 64 ms or shorter. For completeness one should also mention that error correction codes are applied for all commercial DRAM cells, several timing schemes exist for operating large memory arrays and finally various DRAM types can be currently found on the market, like synchronous dynamic RAM, synchronous graphics RAM, pseudo-

static RAM and others. It is outside the scope of this work to further discuss such topics, but the interested reader is advised to some related literature [60–62].

Because, until a few years ago, silicon oxide was used also for the dielectric layer of the storage capacitor and the space requirements were not so strict, one could rely on thick SiO_2 layers as insulator. With its large bandgap and low defect concentrations SiO_2 was a perfect dielectric for early DRAM designs. The focus thus was directed rather on the subtreshhold swing of the pass transistor, in order to minimize charge leakage. In recent years however this is no longer true; the usage of oxynitrides for the pass transistor gate dielectric, together with the optimization of MOSFET fabrication techniques have made the subtreshhold swing a minor problem of the DRAM block. It should be mentioned however, that the technological node of the pass transistor is typically a few years behind the node of logic circuits - like processors. The reason therefore is that a pass transistor with 45 nm, 32 nm or 20 nm gate length will anyway only occupy a small fraction of the DRAM block area, compared to the area of the storage capacitor.

Looking at the simple capacitance formula for the parallel plate capacitor:

$$C = \epsilon_0 \kappa \frac{A}{t} \tag{2.3.1}$$

where ϵ_0 is the permittivity of free space, k is the dielectric permittivity, A is the capacitor area, and t is the oxide thickness, one can immediately see what parameters influence the capacitance of the storage capacitor. As it became clear that the capacitor area needs to be reduced, not so many options for achieving that remained. Vertical integration can bring some improvements in the usage of the chip area but a change of the dielectric material could not be avoided.

Introducing the high-k materials also introduced some new problems for the memory manufacturers. As Figure 2.8 shows, when the dielectric permittivity of a material increases, its bandgap will decrease making it a poor insulator. Special care must also be given to the choice of the metal electrode, since a lower bandgap can be problematic also in terms of the conduction band offset between the electrode and the insulator.

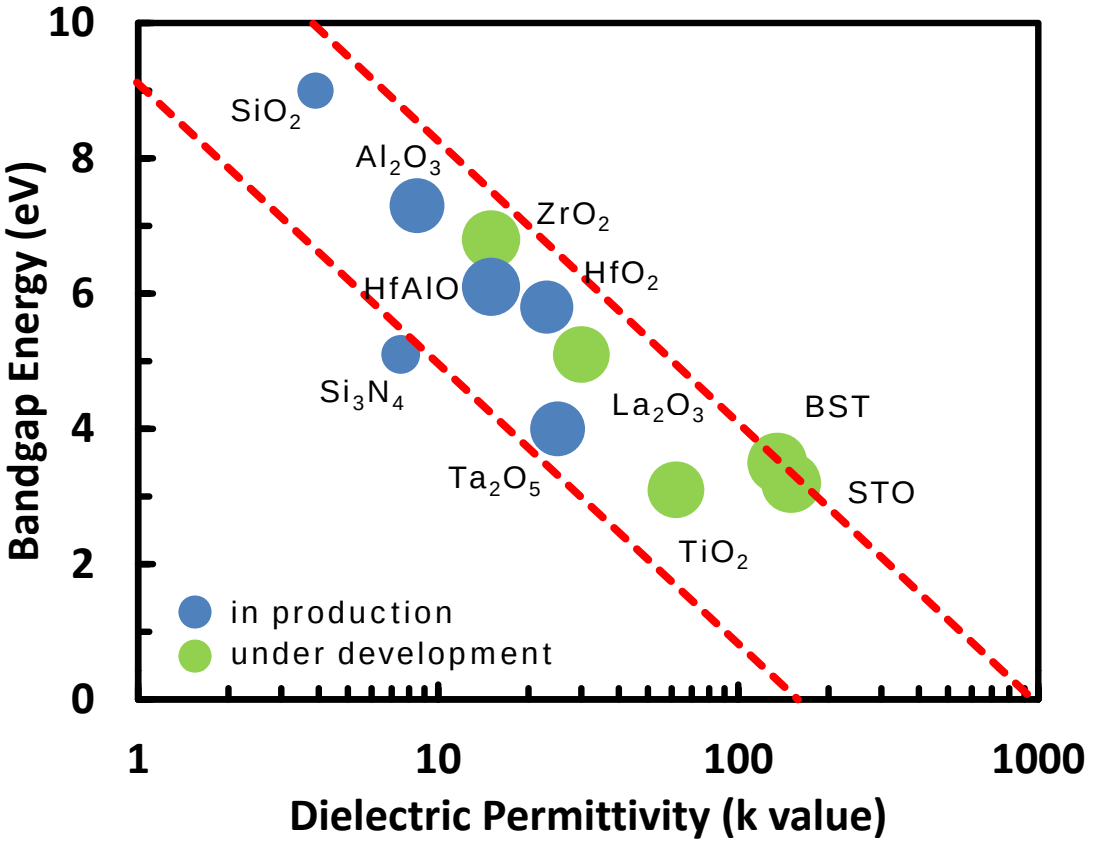

Figure 2.8: Diagram exemplifying the inverse relationship between bandgap and dielectric permittivity; thus higher-k dielectrics usually become poor insulators.

If not chosen properly, the electrode can have a workfunction close to the conduction band (CB) of the dielectric material, making thus the Schottky emission – electron emission from the metal workfunktion in the dielectric's CB – very likely. The processing temperature is an additional constraint for DRAM manufacturers: when choosing a new high-k material one has to keep in mind that for a back end of line integration (BEOL) of the high-k dielectric, the thermal budget of the CMOS process is of around 400 C [63] - higher temperatures for the processing of the dielectric layer will require additional complications to the standard fabrication steps, probably their inclusion in the front end of line (FEOL) or middle of line (MOL) process and will most surely increase the memory manufacturing cost. A table with some selected candidates, their bandgap, k value and processing temperature in shown in Figure 2.10. Finally, as already mentioned, many new candidates suffer from high defect concentrations

Compound dielectric	Process temperature	Average k-value
BiTaO	360 °C	50
$SrTiO_3$	500 °C	150
$SrTa_2O_6$	700 °C	100
$Ba_xSr_{1-x}TiO_3$	800 °C	230
$BaTaO_2N$	1000 °C	450
$CeAlO_3$	1600 °C	3000

Figure 2.9: Possible candidates for future DRAM cells dielectrics [64–68].

since the fabrication techniques are not mature enough to produce high quality uniform films.

All the above mentioned factors have shifted the focus of the charge leakage in DRAM cells from the subthreshold swing of the pass transistor to the non ideal insulating properties of the new dielectric candidates. Figure 2.10 shows the measured leakage current versus voltage for a 10 nm thin STO sample, at different temperatures. As can be observed, the leakage current at 1 V is a few orders of magnitude above the required 10^{-7} A/cm^2; fitting these I-V curves measured at different temperatures, with appropriate physical models/parameters and giving thus a reasonable explanation for the poor performance will be a main goal of the current work.

The growth of STO MIM structures, suited for DRAM application, has been previously highlighted, with a wide range of metals or conductive oxides as electrodes [70–72]; a promising choice for the capacitor electrodes, due to the low lattice mismatch and high conductivity could be SrRuO3, as reported in [23, 28]. Han *et al.* show that with an appropriate choice of the metal organic (MO) precursors and using a combined method of ALD for SrO and CVD for RuO_2, thin films of remarkable quality can be obtained. Growth of crystalline STO, lattice matched on SRO seed layers is demonstrated, with material properties close to those measured for our samples (k-value of 100 to 200) [24]. More important, coverage of high aspect ratios trenches is also demonstrated an essential requirement for new memory architectures. Popovici *et al.* also report

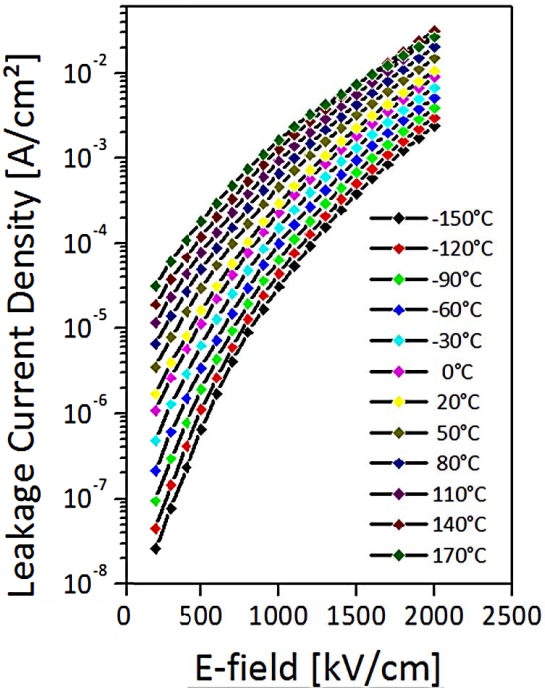

Figure 2.10: Measured I-V characteristics for the 10 nm SRO/STO/SRO sample, for different temperatures (taken from [69]).

ALD growth of STO films using Pt and TiN as electrodes [73]. They achieve a k value of 160 after a rapid temperature annealing step but face the same problems of increased leakage current – about 10^{-4} A/cm^2 @ 1 V. Some "exotic" samples are also reported by Pontes *et al.* [74] or Hofman *et al.* [75], using spin coating or sol gel methods; both report k values exceeding 200 but it has to be noted that their samples are relatively thick, at around 600 nm. It is known that the bulk k value of high-k dielectrics is significantly higher than for thin films. Also PVD methods for fabricating STO films are reported: Chiang *et al*. [76] fabricated such a MIM structure with TaN contacts, achieving a very high capacitance density of 44 fF/μm^2.

2.4 State of the Art Simulation Methods

As one can conclude, the history of high-k dielectrics started some 40 years ago. Many novel techniques have been since reported that allow for the growth and fabrication of a large number of binary and compound oxides. Experimental data on the performance of devices and structures that make use of high-k dielectrics can be found in numerous studies. However, until now, few research

groups have tried to develop theoretical frameworks that can give a complete description of the transport mechanism in such dielectric films.

Some first theoretical studies described the leakage current either as a Schottky emission of carriers at one of the electrodes or a tunneling process [77,78]. The effect of defects in the dielectric layer was taken into account by other research groups by including the Poole Frenkel (PF) emission as a possible mechanism [79, 80]. For such "single formula fit" approaches a dominant mechanism is used to model the measured leakage current for a specific bias range or regime. Often analytical expressions of the current density are evaluated, without taking into consideration electrostatic interaction or secondary leakage channels.

An improvement can be noted by Jeong *et al.* [81]: the leakage mechanism is described as a two step process - a tunneling assisted PF emission for Hafniumoxide films. In the same direction, Blank *et al.* [82] implement a multistep trap-assisted tunneling to fit the leakage current of Al_2O_3/SiO_2 samples. Most advances in the modeling of leakage currents are reported for high-k/SiO_2 gate stacks; this is not surprisingly since the first high-k transistors went into production already in 2007 and this novelty attracted a lot of attention in the research community.

Another interesting approach to model the leakage current of thin dielectric samples is to take into account possible "dead layers" [83]; however, several research groups report increased currents with no observation of the "dead layer" effect, limiting thus this approach to some material systems known to form such interfacial layers.

Some advances have been made in the recent years also for more exotic dielectric materials. Theoretical studies on the conduction of STO films with Ru electrodes [84] reveal that Schottky emission in the low electric field and Fowler Nordheim tunneling in the high electric field regime dominate the leakage for this material system, mainly due to the small barrier height at the STO/Ru interface. Kaczer *et al.* [85] concentrated their modeling study on ultrathin STO films with RuO_x and TiN as electrodes; in order to determine the ultimate scaling limits of their ultrathin MIM structures, the intrinsic direct tunneling mechanism is analyzed in detail.

Manger *et al.* [86] characterized the leakage in their STO films with TiN electrodes as field assisted, thermally activated hopping between trap sites. While their single equation fit can reproduce fairly well the measured J-V-T characteristics over an interval of 75 K, applying it to our samples fails to reproduce the measured curves. This is a first hint that for the SRO/STO/SRO samples a complex model is needed, which takes into account leakage mechanisms associated to the bulk STO films, as well as to the STO/SRO interface.

Most of the studies mentioned above rely on analytical expressions or numerical approximations of the dominant mechanism that is responsible for the unwanted leakage current. Such approaches can be therefore used only for specific material systems, where the dominant mechanism has been identified. They also fail to deliver trustworthy results when more than one physical process is responsible for the leakage behavior.

On the other hand, advances in numerical simulation programs allow the user to couple multiple processes, in order to give an accurate description of the transport mechanism. To our knowledge, this approach of extending an advanced drift-diffusion simulator to take into account also various other leakage mechanisms that are typical for high-k dielectrics, is a new one. We will give further details and stress out the advantages of this hybrid simulation technique in the following sections.

There is however another modeling approach that deserves some attention and discussion: the statistical approach via Monte Carlo methods. In this case, no assumption or knowledge of the dominant transport mechanism is needed; all possible transport processes can be included in the model and executing a stochastic algorithm – Monte Carlo in this case – will determine the total leakage current. There are of course multiple advantages of this method: including many possible transport processes, although not likely for a specific material system, makes this approach suited for a large spectrum of binary and compound oxides. Also, all aspects of the transport across the dielectric film can be included, starting from the charge injection at one electrode, multistep trap-assisted or PF tunneling and collection at the opposite electrode.

Okuyama *et al*. [87] presented a first framework capable of duplicating measured data through MIM structures with a Monte Carlo method. They already include

in their work elastic and inelastic tunneling processes through trap sites in the dielectric and use a more detailed description of the charge injecting process.

Vandelli *et al.* [88] also present a statistical approach of simulating the leakage currents through silicon oxide/high-*k* dielectric stacks for nonvolatile memory application. Their study underlines the importance of simulation studies for the optimization of FLASH memory cells.

Finally Jegert *et al.* [39] show remarkable results for the reliability study of $TiN/ZrO_2/TiN$ material system for DRAM application.

Although the above mentioned studies can bring new insights on the topic of high-*k* dielectrics reliability, one should also briefly mention the limitations of this technique. The large simulation time and vast resources needed make it not well suited for industry applications, where simulation time can be a critical factor. Also, complex geometries of the structures to be analyzed are still an issue. Most Monte Carlo studies concentrate on planar MIM structures, realistic 3 D trench geometries under realistic bias conditions being ignored for the moment.

Our believe is that a Monte Carlo framework is very well suited for a first principles study on the leakage mechanisms of new material systems. Such a study can also be used to give physically meaningful approximations on some parameters that are hard or impossible to measure with experimental methods – like trap concentrations or tunneling parameters. Once a good agreement between measured and simulation data can be obtained, the framework and its parameters can be "exported" in a drift diffusion environment modified accordingly. Superior speed, robustness, arbitrary geometries, modeling of simple circuits, post-processing capabilities are just some of the advantages this strategy can bring. We will bring arguments and elaborate on this approach in the following chapters.

3 Simulation Methods

We have presented until now an overview on the topic of high-*k* dielectrics covering the main application areas, a brief historical development, we have summarized some of the most important fabrication techniques and have spend some words on the advances in the area of simulating leakage currents for such material systems.

Since the main goal of this work is to concentrate on the simulation methods one can employ to analyze, understand and predict the leakage current in novel material systems, we will firstly discuss in more detail the simulation methods employed.

3.1 Introduction to kinetic Monte Carlo

Monte Carlo (MC) methods have been used over the last decades for a large number of computational problems in various fields of expertise. Through the use of random numbers and stochastic algorithms, one can solve complex problems ranging from chemical, solid state or nuclear physics, mathematics to engineering or even economics. In the classical implementation, samples are drawn from a probability distribution, e.g. the Boltzman distribution, and the steady state or equilibrium properties of the system can then be analyzed. Variations of the classical implementation may include quantum, volumetric or kinetic Monte Carlo, each of the above mentioned methods having their advantages for certain model systems.

We will focus on the kinetic Monte Carlo (kMC) variation in the following, shortly discussing its advantages and disadvantages over other Monte Carlo methods and also comparing it to alternative computational techniques - that

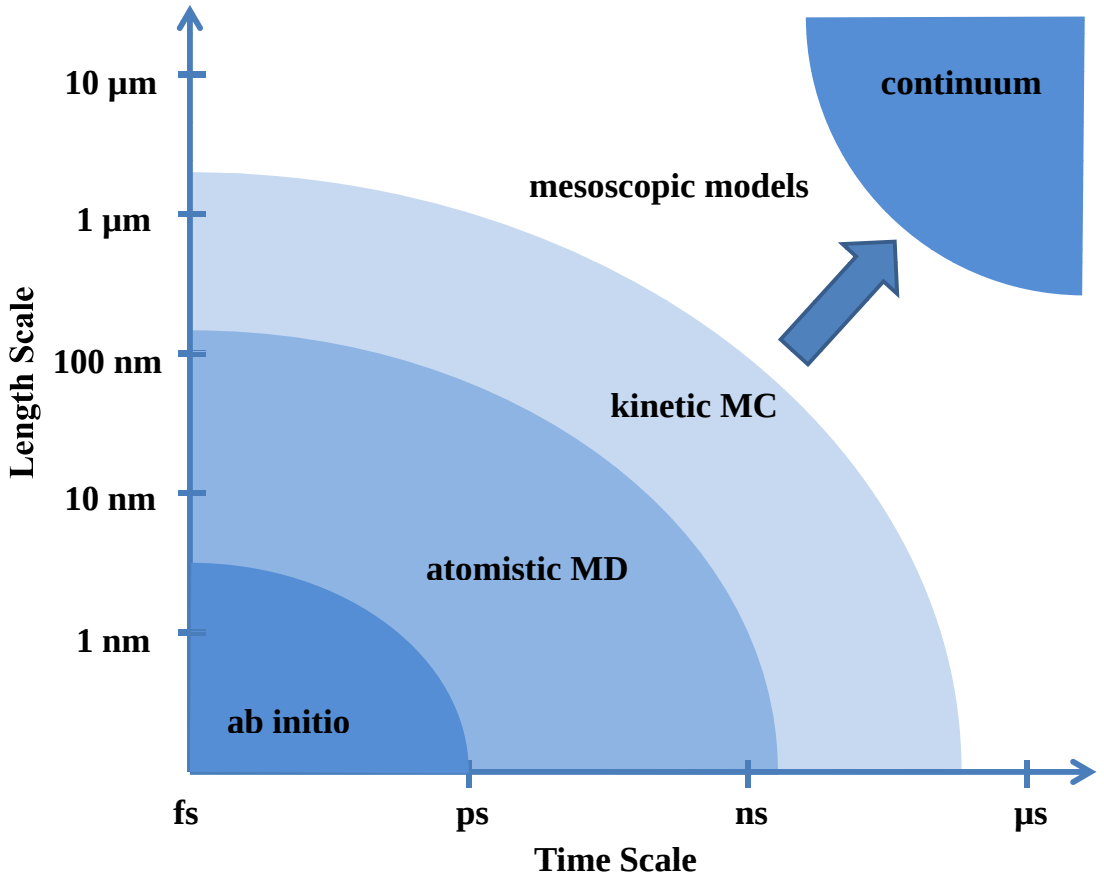

Figure 3.1: Comparison of different Monte Carlo simulation techniques, highlighting the typical length and time scales that can be covered with each of these variations.

do not employ random numbers but still can be used to predict time evolution and dynamics of multiparticle systems.

Let us first start with an enumeration of some selected simulation techniques most commonly used in computational chemistry and physics. As one can observe in Figure 3.1, these methods are plotted in the graph according to two quantities of interest: the time scales covered by the specific method and the length scales. Covering the very small time and length scales, one can enumerate the atomistic models. Some widely used techniques are the *ab initio* Molecular Dynamics (MD) or the quantum Monte Carlo frameworks. While these methods can be very useful in deriving and predicting material properties and parameters, like defect energy levels, defect mobilities, interstitials or surface potentials, with minimum input parameters - usually the atomic structure and interatomic

interactions - their application range is quite limited. Only rapid processes can be simulated, with severe limitations on the size of the simulation cluster. Moving to microscopic models, one can name the classical Molecular Dynamics (MD), Metropolis Monte Carlo (MMC) or kinetic Monte Carlo (kMC) techniques. Further details on this class of algorithms will be given shortly. Bridging the gap between microscopic and continuum models, only some problem-specific approaches exist. Monte Carlo Potts Model can be useful to study grain structures in crystalline materials or dislocation dynamics to analyze deformation processes. Still, a general model that covers the mesoscopic range would be highly desirable for solid state physicists, as well as chemists and material science engineers. Finally, in the macroscopic range, the continuum approach makes use of some constitutive relations and solves a system of partial differential equations (PDE), with the help of some finite elements or finite volumes method. Relevant for electron transport are, among others, the Drift Diffusion model (DD), the Thermodynamic and Hydrodynamic models. The continuum approach will be discussed in detail in the next chapter.

Since the goal of our work is to model the leakage current through thin dielectric films, and we can already assume that a large number of defects can be found in these films - experimental studies suggest this fact - we will choose to focus on a microscopic model at first. This approach enables us to threat the electrons as particles, impurities as point-defects and should allow us to extract some material properties.

We recall that the most suited microscopic models are the Molecular Dynamics, the Metropolis Monte Carlo and the kinetic Monte Carlo technique. Let us start with a first analysis of the Molecular Dynamics framework.

The MD framework is a deterministic simulation procedure that allows one to compute the dynamical behavior of a multiparticle system. The initial conditions of the system need to be given and also the interacting potential between particles is assumed known in order to calculate the driving forces between the particles of the system. Once these premises are fulfilled, the evolution of the system can be computed based on the classical equation of motion or Newtons second law to be more precise:

$$\mathbf{F} = \frac{\mathrm{d}\mathbf{p}}{\mathrm{d}t} = m\frac{\mathrm{d}\mathbf{v}}{\mathrm{d}t} = m\mathbf{a}. \tag{3.1.1}$$

This equation is solved for all particles of the system, usually with some optimized numerical method.

The main advantages of this method are the reduced input information needed and the capability of the model to predict even new physical configurations/phenomena based on that input. The method is highly accurate for atomic-level simulations but suffers from limited simulation range in the space and time domain. Since it needs to resolve vibrational modes at atomistic level, the time step is usually in the order of fs for MD simulations; thus the total simulation time rarely exceeds 100 ns. In the space domain, usually several millions atoms can be resolved which translates into some nanometer scale atomic cells. Electrons are introduced in the system through the potential energy surface, under the assumption of the Born-Oppenheimer approximation. A disadvantage of the method is that the potential energy surface for complex systems can in most cases only be approximated - the quality of the solution for realistic simulations depends on the availability and choice of these functions for the potential energy surface. Another source of inaccuracy is the assumption of classical motion for the particles, obeying Newtons laws. As the thermal de Broglie wavelength:

$$\Lambda_{th} = \frac{h}{\sqrt{2\pi k_B T}} \tag{3.1.2}$$

- where h and k_B are the Planck and Boltzmann constants, respectively - becomes larger than the interparticle distance, the MD method will fail to deliver a physically meaningful solution. This is usually the case for very light atoms, where the thermal de Broglie wavelength approaches 1 Angstrom. Some state-of-the-art simulation studies using MD methods can be found by an interested reader in [89, 90].

If deterministic methods have such disadvantages, one may think of using stochastic methods to study a multiparticle system. Maybe the most known Monte Carlo technique is the so called Metropolis Monte Carlo method. This method allows one to study equilibrium properties of a system; it can generate the final states according to a large variety of statistical-mechanical distributions.

Usually a random walk (Markov chain) is performed in the phase space and the energy of the initial and final states is computed. Since the goal of the method is to find the equilibrium configuration of the system, any state with lower energy than the initial state is accepted as a valid step in the Markov state. States with higher energy can be also accepted, based on a random number pick, with a probability distribution equal to the ratios of the initial and final state probabilities. In case of the Metropolis MC, we usually use the Boltzmann distribution, so the random choice of selecting a next state with higher energy has a probability proportional to:

$$P \propto \exp(-\frac{U_{nm}}{k_B T}). \tag{3.1.3}$$

Here $U_{nm} = U_n - U_m$, U_m is the potential energy of the initial state and U_n the potential energy of the final state, which is higher. It can be proven in this case, that the transition probability also satisfies a detailed balance condition or in other words:

$$\mathrm{W}(n \to m)\mathrm{P}(n,t) = \mathrm{W}(m \to n)\mathrm{P}(m,t) \tag{3.1.4}$$

where $\mathrm{P}(m,t)$ is the probability of finding the system under observation in state m at time t and $\mathrm{W}(m \to n,t)$ is the probabilty that a transition from state m to state n will take place in the unit time interval.

Although the equilibrium state of a system can be found in a straight forward way, starting from an arbitrary initial state, the Metropolis MC technique fails to predict the dynamics of the system. It cannot predict the correct time evolution, nor can it give any information of the real time scale of the simulation. For additional examples of the Metropolis MC method one is advised to read [91, 92].

It seems thus that a stochastic method that can also predict the evolution of a dynamic system would be the perfect choice for modeling systems that are out of equilibrium, like the current flow through a leaky insulator. As one can now probably guess, this is exactly what a kinetic Monte Carlo (kMC) algorithm does; it combines the advantages of both Molecular Dynamics and Metropolis Monte Carlo. The fundamental idea of kMC is to use transition rates instead of energy

states, according to some stochastic method and also to link these transition rates to the physical system time. It has to be observed that a prior knowledge of all the important transition rates in the system is required. This transition rates can be deduced either from analytical physical models, can be measured in experiments or can be output of ab initio calculations.

3.2 History of kinetic Monte Carlo

The Monte Carlo methods were first developed at the Los Alamos National Laboratory, in the late 1940s, in the framework of the Manhattan project, mainly to help study the neutron diffusion and other thermonuclear reactions. The exact reason for the choice of the Monte Carlo name is still disputed: some argue that the uncle of S. Ulam one of the pioneers in this field used to travel frequently to the Monte Carlo Casino for gambling, while others attribute the name to Ulams own passion for poker.

The first publication that mentions the Monte Carlo name for the stochastic method is the now famous *Journal of the American Statistical Association* by N. Metropolis and S. Ulam published in 1949 [93]. It was followed after four years by maybe one of the most important papers of the last century, in the field of stochastic methods, the Equation of State Calculations by Fast Computing Machines [94].

These articles concentrated on calculating properties for systems consisting of individual interacting particles; good results were obtained using a 2D rigid sphere approach and implementing it on the first electronic computing machines of that time.

But as already mentioned, the method proposed by Metropolis *et al.* cannot give the correct time evolution of a system. Researchers therefore soon started to develop alternative stochastic techniques that could also predict the dynamics of a system. A first step in this direction was made by Flinn and McManus in 1961 [95]. They analyze the order-disoder transformation in crystal lattices and can report some conclusions on the kinetics of the transformation - the rate-limiting process for the diffusion in the ordered system appears to be the hopping of vacancies to neighboring lattice sites. The concept of transition rates

and probabilities is introduced in this paper, however a systematic derivation of the time-scale for the physical processes under investigation is still missing.

Five years later, Young and Elcock [96] present their own study on the migration of vacancies in binary alloys. The variation of Monte Carlo Method used for the simulation part can be viewed as the first kinetic Monte Carlo implementation, with physically meaningful conditions and criteria for choosing a next transition and incrementing the simulation time.

Finally, Bortz, Kalos and Lebowitz [97] present their Monte Carlo algorithm, for the simulation of Ising spin systems. This implementation can be viewed maybe as the prototype for all the following studies in the field of dynamic Monte Carlo simulations. The elegant method for choosing the next transition and time step enables them to report a speed up of more than 10 times compared to the other published studies.

When discussing about the early days of the kinetic Monte Carlo development, one should also mention Beeler's et al. [98] study on the annealing of radiation damage, one very interesting and practical implementation of this stochastic framework that paved the way for many more research studies in this field [99, 100].

Over the last decades, this method for modeling the dynamic evolution of complex multiparticle systems became increasingly appealing for a wide variety of research fields in chemistry or material science. The simulation of surface absorption [101, 102], protein folding, particle diffusion, epitaxial growth of thin material layers [103–106] are just some examples among many others. The interested reader is finally advised for a more recent review article [107] on this topic, which enumerates many interesting implementations for the above mentioned method.

3.3 The kMC Algorithm

We have given until now a broad overview on the kinetic Monte Carlo method and have underlined its advantages over other deterministic or stochastic frameworks. In the following, we will present the actual implementation of the kMC algorithm used to simulate the leakage currents through the high-k dielectric

STO layers. The procedure is based on the numerical approach presented by D. Gillespie in [108, 109].

A straightforward way of calculating the time evolution of the particle flow in a multiparticle system, would be to solve the coupled partial differential equations that describe the transport of the particles involved: one example would be solving the electron and hole continuity equation in a semiconductor device. The time-rate-of-change of the electron or hole concentrations would then be expressed as a continuous, single valued function of time. Of course, if the transport of the particles in the analyzed system is governed by more complex equations, it is impossible to compute an analytical solution and one has to rely on numerical methods to determine an approximate solution.

The alternative approach, to the above mentioned deterministic method, is to use a stochastic formulation. Instead of defining generation and recombination rates e.g. in the electron or hole continuity equation, one can think of using probabilities per unit time. In this framework, the time evolution of the multiparticle system is governed by a master equation, which describes the probability of finding a specific particle at a specific moment in time. Analytically, one can formulate the stochastic solution as a single differential-difference equation that contains all particle species, particles and time as variables. The temporal behavior can be viewed as a Markov chain of random events involving the different particles of the system.

Some remarks should be made before discussing the master equation and deriving the choice for the next step in the random walk. Both the deterministic and the stochastic approach are correct and equivalent from a physical perspective, it is up to the user which of the two methods to use in an attempt to solve a given problem. An argument that did speak for a deterministic solution in the past, was the elegance and effectiveness of a closed analytical formulation for the problem of interest. But this advantage usually disappears, as mentioned above, for systems containing several particles that can undergo complex processes or transitions. In such a case one has to rely again on numerical methods to find a solution, similar as in the case of the stochastic approach.

To conclude, for the study of complex multiparticle systems, a deterministic or a stochastic approach are equivalent from a physical but also from a mathematical

point of view both methods will rely on numerical methods to generate a solution.

3.3.1 The Reaction Probability Density Function

One formulation of the so called *masterequation* for the stochastic approach, as deduced by McQuarrie et al. [110], will concentrate on the probability of finding X_1 particles of the species S_1, , X_N particles of the species S_N in our volume V of interest, at a given time t:

$$\mathrm{P}(X_1, X_2, ..., X_N; t) \tag{3.3.1}$$

and the corresponding k^{th} moments:

$$X_i^{(k)}(t) = \sum_{X_1=0}^{\infty} \cdots \sum_{X_N=0}^{\infty} X_i^{(k)} \mathrm{P}(X_1, X_2, ..., X_N; t) \quad (i = 1, ..., N; k = 1, 2, ...). \tag{3.3.2}$$

Of significance are certainly the first and second moments:

$$X_i^{(1)}(t) \tag{3.3.3}$$

$$\Delta_i(t) = \left\{ X_i^{(2)}(t) - \left[X_i^{(1)}(t) \right]^2 \right\}^{1/2} \tag{3.3.4}$$

because they give the average number of X_i particles of species S_i, at the time t, inside our volume V - equation 3.3.3 - and the RMS value of the variations around this number - equation 3.3.4.

The only hypothesis we make within this framework is to assume that each particle transition R_μ from one state - let state denote energy, position, etc. - to another can be characterized by a transition parameter c_μ as follows:

$$\begin{aligned} c_\mu \delta t = {} & \text{first order average probability that an arbitrary number of particles} \\ & \text{will carry out } R_\mu \text{ transitions within the next time interval } \delta t. \end{aligned} \tag{3.3.5}$$

A reader familiarized with probability theory will however observe, that solving the master equation and deriving its moments is not a trivial task. Finding an analytical closed form is equally as challenging as trying to construct a numeric approximation, even under the assumption formulated in equation 3.3.5.

A promising alternative to calculating the correct time evolution of a complex system is to try and simulate the whole Markov chain of events, which is essentially depicted in equation 3.3.1, in an analytical formulation, rather than explicitly solve the time-dependent probability function for all the particles of all the species interacting in our system. In the following, we will describe the simulation framework capable of simulating such random walks, in the space of X_i particles of S_i species; this framework will subsequently be used to model the leakage behavior of our high-k samples.

One elegant way of constructing an algorithm, capable of carrying out an arbitrary number of Markov walks, that avoids a complex solution derivation from the master equation has been proposed in [108]. It relies on the assumption of equation 3.3.5 and makes use of the so called reaction probability density:

$$\begin{aligned} P(\tau,\mu)d\tau = {} & \text{probability at time } t \text{ that the next } R_\mu \text{ reaction will occur} \\ & \text{within the differential time interval } (t+\tau, t+\tau+d\tau). \end{aligned} \tag{3.3.6}$$

Here we denote with μ the discrete set of possible transitions or reactions $\mu = 1, ..., M$ between system states and with $\tau \in [0, \infty)$ the continuous time variable of our system. It will be our task to develop an exact formulation of this joint probability density in the following.

Let us start by defining some important state variables:

$$\begin{aligned} h_\mu = {} & \text{number of particles found in volume } V, \text{ at the time } t, \\ & \text{which can undergo a } R_\mu \text{ transition.} \end{aligned} \tag{3.3.7}$$

Then, using both equation 3.3.5 and equation 3.3.6, one can write:

$$h_\mu c_\mu \delta t = \text{first order probability that an } R_\mu \text{ reaction will take place in volume } V, \text{ in the time interval } t. \tag{3.3.8}$$

Obviously h_μ will be a function of the total number X_i of particles that can be found in the system at the time t. We can now rewrite the probability density function in equation 3.3.6 as a product between $P_0(\tau)$, the probability that no reaction will occur between the times $(t, t+\tau)$ and the probability that an R_μ reaction will occur in the next infinitesimal time interval $(t+\tau, t+\tau+d\tau)$, denoted by the second term in the equation below:

$$P(\tau, \mu)d\tau = P_0(\tau) \cdot h_\mu c_\mu d\tau. \tag{3.3.9}$$

To calculate the first term of equation 3.3.9, we will make use of some standard probability theory schemes. Let us divide the time interval between t and $t+\tau$ into Z equidistant subintervals $\delta = \tau/Z$. We can now calculate what is the probability that no transition $R_1, , R_M$ will take place in the first subinterval between t and $t+\delta$; since we assume a random chain of events, the probability that no transition will take place in the next δ interval remains unchanged. For Z such subintervals $(t, t+\delta), (t, t+2\delta), , (t, t+\tau)$ the total probability can then be written as:

$$\begin{aligned} P_0(\tau) &= \left[1 - \sum_\mu h_\nu c_\mu \delta + o(\delta)\right]^Z \\ &= \left[1 - \sum_\mu h_\mu c_\mu \tau/Z + o(Z^{-1})\right]^Z . \end{aligned} \tag{3.3.10}$$

If we let Z become infinitely large and make use of the known equality:

$$\lim_{n\to\infty}(1 + \frac{x}{n})^n = e^x \tag{3.3.11}$$

we can write the probability $P_0(\tau)$ thus as:

$$P_0(\tau) = \exp\left[-\sum_{\mu=1}^{M} h_\mu c_\mu \tau\right] \tag{3.3.12}$$

and can conclude that the total probability density function described by equation 3.3.6 is equal to:

$$P(\tau, \mu) = h_\mu c_\mu \exp\left[-\sum_{\mu=1}^{M} h_\mu c_\mu \tau\right]. \tag{3.3.13}$$

For completeness we shall mention that the function defined in equation 3.3.13 is normalized over the definition domain spanned by the continuous time variable $0 \leq t < \infty$ and the discrete transition variable $1 \leq \mu < M$, a property that can easily be proven.

3.3.2 Choosing a Transition and Time Step

The main idea of the presented approach is to simulate now a Markov chain of events that obeys the probability density function described in equation 3.3.13. Before discussing an implementation of the algorithm used to generate these random walks, we first have to spend a few words on the method needed to calculate a pair of variables (τ, μ) according to the joint probability function given in equation 3.3.13.

We will start by making use of the fact that a two variable probability density can be always written [111] as a product between two single variable probability density functions:

$$P(\tau, \mu) = P_1(\tau) \cdot P_2(\mu|\tau). \tag{3.3.14}$$

Here we have denoted with P_1 the probability that an arbitrary transition will occur in the time interval $(t + \tau, t + \tau + d\tau)$ and with P_2 the probability that the next transition will be precisely R_μ.

Making some simple assumptions we can now derive the expressions for P_1 and P_2. P_1 can be calculated by simply summing $P(\tau, \mu)$ over all possible transitions and is therefore:

$$P_1(\tau) = \sum_{\mu=1}^{M} P(\tau, \mu). \tag{3.3.15}$$

Inserting the above expression in equation 3.3.14 one can obtain for P_2:

$$P_2(\mu|\tau) = P(\tau, \mu) / \sum_{\mu=1}^{M} P(\tau, \mu). \tag{3.3.16}$$

We have now the derived P_1 and P_2 as functions of $P(\tau, \mu)$. Using the simplification:

$$p_\mu = h_\mu c_\mu \qquad (\mu = 1, 2, ..., M), \tag{3.3.17}$$

$$p = \sum_{\mu=1}^{M} p_\mu = \sum_{\mu=1}^{M} h_\mu c_\mu \tag{3.3.18}$$

we obtain the following equations:

$$P_1(\tau) = p \exp(-a\tau) \qquad (0 \leq \tau < \infty) \tag{3.3.19}$$

$$P_2(\mu|\tau) = p_\mu / p \qquad (\mu = 1, 2, ..., M). \tag{3.3.20}$$

To shortly resume the above results: we will first generate a random continuous value t according to the probability density function in P_1 and then generate a discrete value μ according to P_2; then the pair (t, μ) must necessarily satisfy equation 3.3.13. Thus, the actual task before us is to choose a method capable of generating random numbers according to the above given instructions; we will discuss it in the following section.

3.3.3 Generating Random Numbers According to Arbitrary Probability Density Functions

For most numerical algorithms today, the generation of uniform random numbers in the unit interval is a trivial task; it can be accomplished even by pocket

calculators with reasonable efficiency. The situation gets more complicated however if random numbers are desired picked with a custom probability density function over an arbitrary interval.

Two methods that are easy to implement can be used for this task: the inversion and the rejection method. A detailed derivation for both methods can be found in [111], we will only briefly describe the inversion method, since this method was used for the kMC simulations that will be presented in the next sections.

Let us start with some basic probability theory notions. If we have a probability density function $P(x)$, then it follows that $P(y)dy$ is the probability that the random number x will be found between y and $y + dy$.

If we decide however, to integrate $P(y)dy$ we will obtain what is called the probability distribution function:

$$F(x) = \int_{-\infty}^{x} P(y)dy. \tag{3.3.21}$$

We can thus interpret $F(x_0)$ as the probability that x will be less than x_0. The distribution function has some interesting properties, since:

$$F(-\infty) = 0 \quad \text{and} \quad F(+\infty) = 1. \tag{3.3.22}$$

Similar to the normalization condition for e.g. Schrödinger′s equation, the above equalities imply that every randomly picked number has to be somewhere between $-\infty$ and $+\infty$. We can also observe that the distribution function has to be a strictly increasing function. Due to the above mentioned properties one can be sure that $F(x_0)dx$ will always have an inverse function - this represents in principle also the core of the inversion method. If one wants a random number x according to $P(x)$, it is enough to generate a uniform random number m in the unit interval and then calculate:

$$x = F^{-1}(m). \tag{3.3.23}$$

Figure 3.2 illustrates this principle in a straight-forward way. Now that we have derived the method, we can apply it to generate our random numbers according

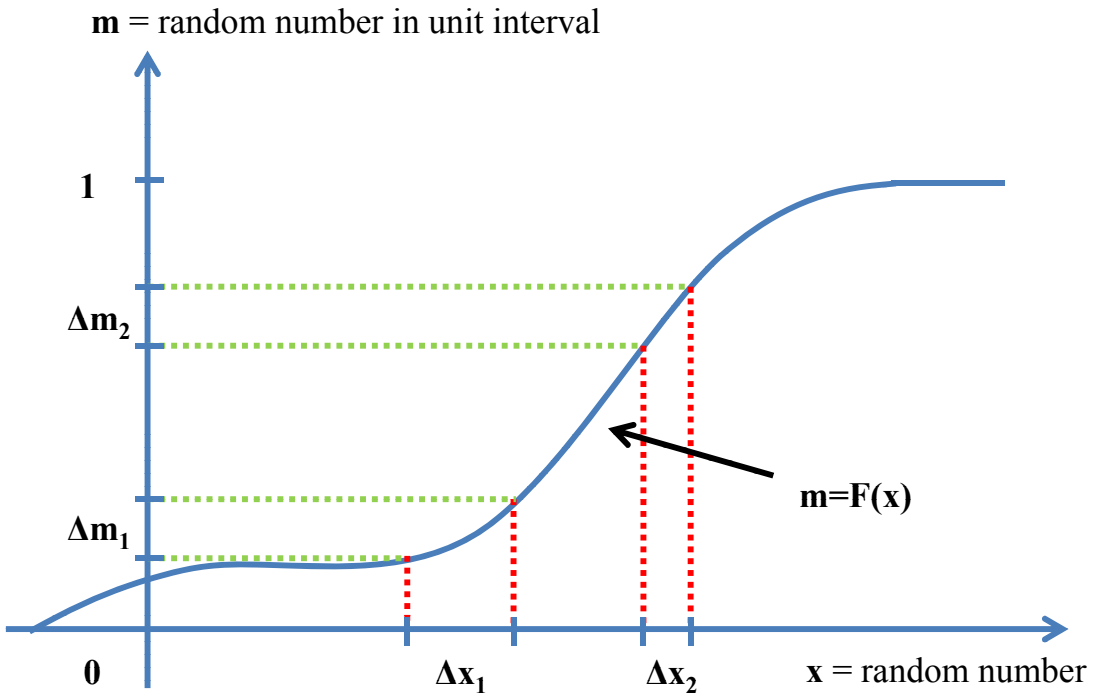

Figure 3.2: The principle of the Inversion Method (redrawn from [111]).

to equation 3.3.19 and 3.3.20. Assume that we need to generate a number x as stated by 3.3.19:

$$\begin{aligned} P(x) &= A\exp(-Ax) \quad \text{for } 0 \leq x < \infty \\ &= 0 \qquad\qquad\quad \text{otherwise.} \end{aligned} \tag{3.3.24}$$

We can identify $F(x) = 1 - \exp(-Ax)$. If $F(x) = m$, we can invert F according to equation 3.3.23 and we finally obtain:

$$x = (1/A)\ln(1/m) \tag{3.3.25}$$

The above formula allows us to generate a random number as required by the density function in equation 3.3.19 by simply picking m - a uniform random number in the unit interval and performing transformation 3.3.25 afterward.

We now have to derive the equivalent formula for the case of the discrete probability density function given in equation 3.3.20. Analogous to the continuous

case, let $P(i)$ be an arbitrary chosen density function. $P(j)$ is now the probability that i will be equal j. The distribution function can be written as:

$$F(i) = \sum_{j=-\infty}^{i} P(j). \tag{3.3.26}$$

To apply the inversion method, one has to draw again a uniform random number m and chose for i the value that fulfills:

$$F(i-1) < m \leq F(i). \tag{3.3.27}$$

To conclude, if we want to generate a discrete random number i according to equation 3.3.20:

$$\begin{aligned} P(i) &= a_i / \sum_{k=1}^{M} a_k \quad \text{for } \; i = 1, 2, ...M \\ &= 0 \qquad\qquad\quad \text{otherwise} \end{aligned} \tag{3.3.28}$$

we simply will choose m and find the integer i that satisfies:

$$\sum_{j=1}^{i-1} a_j < m \sum_{k=1}^{M} a_k \leq \sum_{j=1}^{i} a_j. \tag{3.3.29}$$

We have now given two simple rules for generating the random pair (τ, μ) needed to perform our random walk only making use of two uniform random numbers in the unit interval and some algebraic manipulations. Next we will present a simple algorithm capable of simulating the time evolution of the master equation given in equation 3.3.1.

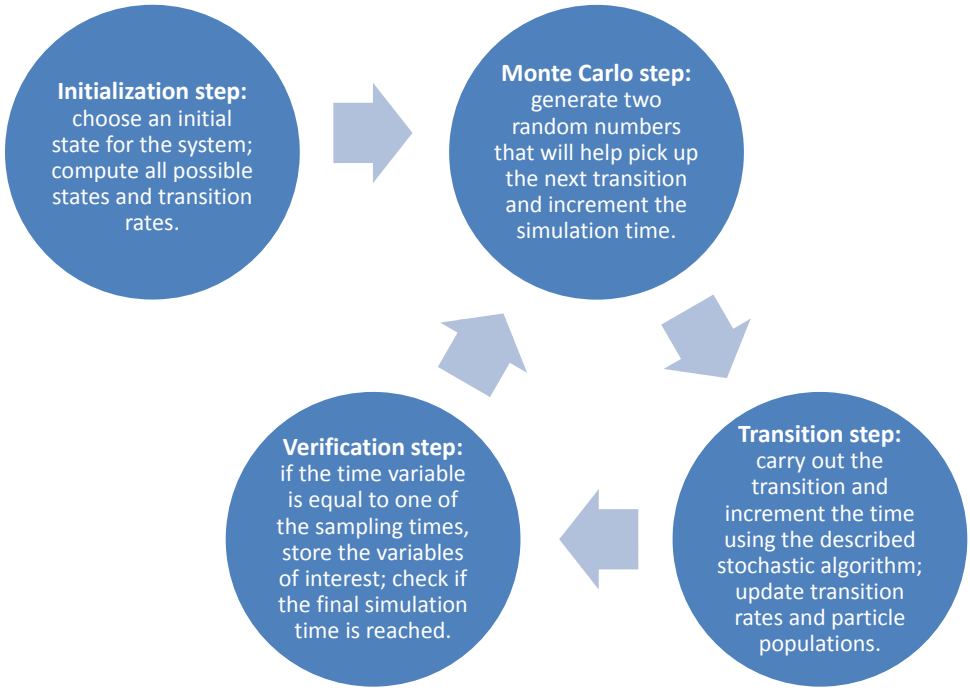

Figure 3.3: Schematic of a possible implementation of the kMC algorithm.

3.3.4 Implementation of a kinetic Monte Carlo Algorithm

As mentioned above, the workaround of actually solving equation 3.3.1 is to use the equivalent, but more practical reaction probability density function, as deduced in equation 3.3.6 and equation 3.3.13. An algorithm that will model this stochastic process is presented below and a work-flow diagram is depicted in Figure 3.3:

Initialization step: The time t is set to 0; all initial states of the system are calculated for all X_i numbers of particles of S_i species if this is the case. The transition parameters $h_1c_1,,h_Nc_N$ for all possible transitions are also computed. Some sampling times are also defined, at which to store the X_i variables, in order to keep track of the stochastic process: a final simulation time is also defined.

Monte Carlo step: Using two randomly picked numbers, generate the (τ, μ) pair with the reaction probability density given by equation 3.3.13.

Transition step: Increment the time variable t with the δt value calculated in the previous step. Carry out the μ transition and update the X_t number of particles

involved in the transition; recalculate the transition parameters $h_t c_t$ for those particles.

Verification step: If the time variable is equal to one of the sampling times, store the variables of interest. If the final simulation time is not yet reached return to the Monte Carlo step.

Some concluding remarks on the above presented Monte Carlo algorithm. This procedure basically simulates a random walk of the multiparticle system according to equation 3.3.6. We have shown that equation 3.3.6 gives an equivalent but more elegant approach to the stochastic master equation given in equation 3.3.5. By performing several Monte Carlo runs, one can calculate the mean properties of a system - like the mean leakage current - but can also get an idea on the fluctuations that should be expected. Another point to be noted is that a stochastic approach will deliver meaningful results even if we have a system in non-equilibrium, with multiple competing transitions that will all affect the particle populations; in such a case, a deterministic approach will most certainly fail to predict a correct time evolution of the system. Finally, a note on the simulation procedure: since the main goal of the described method will be to model leakage currents through high-k dielectrics and since the charge carriers that build up this current are not neutral, electrostatic interactions are to be expected in our system. For this purpose a Poisson solver is coupled to our kMC algorithm and ensures that all electric interactions are properly taken into account when the transition parameters are recalculated in every loop. More details on this aspect will be given in the sections below.

3.4 The Drift-Diffusion Model

A different approach to simulate the leakage behavior of high-k dielectrics is to make use of a commercially available, state-of-the-art 3-D finite volume physical simulator, the Sentaurus Device simulator [112]. The obvious advantages of such an approach are the improved speed, robustness, post-processing capabilities and ease of use: we will give futher details and discuss these points in the chapter dedicated to TCAD modeling.

As for most basic electrical simulations, Sentaurus Device will by default calculate the transport through our leaky oxide which is viewed in the following as a

semiconductor with a very low mobility in the framework of the drift-diffusion model. It will first solve the electron and hole continuity equations, coupled with the Poisson equation, to model also the electrostatic interactions between charged particles:

$$\begin{aligned} \nabla \cdot [\epsilon \nabla V] &= q(n - p - N_D^+ + N_A^- + \rho_T) \\ \frac{\partial n}{\partial t} &= \frac{1}{q}\nabla J_n + G_n - R_n \\ \frac{\partial p}{\partial t} &= -\frac{1}{q}\nabla J_p + G_n - R_n \end{aligned} \tag{3.4.1}$$

where ϵ is the dielectric permittivity, N_D^+ and N_A^- are the densities of ionized donors and acceptors, respectively, q is the unit charge, n and p are the electron and hole densities, respectively, and ρ_T is the trap density.

As mentioned earlier, the drift diffusion model is used as the standard one; thus the electron and hole current densities have the expression:

$$\begin{aligned} J_n &= \mu_n(n\nabla E_C - 1.5nk_BT\nabla \ln m_n) + D_n(\nabla n - n\nabla \ln \gamma_n) \\ J_p &= \mu_p(p\nabla E_V + 1.5nk_BT\nabla \ln m_p) - D_p(\nabla p - p\nabla \ln \gamma_p). \end{aligned} \tag{3.4.2}$$

Here m_n and m_p are the charge carrier effective masses, $D_n = k_BT\mu_n$ and $D_p = k_BT\mu_p$ the diffusivities and γ can be computed, assuming Fermi-Dirac statistics, as:

$$\begin{aligned} \gamma_n &= \frac{n}{N_C}\exp\left(\frac{E_{F,n} - E_C}{k_BT}\right) \\ \gamma_p &= \frac{p}{N_V}\exp\left(\frac{E_{F,p} - E_V}{k_BT}\right) \end{aligned} \tag{3.4.3}$$

The simple drift-diffusion transport model presented in this chapter needs to be extended, since it was demonstrated that trap states inside the STO film have a severe impact on the transport mechanism [73]. We therefore will include in our model also trap states inside the higher-k dielectric. These trap states and the transitions of the charge carriers from and to such a trap state are modeled using a so called multistate configuration (MSC) framework, for reasons that will later become obvious.

4 TCAD Modeling

This chapter will focus on the implementation of the possible leakage mechanisms, described in Chapter 3, in a state-of-the-art 3-D finite volume physical simulator, part of the Synopsys TCAD Framework [112]. Such an implementation offers unprecedented flexibility, post processing or visualization capabilities coupled with fast simulation times. If a kinetic Monte Carlo simulation needs about 1 week for an acceptable statistic (averaging the current over about 10.000 randomly distributed defects in about 1000 parallel runs), a TCAD simulation will only need about 2 hours. Also arbitrary 3D geometries can be modeled, the advanced meshing algorithm offering high numerical robustness; thus the simulation of realistic device geometries becomes possible. Of course there are some limitations when using this approach and all these points will be addressed in the following chapter.

Since, as already mentioned, it was demonstrated that trap states inside the STO film have a severe impact on the transport mechanism [73], we will start extending the simple drift-diffusion transport model presented in Chapter 3.

4.1 Multistate Configuration Framework

The multistate configuration is characterized by an arbitrary number of states $i = 1,\ldots,N$ with the state occupation probabilities $s_1,\ldots,s_N$ that fulfill the condition:

$$\sum_{i=1}^{N} s_i = 1 \tag{4.1.1}$$

This equation simply states that the probability of finding a random particle in one of possible states of our system must be equal to unity. The dynamics

between two states i and j can be described by an arbitrary number of transitions (in our case trap capture and emission processes):

$$s_i = \sum_{j \neq i} \sum_{t \in T_{ij}} c_{ij} s_j - e_{ij} s_i \tag{4.1.2}$$

where T_{ij} represents the set of all allowed transitions t between state i and j. For such a transition, we can state that the capture rate c is $c = c_{ij} = e_{ji}$ and the emission rate e is $e = e_{ij} = c_{ji}$, where i is the initial and j is the final state.

Each state can have a number K of positive or negative charges associated, but transitions between states must obey the charge conservation laws. The particles needed to fulfill the conservation laws can be taken from reservoirs – metal electrodes. That is, reservoir particles also have an associated charge K_r and can be involved in any transition with an arbitrary number P_r. The charge conservation law reads:

$$K_i - K_j = \sum_{r=1}^{M} P_r K_r \tag{4.1.3}$$

with the same convention for the interacting states.

The states involved in the transitions are all characterized by a base energy E_i, the arbitrary number of charges K_i and the specific energy E_i^- of an electron in that state. The total energy of a state can then be written as:

$$H_i = E_i + K_i E_i^-. \tag{4.1.4}$$

Knowing the total energy of a state, the position of the Fermi levels in the metal electrodes, the charge of the state and the temperature of the system, one can calculate the occupation probability of the state as:

$$Z_i = g_i \exp(-\beta(H_i - K_i E_F)). \tag{4.1.5}$$

Here β is the thermodynamic beta. Summing for all states, one can get the total occupation probability:

$$Z = \sum_{i=1}^{N} Z_i \tag{4.1.6}$$

and thus the equilibrium occupation probability for state i can be defined:

$$s_i^* = Z_i / Z. \tag{4.1.7}$$

We assume for the MSC framework that the intrinsic density n_i can be approximated by:

$$n_i = \sqrt{N_C N_V \exp(-\beta E_g)}. \tag{4.1.8}$$

And furthermore, the intrinsic Fermi level is situated as follows:

$$E_i = \frac{1}{2}\left[(E_C + E_V + k_B T \ln(\frac{N_V}{N_C}))\right]. \tag{4.1.9}$$

We then obtain for the quasi Fermi levels and for the equilibrium Fermi level the energies:

$$\begin{aligned} E_{F,n} &= E_i + k_B T \ln\left(\frac{n}{n_i}\right) \\ E_{F,p} &= E_i - k_B T \ln\left(\frac{p}{n_i}\right) \\ E_F &= \frac{1}{2}(E_{F,n} + E_{F,p}). \end{aligned} \tag{4.1.10}$$

The two quantities, the equilibrium Fermi level of a state and the equilibrium occupation probability of that state, are the most important variables for our multistate configuration system and will be used to calculate the transitions between states.

Keeping the same naming convention for the initial state i and final state j, one can write the detailed balance condition for any transition as:

$$\frac{e}{c} = s_j^* s_i^*. \tag{4.1.11}$$

We will now deduce the capture and emission rates, or in other words the transition rates, between the states of the MSC system for the case of a defect state. Let us treat the case of electrons in the following; the same rationale holds also for the case of holes if one simply changes the signs of the charges and of the inequalities. If the number of electrons is larger in the initial state than in the final state $K_i > Kj$, then the capture rate depends on the electron density n, with:

$$c = \sigma v_{th} n \tag{4.1.12}$$

where σ is the trap cross section and v_{th} is the charge carrier thermal velocity; an analogue capture rate can be deduces for holes also. We will also observe that for an any capture process:

$$N_n - N_p = K_i - K_j \tag{4.1.13}$$

with N_n and N_p being the number of electrons and holes that interact in the transition. For the emission rate, due to the detailed balance requirement 4.1.11, we will obtain:

$$\begin{aligned} \frac{e}{c} = \exp(&-N_n \beta_n (E_{F,n} - \bar{E}_C) + N_p \beta_p (E_{F,p} - \bar{E}_V) + \\ &+ \beta_i (-N_n \bar{E}_C + N_p \bar{E}_V - H_{ij})) \end{aligned} \tag{4.1.14}$$

where $H_{ji} = H_j - H_i$. The average conduction and valence band energies are :

$$\begin{aligned} \bar{E}_C &= E_C + \frac{3}{2} k_B T_n \\ \bar{E}_V &= E_V - \frac{3}{2} k_B T_p \end{aligned} \tag{4.1.15}$$

It can be shown that in this case, in thermal equilibrium, the detailed balance condition is fulfilled.

In order to make our model as accurate as possible, another effect has been included in the characterization of the states, similar to the kMC simulation: the

relaxation process of a charged state when a carrier is captured. Its importance has been well documented in e.g. [40, 88]. Recent experimental proof of oxygen vacancy related relaxations in STO films [113, 114] also motivates us to include this effect. It can be easily done by defining appropriate state energies for the multistate system, which is one of the main reasons we opted for the implementation of the MSC framework; a charged oxygen vacancy level situated at 0.9 eV under the conduction band [86] with a relaxation energy of 0.1 eV has thus been assumed [115].

4.2 Nonlocal Tunneling

Since the injection from the electrodes – that act as particle reservoirs – and the transport through the STO film is most likely dominated by tunneling between different trap states, further extensions are needed for the physical modeling of the leakage mechanism. A non-local tunneling model is implemented over the whole device. For this purpose a nonlocal mesh is first build, where the non-local lines of the mesh represent all possible tunneling paths.

The direct tunneling contribution through the thin layer is calculated by the WKB approximation that uses the local wave numbers and interface coefficients [116]. Thus the tunneling probability for a particle with energy ϵ and initial position l to a point $u > l$ can be formulated, for an electron, as:

$$\Gamma_{C,\nu}(u,l,\epsilon) = T_{CC,\nu}(l,\epsilon)\exp\left(-2\int_l^u \kappa_{C,\nu}(r,\epsilon)dr\right)T_{CC,\nu}(u,\epsilon) \tag{4.2.1}$$

where $T_{CC,\nu}$ is the interface transmission coefficient and κ the local wave number of the particle at position r. The imaginary wave number of the electron with that specific energy and position can be computed from:

$$\kappa_{C,\nu}(r,\epsilon) = \sqrt{2m_C(r)\,|E_{C,\nu}(r)-\epsilon|}\Theta[E_{C,\nu}(r)-\epsilon]/\hbar. \tag{4.2.2}$$

The parameter m_C denotes the conduction-band tunneling mass and Θ is the Heaviside function.

For the interface transmission coefficient in equation 4.2.1, a model similar to [117] is used to evaluate it:

$$T_{CC,\nu}(x,\epsilon) = \frac{v_{-,\nu}(x,\epsilon)\sqrt{v_{-,\nu}(x,\epsilon)^2 + 16v_{+,\nu}(x,\epsilon)^2)}}{v_{+,\nu}(x,\epsilon)^2 + v_{-,\nu}(x,\epsilon)^2}. \tag{4.2.3}$$

We have used v_- to specify the velocity of the electron on the side of the junction or barrier where it is not confined – in the general case it can be either inside an electrode or in the conduction band of a semiconductor. The v_+ term denotes the velocity of the electron inside the forbidden zone – the bandgap of out high-k dielectric; in this case the velocity can have an imaginary part. Obviously, for two points of the discretized nonlocal mesh that are both located inside the dielectric, the interface transmission coefficient is equal to one. The electron velocities, in the confined and free regions are calculated as:

$$v_\nu = \left|\partial\epsilon/\partial\hbar\kappa_{C,\nu}\right|. \tag{4.2.4}$$

Thus, the contribution to the generation-recombination rates at position u due to an electron tunneling process from position l is:

$$\begin{gathered} R_{C,\nu}(u,l,\epsilon) - G_{C,\nu}(u,l,\epsilon) = \\ \frac{A_C}{qk_B}\vartheta\left[\epsilon - E_{C,\nu}(u), -\frac{dE_{C,\nu}}{du}\right]\vartheta\left[\epsilon - E_{C,\nu}(l), -\frac{dE_{C,\nu}}{dl}\right]\Gamma_{C,\nu}(u,l,\epsilon) \\ \left[T_n(u)\ln\left(1+\exp\left[\frac{E_{F,n}(u)-\epsilon}{k_BT_n(u)}\right]\right) - T_n(l)\ln\left(1+\exp\left[\frac{E_{F,n}(l)-\epsilon}{k_BT_n(l)}\right]\right)\right] \end{gathered} \tag{4.2.5}$$

with $\vartheta(x,y) = \delta(x)\left|y\right|\Theta(y)$, $A_C = g_C A_0$ the effective Richardson constant, g_C the degeneracy factor, $\Gamma_{C,\nu}$ the tunneling probability calculated in equation 4.2.1.

Integrating over the position and energy one finally gets the expression of the tunneling current density:

$$j_{CC}(l) = -q\sum_\nu \int_l^\infty \int_{-\infty}^\infty \left[R_{C,\nu}(u,l,\epsilon) - G_{C,\nu}(u,l,\epsilon)\right] d\epsilon du. \tag{4.2.6}$$

The non-local mesh also couples the particle reservoirs to the trap states ensuring that not only injection and extraction of carriers in and out of traps, from the electrodes, but also trap assisted tunneling is possible.

Both electrode-trap tunneling and trap-trap tunneling can be an elastic or inelastic process. The phonon-assisted capture rate from an electron tunneling from an electrode into a trap can be modeled as [118, 119]:

$$\begin{aligned} c^n_{C,inelastic} = & \frac{\sqrt{m_t m_0^3 k^3 T_n^3} g_c}{\hbar^3 \sqrt{\chi}} V_T S \omega \left[\frac{\alpha (S-l)^2}{S} + 1 - \alpha \right] \cdot \\ & \cdot \exp \left[-S(2f_B + 1) + \frac{\Delta E}{2 k_B T} + \chi \right] \left(\frac{z}{l+\chi} \right)^l \cdot \\ & \cdot F_{1/2} \left(\frac{E_{F,n} - E_C(0)}{k_B T_n} \right) \frac{|\Psi(z_0)|^2}{\Psi(0)}^2 \end{aligned} \tag{4.2.7}$$

where V_T is the trap interaction volume, S is the Huang-Rhys factor and $\hbar\omega$ the energy of the phonons involved in the transition. The Bose-Einstein occupation of the phonon state is computed as, $f_B = [\exp(\hbar\omega / k_B T) - 1]^{-1}$ while $z = 2S\sqrt{f_B(f_B+1)}$ and $\chi = \sqrt{(l^2 + z^2)}$.

The number of emitted phonons is l while the dissipated energy is $\Delta E = E_C + 3k_B T_n/2 - E_{trap}$.

Furthermore, for the elastic case we have [118]:

$$\begin{aligned} c^n_{C,elastic} = & \frac{\sqrt{8 m_t} m_0^{3/2} g_C}{\hbar^4 \pi} V_T [E_C(z_0 - E_{trap})]^2 \Theta[E_{trap} - E_C(0)] \cdot \\ & \cdot \sqrt{E_{trap} - E_C(0)} f \left(\frac{E_{F,n} - E_{trap}}{k_B T_n} \right) \frac{|\Psi(z_0)|^2}{\Psi(0)^2}. \end{aligned} \tag{4.2.8}$$

For the calculation of the ratio between the two electron wave function amplitudes, at the injection site and the trapping site, we will again use the tunneling probability previously calculated with the WKB approximation:

$$\frac{|\Psi(z_0)|^2}{\Psi(0)^2} = \frac{v(0)}{v(z_0)} \Gamma_C. \tag{4.2.9}$$

We will use the trap energy for calculating Γ_C in the case of the elastic tunneling process, while for the inelastic case we will approximate the tunneling energy with $E_C + k_B T_n/2$ for the computation of the same parameter. As stated above, emission rates are always computed following a detailed balance principle.

4.3 Geometry Generation

The first step, before defining a command file – a script that controls a simulation in the TCAD framework, we will discuss further on this topic in the next sections – is to model and define the structure of the device we want to analyze.

We will start our modeling task by generating a geometry similar to that of our fabricated SRO/STO/SRO samples. For this purpose we will use the Sentaurus Structure Editor (SENSE) tool from the Sentaurus TCAD framework. This program allows the user to easily edit a structure with the help of a graphical user interface (GUI). Other actions, like defining meshing refinements or analytical doping profiles, can be also performed with the help of the GUI environment. SENSE can be viewed also as an interactive link between the different Sentaurus meshing engines and the physical simulator Sentaurus Device, since it will also generate the needed input files for the meshing programs and will allow the user to configure the meshing strategy.

A typical structure modeling procedure, performed to obtain a MIM structure identical to that in Chapter 3, covers the following steps:

1. Generate the 3 dimensional model.
2. Add and define electrical contacts.
3. Add doping profile – a wide variety of deterministic and stochastic approaches are available in order to define a realistic doping profile.
4. Declare a refinement strategy.
5. Configure one meshing algorithm.

In our case, the high-k dielectric capacitor was defined as composed of three cuboids, with the geometrical dimensions corresponding to the measured ones. The STO layer has a thickness of 10 nm, with lateral extensions of also 10×10 nm,

while the two SRO electrodes were also defined as 3 dimensional contacts, to allow a more accurate treatment of the "metal/dielectric" interface (in the case of ideal 2 dimensional contacts, some restrictions apply to the contact/dielectric interface).

The corresponding materials – STO in the case of the dielectric and SRO in the case of the contact or electrode – were defined in external parameter files, with appropriate material parameters taken form literature.

No doping profile has been defined, since the fabrication and characterization steps for the fabricated samples do not reveal any unintentional doping.

An adaptive meshing algorithm has been chosen for the device discretization. The minimum and maximum discretization lengths for the 3 spatial dimensions are given and the meshing engine will find an optimum number of vertices for the given set of instructions. Since we will be interested in nonlocal (trap assisted) tunneling processes, a very fine mesh is needed. We choose our minimum and maximum element sizes in all 3 directions (a carthesian coordinate system is assumed by default) to be 0.25 and respectively 0.5 nm. We can thus be sure, that the generated mesh will be fine enough to serve also as an non-local mesh for the tunneling events. For such a process, entire lines connecting mesh vertices are needed to model the tunneling paths, rather than individual vertices on the two sides of the tunneling barrier – hence the non-locality of this tunneling model.

The default meshing engine is chosen, with the option to force an axis-aligned mesh and relying on the box method for the meshing algorithm. Some details on this algorithm will follow in the next section.

4.4 Meshing Algorithm

In the following, we will give a concise description of the algorithm used to mesh our modeled geometry. The interested reader is referred to Chapter 40 of the Sentaurus Device User's Guide [112] for more details.

Since a simulator cannot interpret continuous quantities, it needs a mesh to discretize the given geometry and thus calculate the quantities of interest – like current densities, charge or electric field – in each vertex of the mesh. The "box method" will construct a test volume around each vertex of the mesh

and will solve the system of coupled partial differential equations (PDEs) for that point by numerical integration. This method has the advantage that by using finite volume elements and flux conservation as coupling criteria between adjacent elements, it ensures that Gauss law will be fulfilled for all mesh vertices. This characteristic makes the finite-volume approach very appealing for the numerical simulation of semiconductor devices.

The default meshing algorithm will in general approximate the PDE:

$$\nabla \cdot J + R = 0 \tag{4.4.1}$$

with a first order accuracy to:

$$\sum_{j \neq i} \kappa_{ij} \cdot j_{ij} + \mu(\Omega_i) \cdot r_i = 0 \tag{4.4.2}$$

A graphical representation of this algorithm, clarifying also the naming convention for the coefficients of the above equation is given in Figure 4.1.

Depending on the dimensionality of the problem to be solved, the coefficients κ_{ij} and control volumes $\mu(\Omega_i)$ for the method can vary:

Dimension	κ_{ij}	$\mu(\Omega_i)$
1D	$1/\mathrm{l}_{ij}$	Box length
2D	d_{ij}/l_{ij}	Box area
3D	D_{ij}/l_{ij}	Box volume

Table 4.1: Box method coefficients for 1, 2 and 3-D discretization.

Also, the differential equations that need to be solved coupled in each vertex of the mesh – usually the Poisson equation, the electron and hole continuity equation – are discretized using the j_{ij} and r_i variables in the following manner:

where $B(x) = x/(e^x - 1)$ is the Bernoulli function.

Looking at Figure 4.1 and at Table 4.1, we can observe that for the 1D and 2D case the box coefficients are trivial to deduce while for the 3D case, in general, calculating these coefficients becomes a challenging task. One problem

Equation	j_{ij}	r_i
Poisson	$\epsilon(u_i - u_j)$	$-\rho_i$
Electron continuity	$\mu^n(n_i B(u_i - u_j) - n_j B(u_j - u_i))$	$R_i - G_i + \frac{d}{dt} n_i$
Hole continuity	$\mu^p(p_i B(u_i - u_j) - p_j B(u_j - u_i))$	$R_i - G_i + \frac{d}{dt} p_i$

Table 4.2: Numerical approximation of the coupled differential equations, solved in each vertex of the mesh.

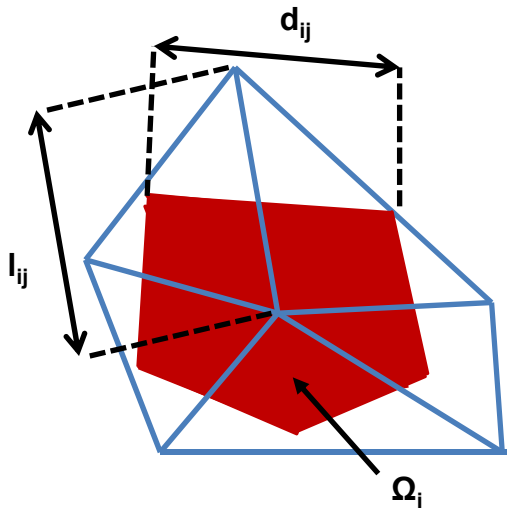

Figure 4.1: A box discretization for a 2-dimensional triangular mesh, exemplifying the choice of the box coefficients $\kappa_{ij} = d_{ij}/l_{ij}$ and control volume Ω_i (redrawn from [120]).

that might occur, for an unwise meshing situation, is that the discretization coefficients become negative.

The standard approach for the 3D problem is to build a special mesh, a so-called Delauny mesh. This mesh has the important property that no other vertices lie inside the circumsphere of a mesh element. For further details on the advantages of using a Delauney mesh for the spatial discretization of a physical problem and other important properties of such a meshing strategy, the interested reader can find more information in [121].

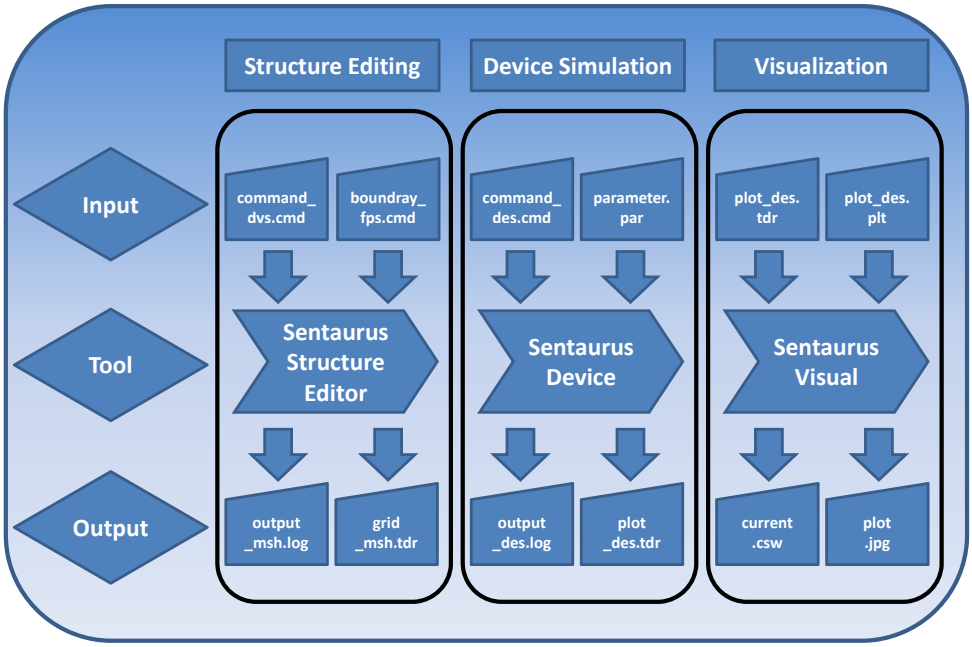

Figure 4.2: Typical TCAD simulation flow including device editing, device simulation and post-processing of the obtained simulation results.

4.5 Device Simulation

Once a structure has been generated, we can proceed to the next step and carry out the actual device simulation. The flow chart in Fig.4.2 gives an overview of the input and output files that are needed or generated during a typical device simulation process and programs that execute them.

As stated above, the grid file is the first prerequisite needed to start a device simulation. This file can be generated by 3 different methods: using the Sentaurus Structure Editor – this approach has been already described in detail, using the Procem advanced process emulation framework, which is also part of the TCAD bundle, and finally using the Sentaurus Process simulator, to model in the most complex and realistic way the fabrication of an electronic device. The latter approach will be extensively discussed in the application section of this chapter.

The grid file is given as input in the command file of Sentaurus Device, together with some other files; in the case of leakage simulations, other important input files were the parameter files for the SRO/STO material system. Detailed elec-

trical parameters have been extracted from literature or from direct electrical measurements and are properly formatted to serve as input files for Sentaurus Device.

Analyzing a command file, for an electrical simulation of the leakage current through the MIM structure, some observations can be made: the command file has 6 distinct sections that control everything from the device physics to the voltage ramps and the quantities to be plotted. Let us describe in brief these sections:

File section

We define and link here all important input files and name also the output files. As mentioned, the parameter files for SRO and STO are given here. Sentaurus device will generate and save then two types of output files, when a simulation is successfully terminated. They are: a .plt file – that records all scalar quantities like currents, voltages or charges at the device terminals – and a .tdr file – stores the distribution of the electric field, charge carrier concentration and other vector fields inside the device.

Electrode section

This section contains all parameters that are needed to characterize the electrodes. In the present case we have 2 electrodes, the two plates of the MIM capacitor, both having SRO declared as material. A good study on the properties of the SRO/STO interface is given in [122], so we model our electrodes accordingly; we assume a barrier of 1 eV as conduction band offset between the electrode and the high-*k* dielectric. The two electrodes are initialized at zero volts to avoid numerical convergence problems.

Physics section

Maybe the most important section, it contains the switches for activating all important physical mechanisms that we want to include in our simulation. The different physical mechanisms can be activated region-wise, material-wise, at interfaces to electrodes or between different materials. In our case, we activate a barrier lowering mechanism at the SRO/STO interface, since [122] predict that a strong reduction of the Schottky barrier at this interface, in the presence of oxygen vacancies, will occur. A thermionic emission process at the injecting

electrode is also switched on, to model the Schottky emission at high temperature. In the global physics section, we turn on also the nonlocal tunneling mechanism throughout the whole STO layer, to enable charge carrier tunneling. The multistate configuration for the defect states inside the dielectric is defined here as well.

Plot section

This section contains information about what quantities to be saved during a simulation run for subsequent visualization and data post-processing. Typical keywords for quantities to be stored include: electric field, electrostatic potential, electron and hole quasi Fermi levels, electron tunneling current, band gap, conduction and valence band, electron density, space charge, current density, etc.

Math section

Options for the used numerical algorithms can be specified here. Relative error, absolute error, number of iterations for the Newton algorithm can be declared here among others. For a short summary of the numerical method used by Sentaurus Device, refer to the next section. Also in the math section, two nonlocal meshes are defined each one stretching from one of the contacts over the rest of the device; in this manner, we can make sure that the injection of charge carriers in the defect state is possible, as well as the extraction of these carriers, coupling also all defect states in the dielectric to the tunneling process.

Solve section

We can define here what simulation our program should actually perform. A wide variety of simulations can be performed with the Sentaurus Device simulator like: quasistationary and transient parameter ramping, small signal (AC) analysis, harmonic balance analysis, coupled optical simulations, coupled thermal simulations, etc. For our purpose, we perform quasistationary voltage ramps on one of the electrodes, gradually increasing the voltage until 2 V to duplicate the measured leakage characteristics of our devices.

4.6 Simulation Algorithm

To complete this section presenting the physics used for the electrical simulations within the TCAD framework, we will finally discuss also the numerical algorithm employed for obtaining the I-V-T curves for the MIM capacitors.

Sentaurus device uses a variation of the Newton algorithm, presented by Bank *et al.* [123], to find a solution for the nonlinear system of partially differential equation – the Poisson equation and the electron and hole continuity equation. For increased accuracy, improved convergence and less memory usage, it is worthwhile to rewrite these 3 equations as:

$$\begin{aligned} g_1(u,v,w) &= -\Delta u + e^{u-v} - e^{w-u} - k_1 = 0 \\ g_2(u,v,w) &= \nabla \mu_n e^{u-v} \nabla v + k_2 = 0 \\ g_1(u,v,w) &= -\nabla \mu_p e^{w-u} \nabla w + k_2 = 0 \end{aligned} \tag{4.6.1}$$

Where u is the electrostatic potential, v and w are the quasi Fermi levels. An argumentation on the choice of these variables can be found again in [123].

In order to determine the solution of a coupled PDE, denoted by g, the Newton algorithm will follow the scheme:

$$g + g'\mathbf{x} = 0 \tag{4.6.2}$$

$$z^j - z^{j+1} = \lambda \mathbf{x}. \tag{4.6.3}$$

The two upper equations can be shortly explained in a few sentences looking also at Figure 4.3. Usually the problem consists in finding the root $g(z_0) = 0$ of a given function or system of PDEs, at a certain bias voltage. An initial guess z^j is needed for the first iteration of the algorithm – special techniques for finding an initial guess near enough to the actual root have also been developed. The derivative of $g'(z)$ is then computed in the point z^j and the intercept of this tangent line with the x-axis can be determined. This intercept z^{j+1} is taken as a better approximation for the root of our function $g(z)$ and the whole algorithm is repeated until a break criterion is met. The voltage can then be incremented until e.g. a voltage ramp is fully swept.

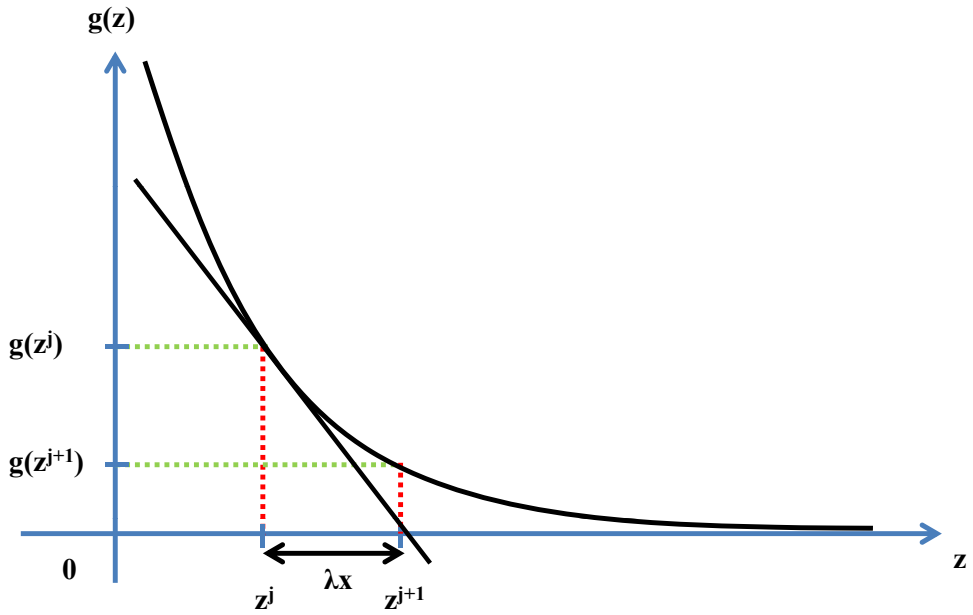

Figure 4.3: Graphical exemplification of the Newton algorithm: starting from the initial guess z^j and computing the derivative of the function in this point, a better approximation z^{j+1} can be found for the root of our function $g(z)$ (redrawn from [120]).

In our case, for $g(z)$ having the form given in equation 4.6.1, the derivative of the coupled system with respect to the 3 variables u, v and w can be written in the form of a Jacobi matrix:

$$g' = \begin{bmatrix} -\Delta * + (e^{u-v} + e^{w-u}) * & -e^{u-v} * & -e^{w-u} * \\ \nabla(\mu_n * e^{u-v} \nabla v) & -\nabla(\mu_n * e^{u} \nabla(-e^{-v} *)) & 0 \\ \nabla(\mu_p * e^{w-u} \nabla w) & 0 & -\nabla(\mu_p * e^{-u} \nabla(e^{w} *)) \end{bmatrix} \tag{4.6.4}$$

There are several break criteria that will stop the Newton iterations: either the norm of the right-hand side in equation 4.6.2 is sufficiently small or the error between to iterations is negligible. The error of the variables to be calculated can be expressed as a relative error:

$$\frac{1}{\epsilon_R} \left\| \frac{\lambda x}{z^j + z_r ef} \right\| < 1. \tag{4.6.5}$$

An absolute formulation of the error can be also used:

$$\left\| \frac{\lambda \bar{\mathbf{x}}}{\epsilon_R \bar{z}^j + \epsilon_A} \right\| < 1 \tag{4.6.6}$$

with $\bar{z}^j = z^j / z^*$, $\bar{\mathbf{x}} = \mathbf{x}/z^*$ and the relation between absolute and relative error:

$$\epsilon_A = \epsilon_R \frac{z_{ref}}{z^*}. \tag{4.6.7}$$

The default convergence criteria is a relative error smaller than 10^{-5} and was also used throughout the presented simulations.

Beside the mentioned Bank-Rose modification of the Newton algorithm, another method for numerically solving electrical problems (but also optical a.o.) can be selected within the Sentaurus Device simulator: the Gummel iterations. For this option, the single PDEs that build our coupled system are individually and consecutively solved. A series of "plugin" loops follows, until again a certain break criterion is met.

4.7 Model Validation

The calibration of the leakage mechanism is performed on a MIM structure that is very similar to the fabricated samples described in the previous chapter; a picture of the modeled capacitor together with the mesh used for the electrical simulations are shown in Figure 4.4. The band diagram of the modeled MIM structure is depicted in Figure 4.5 and some important simulation parameters are presented in Table 4.3. All important physical processes that can play a role in the leakage mechanism of the analyzed structure, and that have been treated in Chapter 3, are also implemented in the TCAD simulation and shown in Figure 4.5.

In short, we can have the following cases:

- Electrons can tunnel from an injecting electrode to some trap states located in the vicinity of the electrode. The now occupied trap state in the dielectric will follow a relaxation process as mentioned earlier, and will have a lower energy inside the STO bandgap.

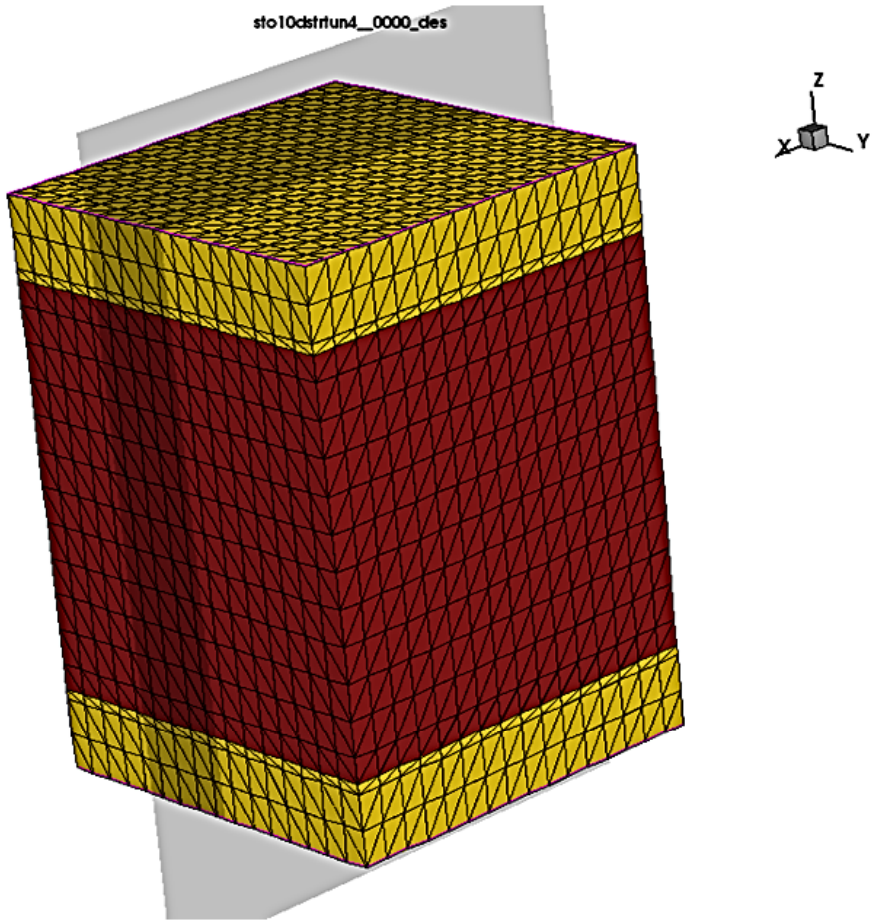

Figure 4.4: Modeled SRO/STO/SRO capacitor (not at scale), with the same thickness of 10 nm as the measured samples, used to calibrate the tunneling mechanisms in the Sentaurus Device simulator.

- Electron emission over the SRO/STO barrier, directly in the STO conduction band is also allowed and can have an impact at higher temperatures. The charge carriers that have tunneled from the electrode into traps can reach the collecting electrode following a trap assisted tunneling process in the STO layer.
- Finally, a Poole-Frenkel emission of the electrons, from trap states in the dielectric film, into the conduction band is also included in the model.

Some measured curves are chosen over an interval of 100 °C and simulations are performed in order to validate the model presented above.

The obtained results together with a short sensitivity analysis are shown in Figure 4.6. As can be observed, a reasonable fit can be achieved with the parameters

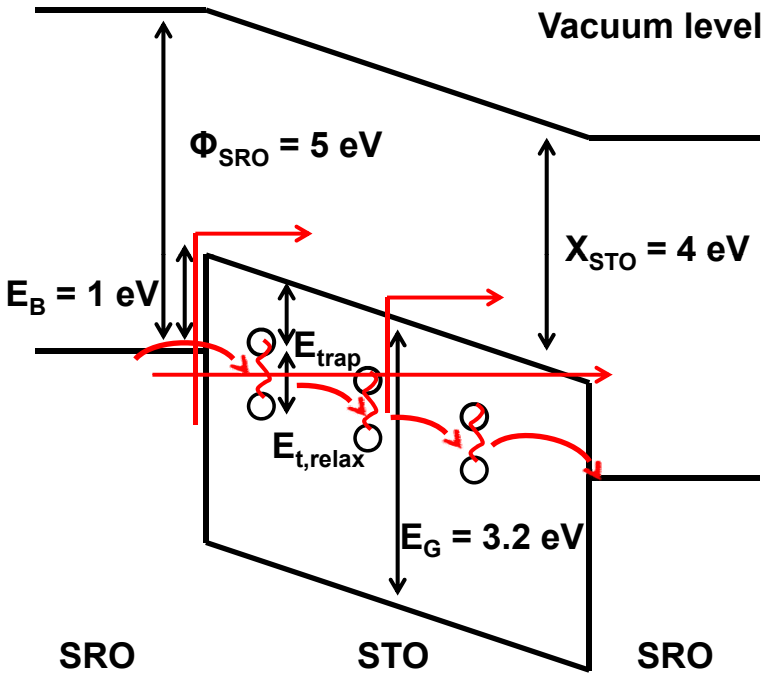

Figure 4.5: Band diagram of the modeled structure, containing some important simulation parameters. Also shown, the possible conduction processes that are included in the model: direct tunneling, Schottky emission over the SRO/STO barrier, elastic/inelastic injection of carriers into trap states and inelastic trap assisted tunneling (taken from [69]).

given in Table 4.3, in good agreement also with our kMC simulations. Together with the best fit results, Figure 4.6 shows, for three different temperatures, the impact of the conduction band offset between the electrode and the dielectric film as well as the effect of the trap state concentration inside the dielectric film.

Over the whole temperature interval the same trend can be observed, namely a sharp decrease in the leakage current when the trap states concentration is decreased by two orders of magnitude. This effect is not really surprising, since we assumed from the beginning that trap assisted tunneling should be the dominant leakage mechanism for our material system, with only moderate impact of the other transport mechanisms included in the model, like Poole-Frenkel emission. Nevertheless, the fact that we can prove our assumptions with the help of our complex physical model is a first and important step towards optimization of the

Parameter	STO	SRO
Bandgap E_g	3.2 eV	-
Electron affinity	4	$\Phi_{SRO} = 5\ eV$
Trap concentration N_T	$2 \cdot 10^{19}\ cm^{-3}$	-
Trap depth E_T	0.8 eV	-
Relaxation energy E_R	0.1 eV	-
Tunneling mass m_t	0.4 m_0	-

Table 4.3: Some selected simulation parameters [84–86, 115, 122].

SRO/STO/SRO structure. We strongly believe that a procedure similar to that reported by Pawlak *et al.* [73] for their material system could also help reduce the trap states concentration for our MIM structure and thus reduce the leakage currents to acceptable values.

The other effect that can be observed for all temperatures in the same figure is the reduction of the simulated leakage current once the conduction band offset between the electrode and the dielectric film is increased. This result also agrees with our understanding of the leakage process through the STO film. An increased barrier at the injecting electrode will decrease the tunneling probability of the electrons from the reservoir into the trap states located near the electrode and will thus limit the current again into an acceptable interval. The simulated increase of the electrode/dielectric barrier in this example was of 0.2 eV and could be achieved experimentally by introducing some interface dipole effect at the injecting electrode.

Having calibrated the leakage model for the planar MIM structure, we can now use in the following sections the same model for the feasibility study of a 3D high-*k* dielectric DRAM cell.

4.8 Process Simulation of a DRAM Cell

In the following section the 3D process simulation of a realistic 1T1C DRAM cell is presented. It is based on a Synopsys technology template, modified in accordance with the MIM structure proposed and demonstrated in [56] – a deep trench SRO/STO/SRO capacitor with a depth of 1 μm, a diameter of 100 nm

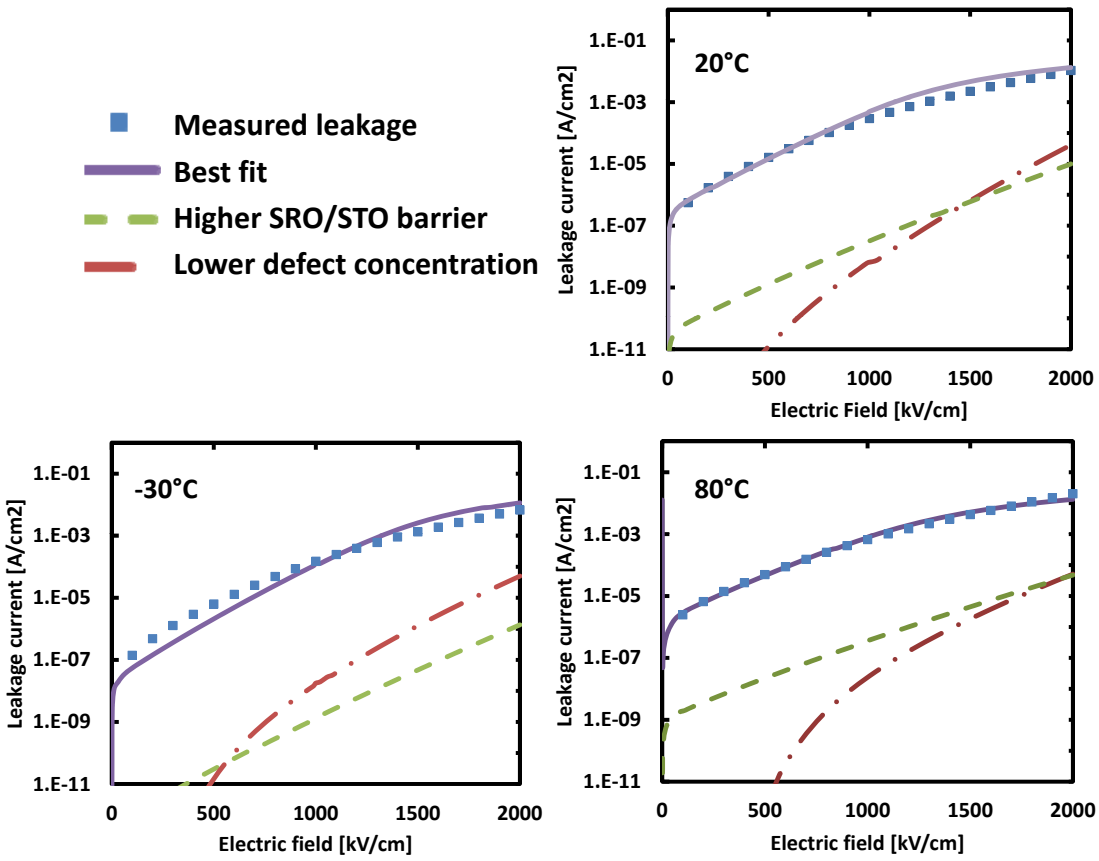

Figure 4.6: Simulated I-V characteristics for the samples, at different temperatures; also shown, beside the best fit, simulations with decreased defect states concentration and with increased injection barrier (taken from [69]).

and a thickness of the dielectric coating of 10 nm. A planar NMOS device is used as the pass transistor of the memory cell. Finally, a characterization of the modeled DRAM cell is performed, including the transfer characteristic of the pass transistor and the cell capacitance is extracted. Analyzing the subthreshold swing and the obtained capacitance, conclusions about the performance of such a high-*k* DRAM cell can be drawn.

4.8.1 Overview

To generate the 1T1C memory cell architecture, a layout driven approach is chosen, using the Sentaurus Process simulator. SProcess is a multidimensional, flexible process simulation environment, integrated in the Synopsys TCAD package. Process steps like deposition, implantation, diffusion, oxidation, etching,

silicidation, etc. have been carefully calibrated with measured typical fabrication steps, offering unique predictive capabilities.

Furthermore, using the ICWBEV Plus Workbench, the masks needed for the process simulation can be read from an external layout file, making thus subsequent modifications to the structure an easy task; the dimensions for the layout masks chosen in this work are taken from [56]. The layout used in the following sections is depicted in Figure 4.8: one can observe that 9 masks are used for this DRAM cell, however four of them are needed only to deposit the metallizations for the device contacts. Simulating the whole fabrication process rather than simply creating a structure with the device editor brings also some other advantages. The geometry can contain an arbitrary number of rounded shapes, which usually are formed during non-isotropic etching steps of the silicon oxide or nitride spacers, and are difficult to reproduce in a structure editor without prior knowledge of the non-isotropic etching rates. Complex analytical doping profiles can also be included in the process and – a point that is important for industrial applications – the thermal budget of the whole process flow can be accurately estimated. Thus a simulation tool flow which starts with a layout file, models the fabrications process, extracts the electrical properties with a device simulator and allows for complex visualization and post-processing capabilities of the calculated quantities could enable virtual prototyping and help shorten the cycles of a learn curve considerably.

The process simulation for our memory cell can be divided in 6 steps, which will be further discussed, and a final meshing step where a more refined mesh, appropriate for accurate electrical simulations, is generated. We will now shortly present the processing steps that are needed for the fabrication of a realistic DRAM cell.

4.8.2 Initialization

The simulation domain is defined here: in our case, a silicon substrate with a length of 0.4 μm, a width of 0.2 μm and a thickness of 5 μm. The orientation of the silicon crystal is 100 – the orientation is important for stress calculation, if it is believed that stress will influence the device performance. A uniform Boron doping with the value 10^{16} cm^{-3} is assumed for the silicon wafer. Some discretization parameters and global numerical quantities are also defined in

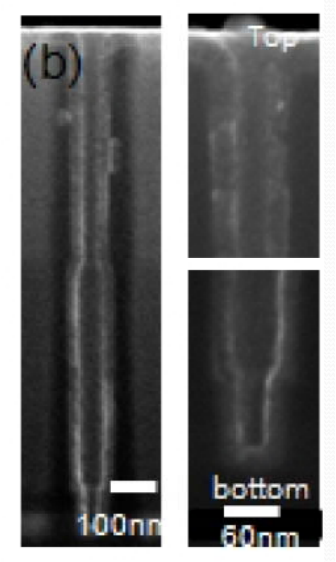

Figure 4.7: A SEM micrograph showing the high conformality of the STO coating inside the etched deep trench capacitor structure (taken from [56]).

this section. Without going into detail, we briefly mention that the process simulator uses either the finite volume or finite elements approach to perform the multidimensional integration and the modified Newton algorithm to solve the nonlinear equations e.g. for the diffusion of dopants.

An oxide buffer (pad) layer is first grown on the substrate followed by a protective nitride deposition. These two layers will help patterning the isolation trench for the memory cell.

4.8.3 Shallow Trench Isolation (STI)

As the isolation pitch between adjacent CMOS devices shrinks together with all other device dimensions according to Moore's law, the leakage and unwanted crosstalk between devices can turn into a severe problem. The standard approach of using a local silicon oxidation (LOCOS) has proven successful for past CMOS generations, but starting with the 250 nm generation, a new technique was needed to reduce again the unacceptable high leakage and crosstalk. For the STI step, a photoresist is deposited on the nitride layer. The photoresist is then patterned using the appropriate layout mask. An etching step follows, as can be observed in Figure 4.9. The nitride and oxide layers are striped and the trench can be etched in the silicon wafer. Silicon oxide is thermally grown to fill the

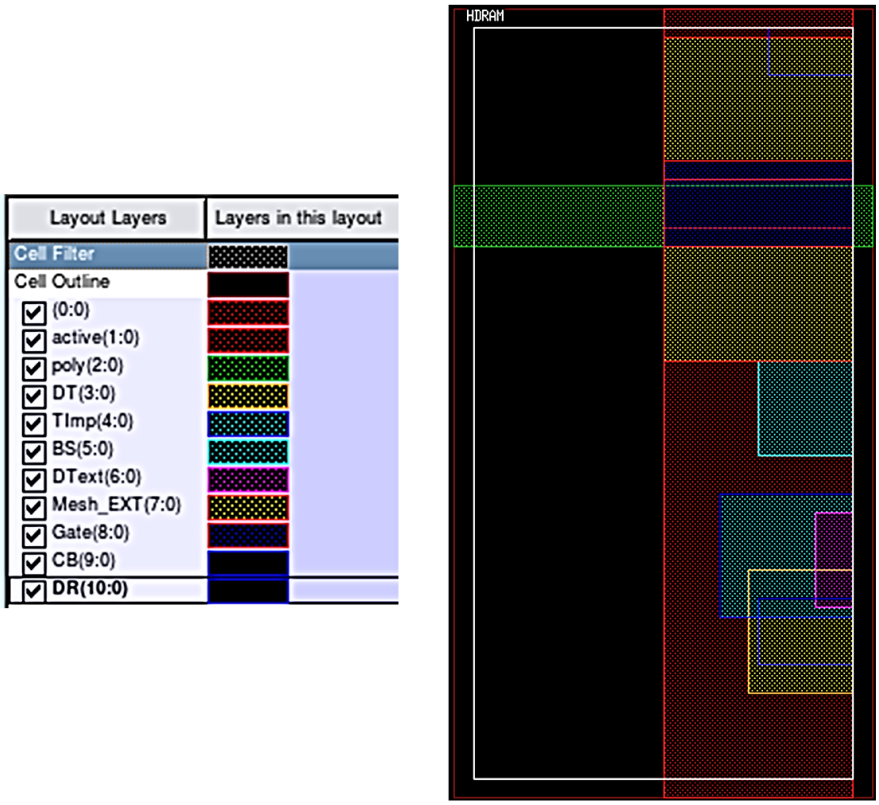

Figure 4.8: The process simulation for our DRAM cell will be, as mentioned above, a realistic, layout driven one; therefore 9 different masks are defined in the ICBEW Workbench and subsequently used in the process.

trench. The buffer oxide is crucial in this step, without it the stress generated by the growing silicon oxide that fills the trench on the silicon – nitride interface, in the immediate vicinity of the trench, would lead to cracks. Once the trench is filled, the patterned nitride can be removed and the oxide height is adjusted to the desired value – this could later be the thickness of the gate oxide for the pass transistor, if no deep trench formation would follow. A so-called quantum zone is defined, as shown in Figure 4.9, where later the quantum corrections for the electrical simulation will be applied. This zone stretches under the oxide, having a length of 32 nm and a thickness of about 10 nm – it is placed where the future pass transistor channel will be formed.

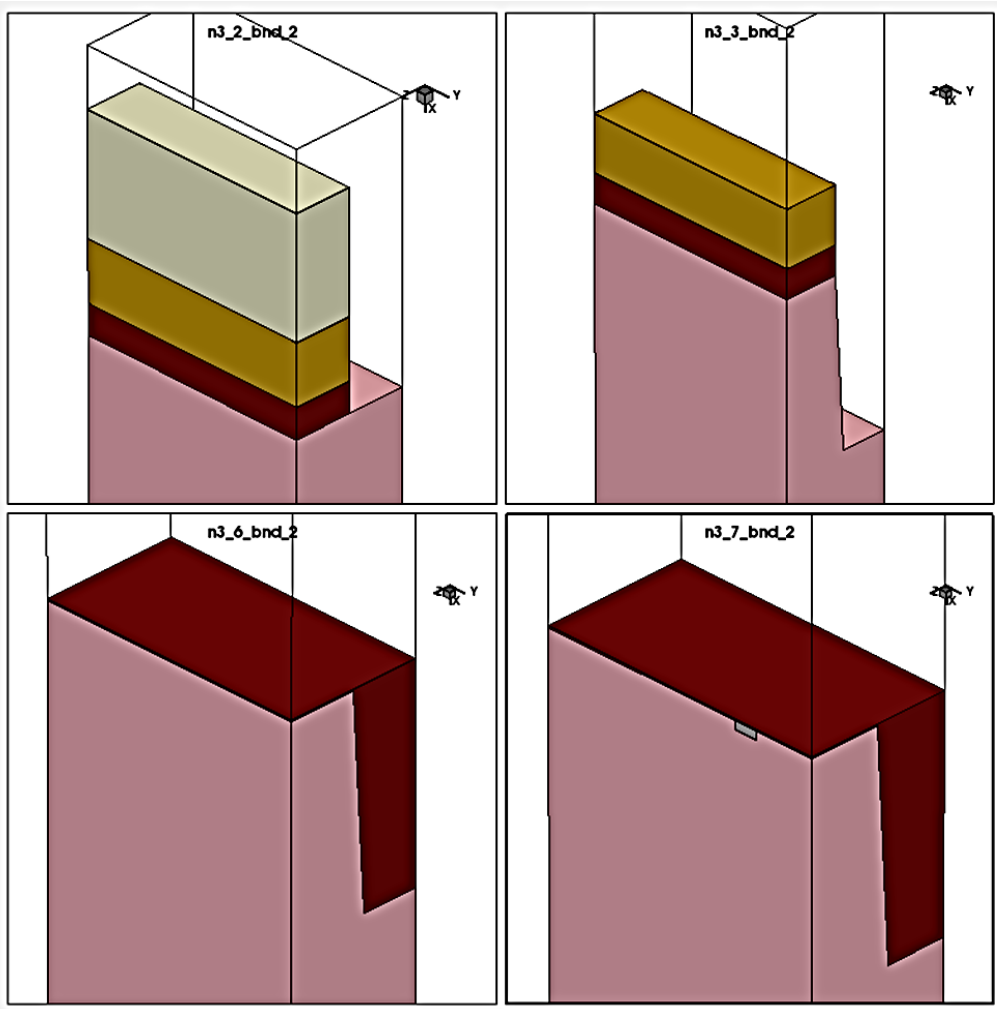

Figure 4.9: The STI process step, including oxide, nitride and photoresist deposition, etching and reoxidation. Also a "quantum-zone" is defined, where the future transistor channel will form.

4.8.4 Deep Trench Formation

The remaining oxide after the trench filling process is removed, to gain access to the silicon wafer. Again, a interlevel dielectric (ILD) is deposited with a positive photoresist on top. Using the layout mask previously defined, the ILD is patterned. Figure 4.10 shows that this etching process is anisotropic, so only a detailed knowledge of the anisotropic etching rates and a careful choice of the deposited dielectric thickness and etching time can ensure an opening with a diameter of 100 nm in the nitride mask. We choose this diameter for the future deep trench capacitor since it is very close to the structure reported in [56] and seems a realistic choice. An isotropic silicon etching step follows and we choose

the etching time accordingly to pattern a 1 μm deep trench. The first electrode, in this case the conductive oxide SRO is uniformly deposited with a thickness of 10 nm, followed by the deposition of the high-k dielectric STO layer of again 10 nm. The trench is finally filled with SRO, which will form the second electrode of the deep trench capacitor. A series of etching steps finalizes the formation of our round trench capacitor. The last steps of this process are some implantation steps. First a boron doping is performed, as a threshold voltage adjustment step, it ensures that the substrate is still p doped at the surface. Then a thick photoresist layer is deposited, the thickness of 1 μm insures that no accidental doping of an undesired region can happen. After patterning, only a small window between the outer trench electrode and the quantum zone, where the transistor channel will be formed, is opened. This area is then heavily n doped with Arsenic – this will ensure an ohmic contact between the capacitor outer electrode and the region that will soon become the drain of our planar NMOS transistor. Recall that in a DRAM cell drain of the pass transistor and one capacitor electrode should lie on the same potential – which translates into a heavy doping and no voltage drop between drain region and capacitor electrode.

4.8.5 Gate Formation

In this step the gate oxide is deposited first with the desired thickness – 3 nm in our case. Then a thick polysilicon layer of approx. 100 nm is grown, followed by a photoresist deposition step. The gate photoresist is patterned and followed by a photoresist strip and polysilicon etching step, as can be observed in Figure 4.11. Finally, an oxide etching step with a reoxidation process follows, the new oxide covering the whole substrate and the polygate structure with a thickness of 5 nm.

4.8.6 Halo and Low Drain Doping Implantation

At 32 nm gate length, short channel effects will influence the transistor behavior. Particularly, the threshold voltage cannot be calculated by simply assuming charge conservation for a rectangular depletion region underneath the gate. When the junction depth of the source and drain regions lies in the same order of magnitude as the channel itself, this assumption no longer holds. Therefore, special steps have to be performed to avoid the large threshold voltage roll

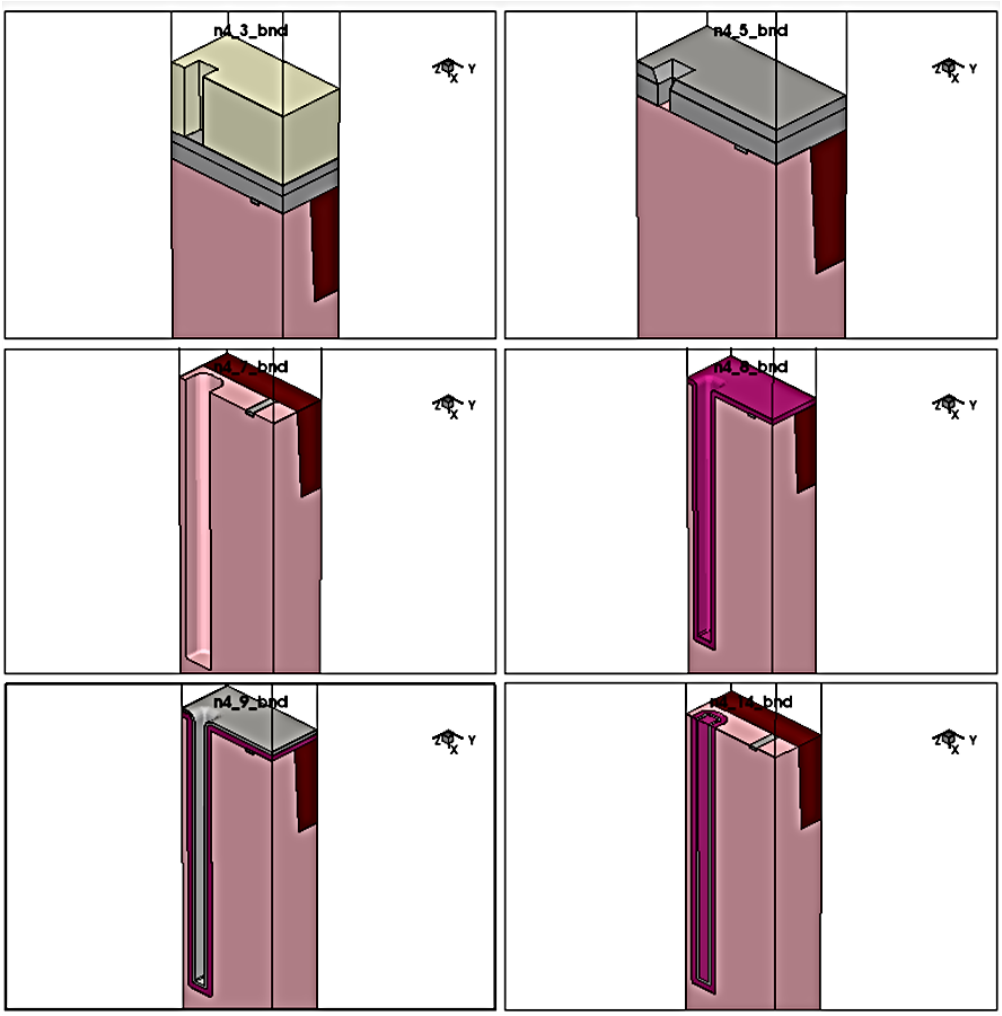

Figure 4.10: Deep trench (DT) formation process, including the ILD and photoresist deposition, etching, electrode and dielectric filling of the trench, followed by a final etching step.

off caused by the short channel effects. A halo implant step, using boron as n dopant, at various tilt angles is performed. This step is followed by a low drain doping (LDD) implantation, with a heavier dopant – Arsenic – at a low implantation energy, in order to ensure a shallow junction.

4.8.7 High Drain Doping

A MOS transistor still needs highly doped drain and source regions to work properly, independently of the channel length. We have seen that the effective channel length is controlled with the help of the halo doping; once this is defined the whole structure can be covered with a thick nitride layer. As can be seen in

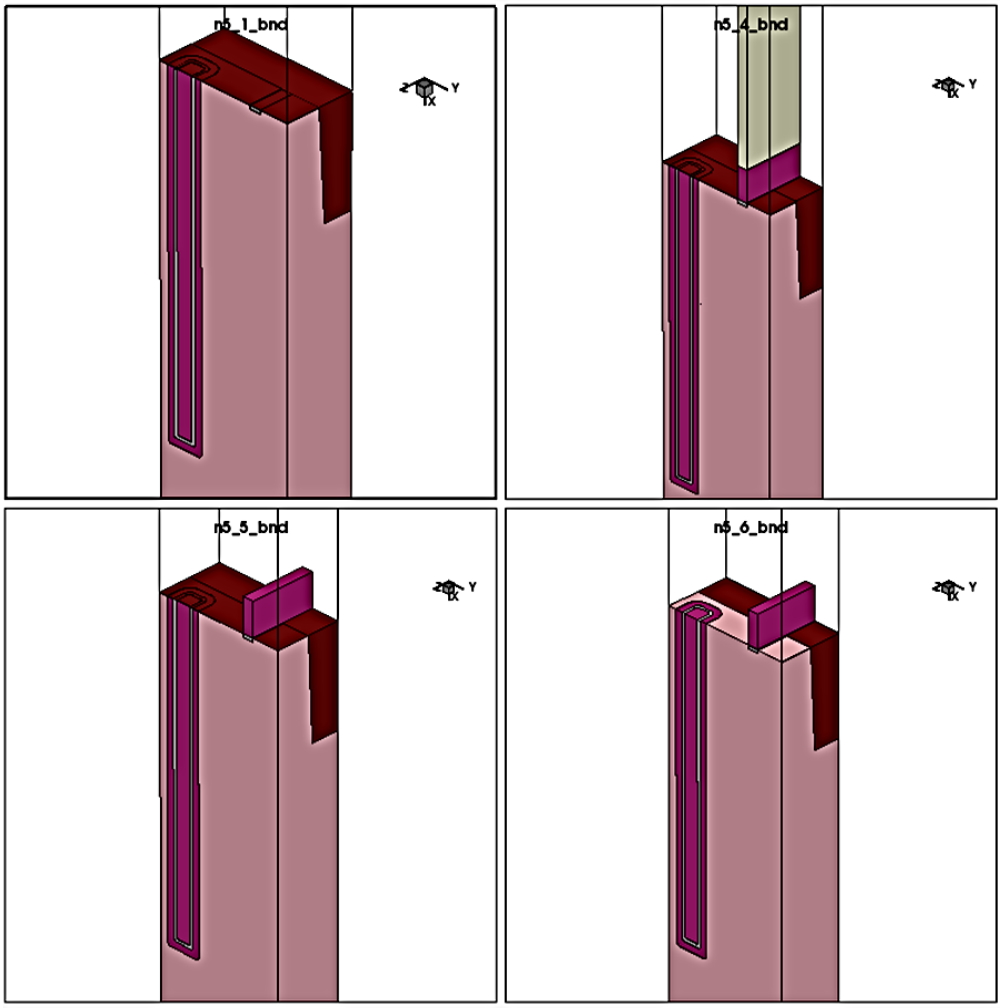

Figure 4.11: Gate oxide deposition followed by a patterning of the polysilicon gate on top.

Figure 4.12, this layer will deposit uniformly and also cover the poly gate region. An etching step is then performed: as already mentioned, this is an anisotropic process so depending on the etching rate and time one can control the shape and thickness of the nitride spacers around the poly gate. In our case, the resulting spacers have a thickness of around 35 nm, a typical value for this process. A heavy dopant implantation follows with a high implantation energy and dose to define the drain and source regions. The dopants are activated in a rapid thermal annealing step at over 1000 °C and the resulting doping profile can be viewed also in Figure 4.12.

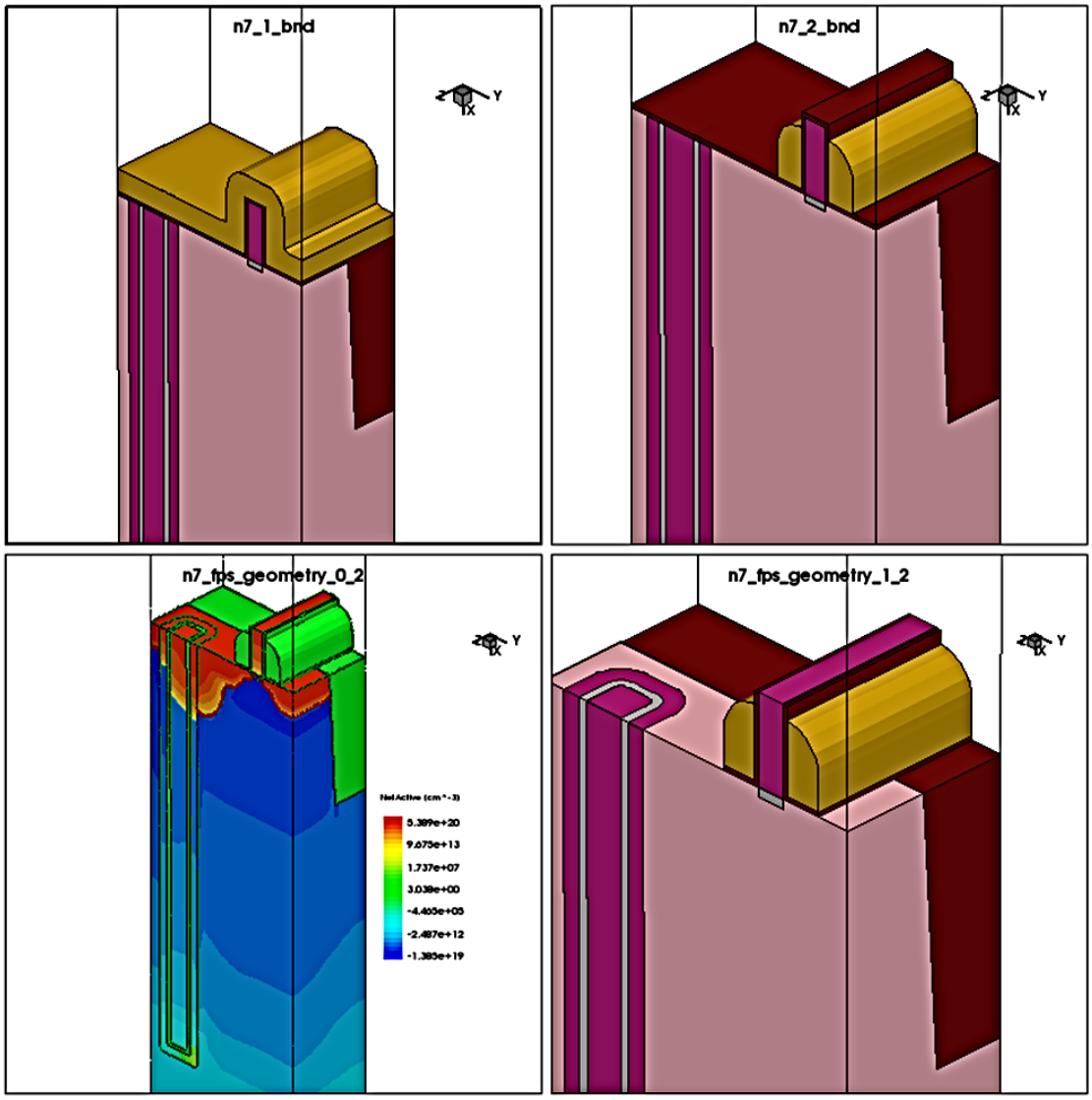

Figure 4.12: A thick nitiride spacer is deposited and anisotropically etched, in order to obtain the desired halo doping profiles.

4.8.8 Device Meshing

A mesh generated by the process simulator cannot be used – in most cases at least – for the electrical simulations, without some additional remeshing and definition of new refinement regions. The reason therefore is that the process simulator will sometimes use a finite elements scheme for solving e. g. the stress equation. Secondly, a nanometer scale refinement is often not needed to model a deposition or isotropic etching step. We will use for this last step the Sentaurus Mesh routine, the default meshing program for device simulations, instead of the MGOALS alternative. The global refinement and error parameters are set

to decent values for device simulation and an adaptive meshing algorithm is selected. For the refinement regions in the areas of interest, like the transistor channel, the highly doped source and drain regions or the trench dielectric, a layout driven refinement is again performed. The refinement regions are read from the exterior layout file and each of them will receive proper adaptive refinement criteria like the maximum edge length, maximum element angle for the Delauny mesh, etc. As a last step, the contacts of the DRAM cell are also defined and applied to the structure.

4.8.9 Final Structure

The resulting 3-D memory cell, together with the mesh used for the upcoming electrical characterization can be viewed in Figure 4.13. To summarize, the most important parameters are: a deep trench of 1 μm with a diameter of 100 nm, coated with a 10 nm SRO layer as electrode – and seed layer for the subsequent 10 nm STO high-*k* dielectric layer. The rest of the trench is filled again with SRO as the second electrode; the chosen geometry is similar to the structures published by Han *et al.* [56], which emphasize the good three dimensional conformality of the grown higher-*k* films. Four contacts can also be observed in the same picture: the NMOS pass-transistor has the standard source, gate and drain metallizations and the trench capacitor shares the drain contact as one electrode, while the second electrode will be shorted on ground potential for the rest of our analysis.

In order to better understand the refinement strategy, a look at the final doping profile is also helpful. In Figure 4.14 we can note that the bulk silicon substrate is slightly p doped. With a constant value of 10^{16} cm^{-3}, the deep bulk region is meshed using a coarse grid, since this area of the device will remain inactive during operation. As we approach the surface of the device, the p doping increases to around 10^{19} cm^{-3}. The reason for this high doping is the need for a threshold voltage adjustment; without it, an unintentional doping of the transistor channel area could lead to large fluctuations of the threshold voltage or, even worse, to normally on transistors. The mesh element size also decreases, as we get closer to the device surface; since the criterion for the adaptive meshing algorithm has been chosen as the gradient of the doping profile, the finer mesh in regions with higher p doping can be easily understood.

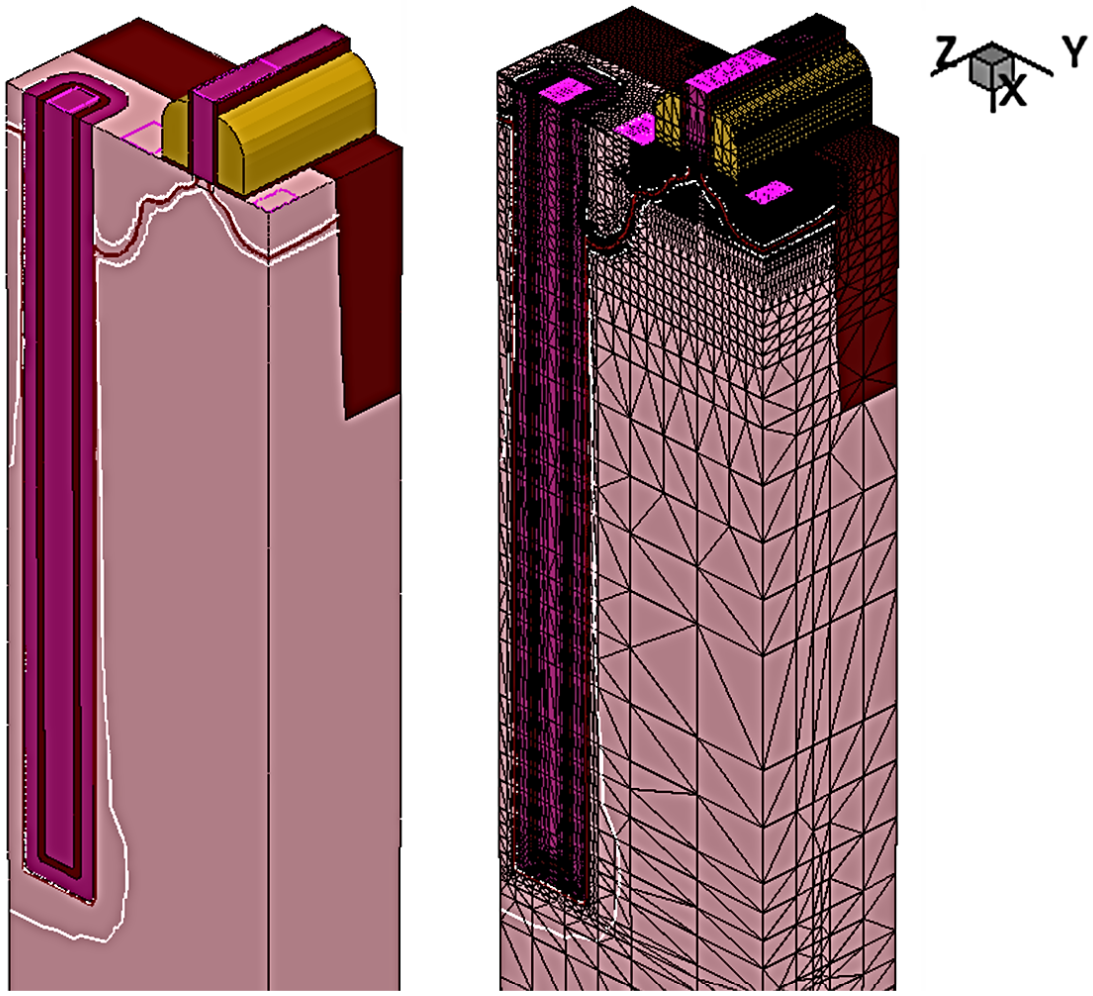

Figure 4.13: The final 3 dimensional structure of the 1T1C deep trench DRAM cell, together with the adaptive mesh constructed and used for the electrical simulations (taken from [69]).

The halo implants can also be observed, since they define the effective channel length of 32 nm. The deeper and heavier source and drain dopings are located at some distance from the effective gate length, due to the nitride spacers that partially shadow the channel region during the implantation step. Again a refined mesh is created in the areas with high doping due to the adaptive mesh criteria – based on the doping gradient.

Other important features of the final DRAM cell include the high n+ doping well between the drain of the NMOS and the trench capacitor electrode that ensures an ohmic contact; both trench electrodes are treated like polysilicon contacts with the material properties of SRO, this explains also the high n doping. Finally, a very refined mesh is constructed for the high-*k* dielectric of the trench structure

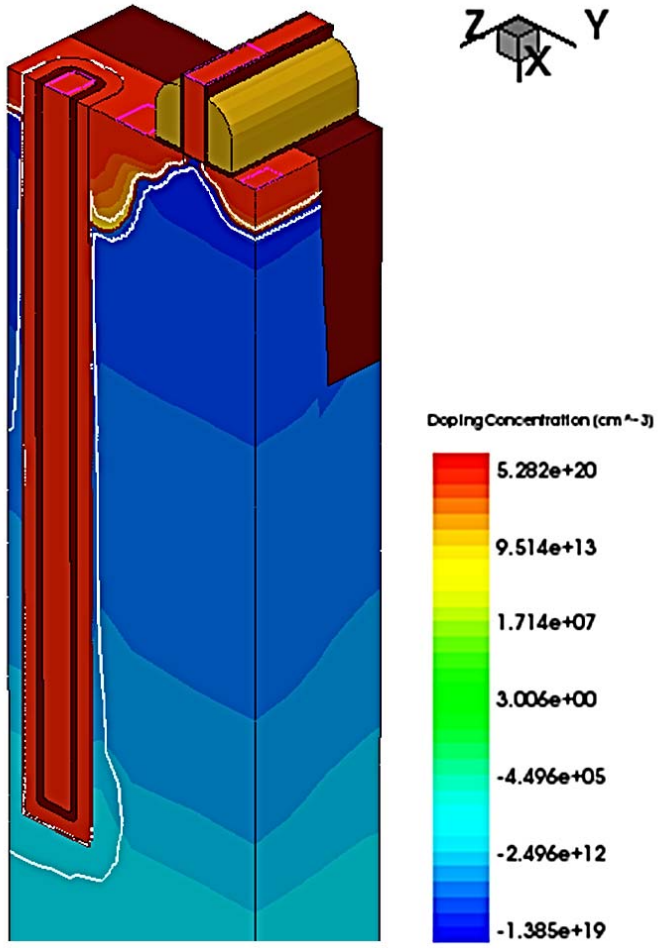

Figure 4.14: Final doping of the memory cell: the halo doping profiles of the pass transistor can be easily observed at the surface of the p-doped silicon wafer (taken from [69]).

– this mesh will be needed to activate the complex leakage mechanism for the dielectric layer.

Some concluding remarks on the process simulation: while the generated structure definitely resembles a real fabricated device, this modeling step is already a demanding one from the point of view of the computational resources. One has to take into account at least 36 hours of process simulation time with minimum 16 GB of RAM available. Maybe the most complex step of the whole process flow is the preparation of the mesh for the electrical simulations. Generating a high quality Delauney mesh on a structure with many rounded shapes, due to anisotropic etching steps, is not a trivial task. But since many parameters of the SRO/STO material system are stored in parameter files, they can easily be

modified without the need of regenerating or remeshing the DRAM structure. An electrical characterization of the memory cell is performed in the following section.

4.9 Electrical Simulation of the DRAM Cell

For the leakage properties, the complex transport model described in the model validation section above, is used for the dielectric layer of the trench capacitor. Nevertheless, the reduced defect concentration is simulated, emulating the case of an optimized fabrication process.

Concerning the pass transistor, a standard 32 nm NMOS currently in production is used, the electrical model being calibrated on measured samples reported e.g. [124]. The model employed for the pass transistor simulation includes some advanced physical mechanisms, since the charge transport in nano-length devices cannot be accurately described by a simple drift-diffusion approach anymore.

Due to the multiple doping steps, for the threshold voltage adjustment and also the halo and heavy drain doping, a doping dependent Shockley-Read-Hall (SRH) recombination model is activated [125]. The SRH recombination model calculates those recombination processes that occur through defect states in the bandgap of the semiconductor. This rate can be expressed as:

$$R_{net}^{SRH} = \frac{np - n_{i,eff}^2}{\tau_p(n + n_1) + \tau_n(p + p_1)} \tag{4.9.1}$$

with:

$$n_1 = n_{i,eff} \exp\left(\frac{E_{trap}}{k_B T}\right) \qquad p_1 = n_{i,eff} \exp\left(\frac{E_{trap}}{k_B T}\right). \tag{4.9.2}$$

Here E_{trap} is the energy difference between the defect level and the Fermi level in the semiconductor. The lifetimes τ_n and τ_p have a temperature dependent factor, in addition to the previously mentioned doping and a field dependence:

$$\tau_c = \tau_{dop} \frac{f(T)}{1 + g_c(F)} \tag{4.9.3}$$

with $f(T)$ being the temperature dependent function and $g_c(F)$ being the field enhancement factor. For the doping dependent lifetimes, the Scharfetter relation [126] is used:

$$\tau_{dop}(N_{A,0}+N_{D,0}) = \tau_{min}\frac{\tau_{max}-\tau_{min}}{1+\left(\frac{N_{A,0}+N_{D,0}}{N_{ref}}\right)^{\gamma}}. \tag{4.9.4}$$

The parameters for the SRH recombination models have been carefully calibrated with measured data [127] and are extensively used for TCAD modeling of CMOS technologies.

Following the same argumentation, a doping dependent mobility model for the charge carriers in the MOS channel is employed. Due to the charged impurity ions, the carrier scattering is expected to degrade the bulk mobility of the semiconductor; therefore the Masetti model for the doping dependent mobility is used, a model which achieves good agreement to measured doped silicon samples [128]. The dependency is implemented as follows:

$$\begin{aligned}\mu_{dop} = \mu_{min1}\exp\left(-\frac{P_C}{N_{A,0}+N_{D,0}}\right) + \frac{\mu_{const}-\mu_{min2}}{1+((N_{A,0}+N_{D,0})/C_r)^{\alpha}} - \\ - \frac{\mu_1}{1+(C_S/(N_{A,0}+N_{D,0}))^{\beta}}.\end{aligned} \tag{4.9.5}$$

The employed parameters, such as the reference mobilities μ_{min}, doping concentrations P_C, C_r, C_S etc., are all again calibrated over a wide range of doping concentrations for silicon samples.

Coupled with the doping dependent mobility, a high field saturation model is also used for the electrical characterization of the device. For short channel devices, at high electric fields the drift velocity of the carriers will no longer increase, but saturate at a certain value. As a comment, when multiple mobility models are activated, the resulting average mobility is computed following the Matthiessen rule as:

$$\frac{1}{\mu_{total}} = \frac{1}{\mu_1}+\frac{1}{\mu_2}+\cdots+\frac{1}{\mu_N}. \tag{4.9.6}$$

The high field saturation model actually computes three different effects of the electric field: the impact on the actual mobility, the velocity saturation approximation and the correction to the driving force term. For the simulations below, the extended Canali model [129] is chosen for the high field saturation mobility, being the default choice for silicon devices. Within this model, the mobility is computed as:

$$\mu(F) = \frac{(\alpha+1)\mu_{low}}{\alpha + \left[1 + \left(\frac{(\alpha+1)\mu_{low}F_{hfs}}{v_{sat}}\right)^{\beta}\right]^{1/\beta}}. \tag{4.9.7}$$

The temperature parameter beta is equal to:

$$\beta = \beta_0 \left(\frac{T}{300\mathrm{K}}\right)^{\beta_{exp}} \tag{4.9.8}$$

and for the saturation velocity and driving force we will use:

$$v_{sat} = v_{sat,0}\left(\frac{300\mathrm{K}}{T}\right)^{v_{sat,exp}}. \tag{4.9.9}$$

$$F_{hfs,n} = |\nabla \Phi_n|. \tag{4.9.10}$$

Where $|\nabla \Phi_n|$ is the gradient of the quasi-Fermi potential.

Additionally, the degradation of the mobility at the silicon/silicon oxide interface, due to acoustic phonon scattering is taken into account by activating the Lombardi model [130]. For this mobility degradation model, the calculation of the normal electric field in the channel region is essential. We therefore need a very refined mesh at this interface, with a spacing of around 0.1 nm between grid lines. The Lombardi model introduces two new mobility terms, that together with the doping dependent and high field saturation mobility terms, will all combine according to the Matthiessen rule stated above to give the actual mobility in the MOS channel. The two terms that account for the acoustic phonon and surface roughness scattering are:

$$\mu_{ac} = \frac{B}{F_\perp} + \frac{C((N_{A,0} + N_{D,0} + N_2)/N_0)^{\lambda}}{F_\perp^{1/3}(T/300\mathrm{K})^{k}}. \tag{4.9.11}$$

$$\mu_{sr} = \left(\frac{(F_\perp / F_{ref})^{A^*}}{\delta} + \frac{F_\perp^3}{\eta} \right)^{-1}. \tag{4.9.12}$$

We denote here with F_{ref} a reference electric field, in order to ensure a unitless numerator, while the transverse electric field at the insulator-semiconductor interface is $F_\perp$.

To conclude, beside the SRH recombination and a doping, field and interface dependent mobility model, we also perform quantum corrections to the potential in the channel region of our pass transistor. Due to the inherent wave nature of the charge carriers at deep sub-μm scales, quantization effects cannot be neglected anymore; they can already be observed in a small shift of the threshold voltage or in the reduction of the gate capacitance. The quantization effects can be easily modeled, by introducing an extra potential term to correct the electron or hole density formulas:

$$n = N_C F_{1/2} \left(\frac{E_{F,n} - E_C - \Lambda}{k_B T_n} \right). \tag{4.9.13}$$

The Lambda potential can be approximated in the density gradient gradient approach [131, 132] with:

$$\Lambda_n = -\frac{\hbar^2}{6 m_n} \frac{\nabla^2 \sqrt{n}}{\sqrt{n}}. \tag{4.9.14}$$

Performing some substitutions and rewriting some terms, like $\beta = 1/k_B T_n$, $\Phi_m = -k_B T_n \ln(N_C / N_{ref})$, $\bar{\Phi} = E_C + \Phi_m + \Lambda_n$ one can write a more general and potential-based expression for our lambda variable:

$$\begin{aligned} \Lambda_n = -\frac{\gamma \hbar^2}{12 m_n} [& \nabla \cdot \alpha(\xi \nabla \beta_{F,n} - \nabla \beta \bar{\Phi} + (\eta - 1) q \nabla \beta \phi) + \\ & + \vartheta(\xi \nabla \beta_{F,n} - \nabla \beta \bar{\Phi} + (\eta - 1) q \nabla \beta \phi) \cdot \\ & \cdot \alpha(\xi \nabla \beta_{F,n} - \nabla \beta \bar{\Phi} + (\eta - 1) q \nabla \beta \phi). \end{aligned} \tag{4.9.15}$$

The calibrated model values for deep sub-micrometer silicon devices are: $\xi = \eta = 1$, $\vartheta = 1/2$ and $\alpha = 1$ [131].

4.10 Feasibility Study

The first simulation that has been performed is an I_d-V_g characteristic of the pass transistor embedded in the DRAM cell. For this purpose, the drain voltage is first ramped up to a value of 1 V. Then the gate electrode is slowly swept to the negative voltage of -1 V and then back to positive 1 V. As can be observed in Figure 4.15, the leakage current at negative and lower than threshold gate voltages is very small, proving that a low defect density in the dielectric of the trench capacitor will have no major impact and making this virtual memory cell suitable for data retention. In the same figure, the transfer characteristic for a 45 nm gate length pass transistor of a modeled DRAM cell is shown, together with the 32 nm transistor, to emphasize the scaling effects of the gate length. Not surprisingly, the total current of the 32 nm gate length NMOS is higher at 1 V gate and 1 V drain bias. A higher current implies that more charges can be injected in the storage capacitor during a memory write cycle or if we decide to keep the stored charge constant, faster operation is possible. Another figure of merit, the threshold voltage, can be extracted from the transfer curve.

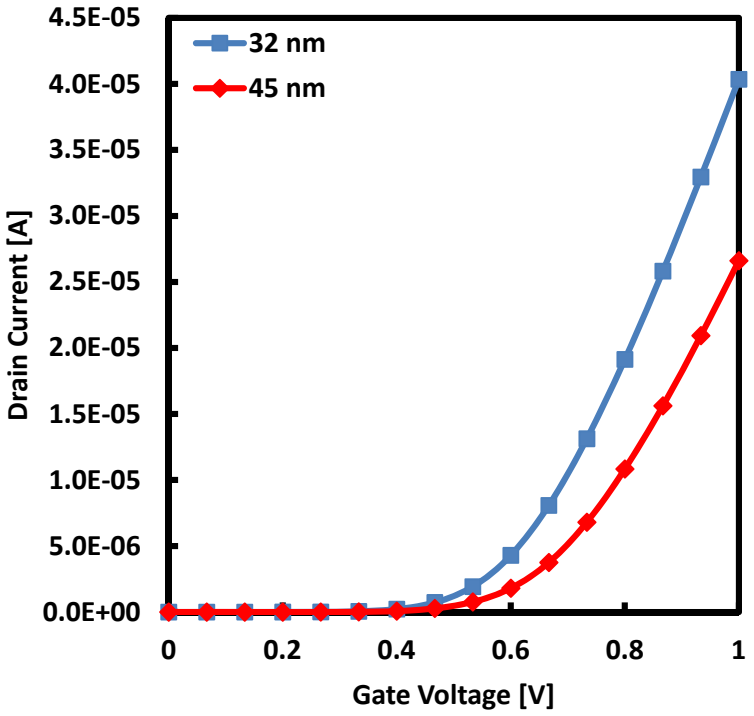

Figure 4.15: Simulated I-V characteristics of a 45 and 32 nm pass transistor, typically used for DRAM cells (taken from [69]).

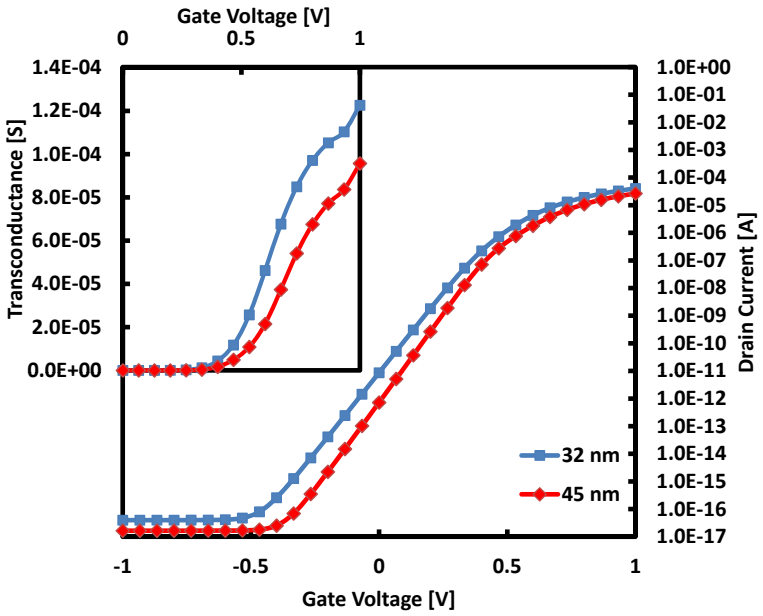

Figure 4.16: A typical figure of merit for CMOS transistors, the transconductance of the 32 and 45 nm gate length transistors, extracted from the above given transfer characteristics.

The values are V_{th}=0.63 V for L_g=32 nm and V_{th}=0.69 V for L_g=45 nm, respectively. A 10 % decrease of the threshold voltage is a remarkable improvement, since it translates into lower operating voltages for a memory array, a crucial requirement e.g. for mobile devices.

In Figure 4.16, the transfer characteristic for the two devices in semi-log scale is shown together with the transconductance g_m. A high frequency analysis of a DRAM cell is outside the scope of this work, but it must be briefly mentioned that the transconductance of a device gives a first hint on the performance at higher frequencies. Obviously, the higher the operating frequency can be, the faster the read and write cycles can be performed, making the memory cell attractive for e.g. real-time systems. The maximum values extracted for gm are of 122 μS and 95 μS respectively, for the 32 and 45 nm NMOS. It can be observed however that the two transconductance curves are still increasing and have not reached their maximum under the performed bias sweeps; increasing the gate voltage would most probably still increase the transconductance of the two devices, but operating voltages larger than 1-1.2 V are not realistic for the future DRAM memory arrays.

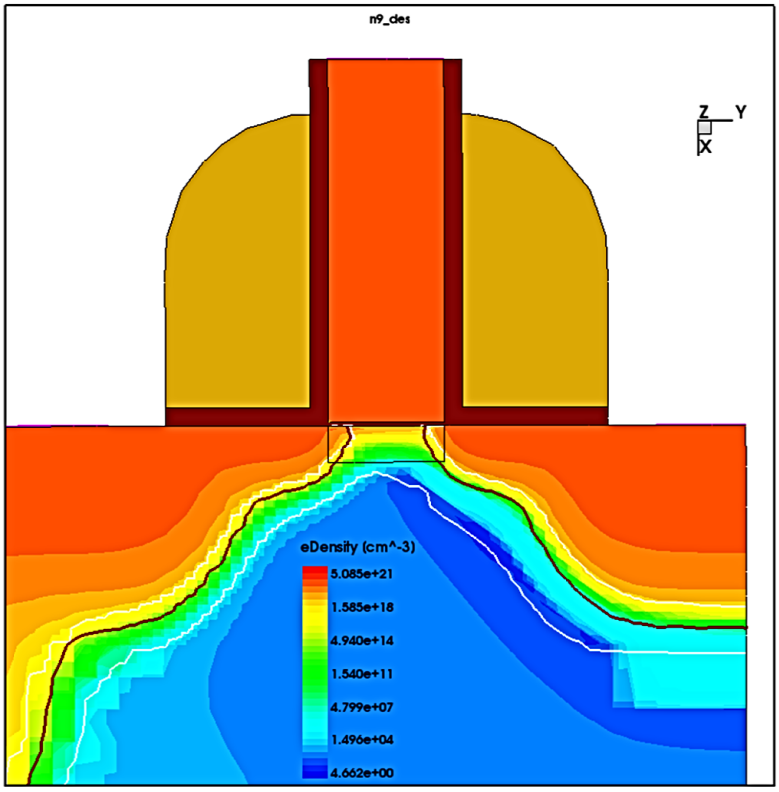

Figure 4.17: Electron density in the channel region, when the pass transistor is turned on: the high electron density, in excess of 10^{20} cm^{-3}, justifies the complex models employed for the mobility and recombination.

In Figure 4.17 and Figure 4.18 we can observe the distribution of the electron density and the absolute electric field for the 32 nm pass transistor under operation – again the bias point is $V_d = V_g = 1$ V. Looking at the Figure 4.17 we can conclude that the choice of using the doping dependent mobility is justified, since the electron densities in the contact regions but also in the channel are very large. The absolute electric field also shows values exceeding 10^6 V/cm^2 but analyzing the two components of the electric field separately gives us an even better idea about the charge transport mechanisms inside the transistor. The field component parallel to the channel is shown in Figure 4.19: due to the relatively high bias voltage and large doping concentration the parallel electric field is high for most of the channel region. Again, the high field saturation model for the mobility seems justified, since at fields of around 10^6 V/cm^2 one cannot expect that the drift velocity of the electrons will continue to increase. Finally, in Figure 4.20 we can observe that the electric field normal to channel region is strongly localized in the gate dielectric; nevertheless large values of the

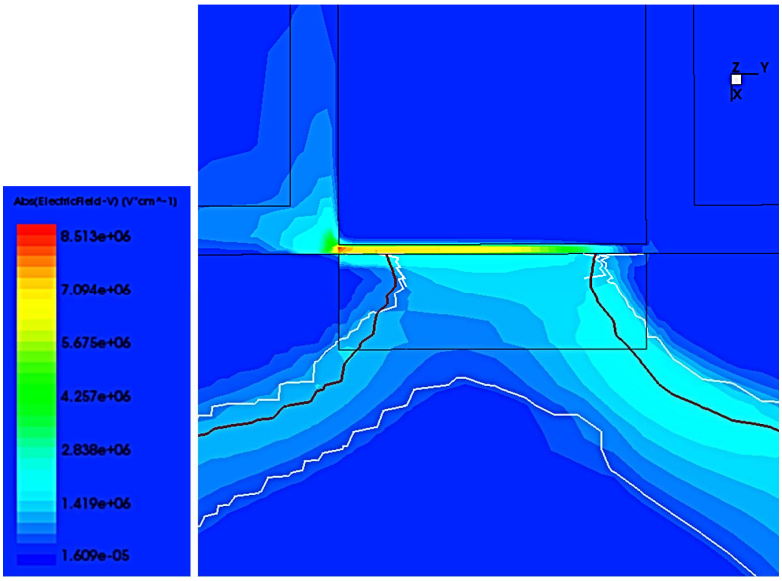

Figure 4.18: Total electric field for the biased pass transistor.

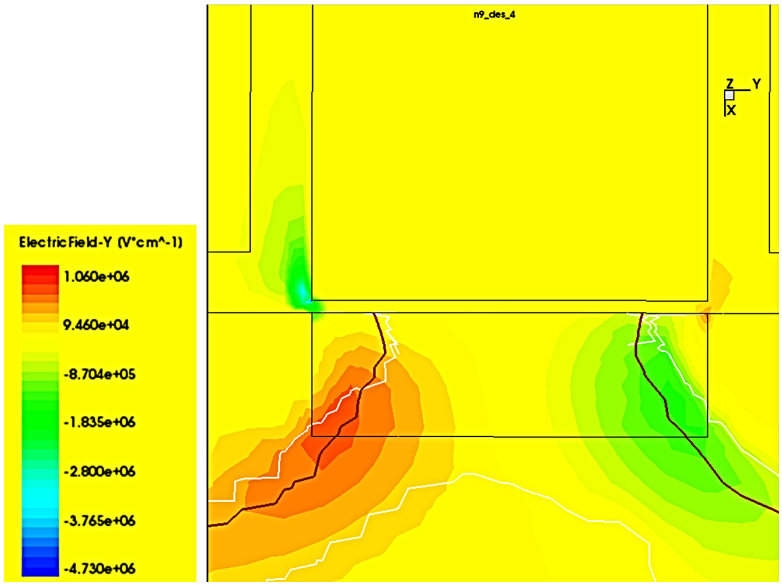

Figure 4.19: The parallel electric field in the channel region reaches 10^6 V/cm^2, making it necessary to activate some additional models, like the high field saturation mobility.

x component can still be observed directly under the gate oxide, having for sure an impact on the carrier flow below.

Although the 3 dimensional DRAM cell simulation shows that such an architecture would work well for memory application, the main advantage of higher-k

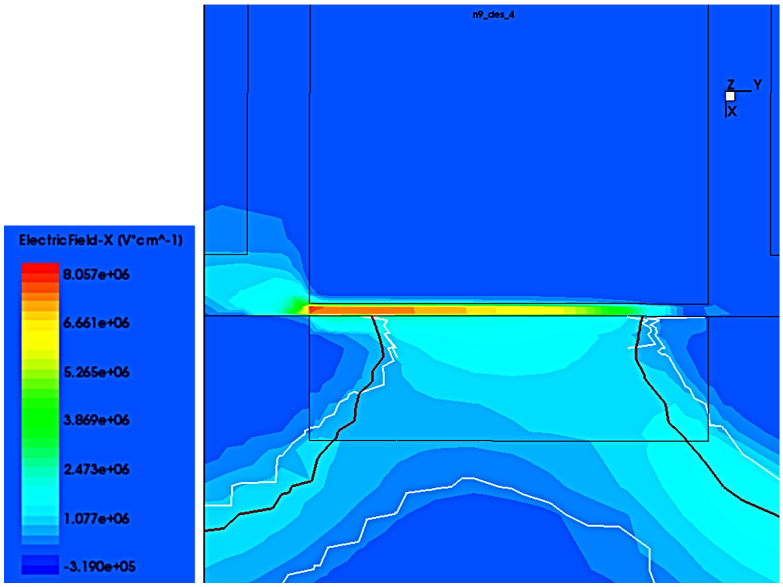

Figure 4.20: The normal electric field under the gate dielectric, suggesting that the Lombardi model for mobility degradation due to scattering at the Silicon/dielectric interface is necessary.

materials are their far superior charge retention capabilities, when compared with standard SiO_2 or high-k materials like HfO_2.

In order to point out the benefits of the proposed material system, when compared with standard approaches, two more cases are analyzed, both for 3D 1T1C trench DRAM cells. We therefore simulate the behavior of a PolySi/SiO_2/PolySi and of a PolySi/HfO_2/PolySi, trench capacitor cell, respectively, both having the same 32 nm gate length pass transistor as in the case of the SRO/STO/SRO DRAM cell, equal trench area and the same thickness of the dielectric layer.

A quasistationary ramp is performed for all three cases, where the source electrode of the pass transistor, which is also one of the capacitor's electrodes, is slowly ramped up, until it reaches a voltage of 1 V. Not only the electron, hole and total current on the device electrodes are stored after each incrementation of the source voltage, but also the total charge on the electrodes – since the Poisson equation is solved for each iteration. Knowing that, in general, one can define the capacitance as:

$$C = dQ/dU \tag{4.10.1}$$

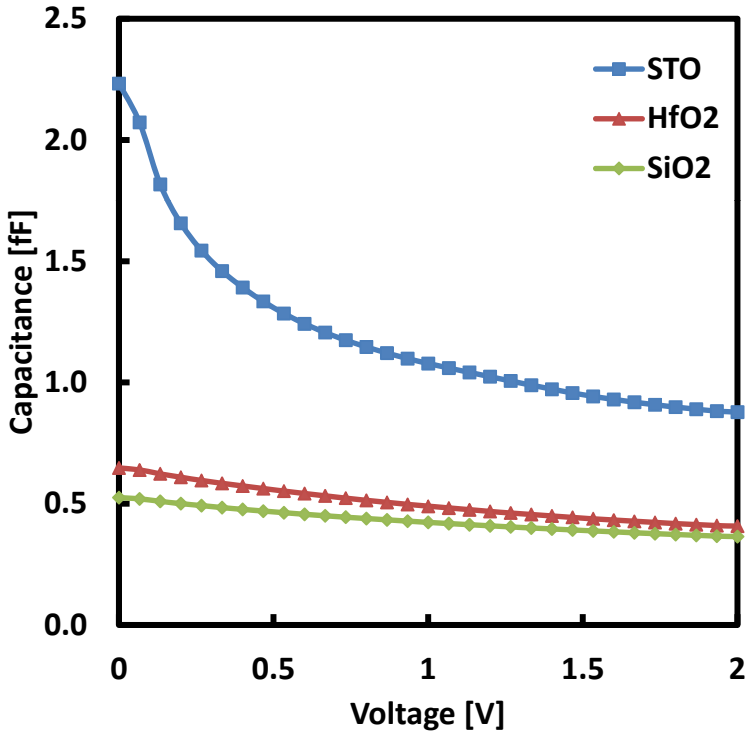

Figure 4.21: Deep trench capacitance vs. drain electrode voltage for three examined capacitor structures: a SRO/STO/SRO configuration, a Polysilicon/Silicon oxide and finally a Polysilicon/Hafnium oxide one (taken from [69]).

we can simply evaluate the capacitance of the trench structure by derivating the stored charge with respect to the ramped terminal voltage.

The three cases are shown in Figure 4.21 and confirm the advantages of higher-k materials, the STO trench capacitor having the largest capacitance. One can also note that the capacitance-voltage characteristic is nonlinear for all three structures; this fact is mainly attributed to the parasitic source-body depletion capacitance. Since our substrate is p-doped and the source region is n-doped, when applying a positive voltage we will have a reverse biased pn diode between source and body of the DRAM cell. This parasitic depletion capacitance, in series with our trench capacitance, will result in the total capacitance depicted in Figure 4.21. Several strategies to reduce the depletion capacitance could be applied, but they would all imply additional fabrication steps and increased complexity of the structure.

While for the standard case of a Polysilicon/Silicon oxide trench structure the extracted capacitance at 1 V is about 0.42 fF, the use of a high-*k* dielectric like HfO_2 already shows a slight improvement – an increase until 0.49 fF.

The SRO/STO/SRO material system shows the highest capacitance value, with a remarkable 1.1 fF. As a concluding remark, the values for the extracted capacitance should be multiplied with a factor of 2, since we have only modeled half of the geometry for the DRAM cell. The reason therefore can be found in the symmetry of the modeled structure: in the case of a half-cell the simulation speed is increased and the need for computational resources reduced, since the number of mesh vertices is halved.

4.11 Discussion

In this chapter we have performed an extensive simulation study making use of the findings from our kinetic Monte Carlo simulations, on the nature of the high leakage current measured for the fabricated high-*k* thin film capacitors.

For this task we have employed a drift-diffusion simulator, which also models elastic and inelastic trap assisted hopping processes and trap relaxation effects in the dielectric film. The measured leakage currents have been validated over an interval of 110 K, typical for DRAM operation. We have confirmed that oxygen vacancies form percolating paths in the dielectric bulk and are responsible for the observed enhanced leakage behavior, in good agreement with our kMC simulation results of the previous chapter and also with experimental observations [73]. Almost identical parameters as those extracted with MC techniques are used for the trap concentration, conduction band offset and trap depth.

Using an optimized thin film capacitor structure, with a reduced number of defect states, a complex 3-D simulation of a 1T1C DRAM cell is performed. A 32 nm NMOS is also modeled for the pass transistor; advanced transport models, including high field saturation, doping dependent mobility and quantum corrections are applied in order to accurately model the operation of the three-terminal device.

The transfer characteristic is simulated in order to determine the subthreshold swing and the threshold voltage. The charge distribution inside the memory cell

is stored during a voltage ramp and thus the cell capacitance is extracted. The same procedure is repeated for several other trench dielectric materials and the results compared.

This complex full 3D simulation also confirms that our proposed high-*k* material choice for the trench capacitor can be successfully implemented in real device application, if the defect densities in the STO film can be decreased at least two orders of magnitude. Since, as already mentioned, recent experimental work by Pawlak *et al.* shows very promising results in the direction of defect-free material engineering, our simulation underlines that even under realistic operating voltages and for 3-D geometries, a poor defect STO trench capacitor will still exhibit very small leakage currents.

We emphasize that the implementation of the above described complex leakage mechanism in a well established TCAD framework offers unprecedented flexibility, post processing or visualization capabilities coupled with fast simulation times. Improved and robust numerical solvers assure the high accuracy of the simulation results. The possibility to use a graphical interface environment also increases the user-friendliness and gives researchers from other fields of interest the chance to examine the topic of leakage in high-*k* dielectrics with only short learning times.

5 Kinetic Monte Carlo Simulations

We will start our kMC analysis with a short discussion of all possible leakage mechanisms that can play a role for our fabricated MIM structures. The major advantage of the kMC method is that once implemented, the stochastic algorithm will identify the dominant leakage channnels and give also the correct time evolution of our system.

5.1 Leakage Mechanisms

5.1.1 Tunneling

The potential landscape seen by an electron, for a biased MIM structure, is shown in Figure 5.1. We will deal in the following only with electron tunneling since, as one can see from the band structure in the figure below, the potential barrier seen by holes in the electrodes is much larger than that seen by electrons. When talking about tunneling through potential barriers, two parameters characterize this classically forbidden zone for electrons: the conduction band offset (CBO) – which is the difference between the workfunction of the electrode and the level of the oxide conduction band – and the barrier width, equal to the thickness of the oxide layer in our case, which has a value of 10 nm.

Assuming a Fermi-Dirac distribution of the charge carriers in the two electrodes and a nondegenerate, parabolic conduction band minimum, the well-known Tsu-Esaki [133,134] expression of the tunneling current density can be derived:

$$\begin{aligned} j_{DT} &= \frac{em^*}{2\pi^2\hbar^3}\int_0^\infty dE_x T(E_x)\int_0^\infty dE' E'\left[f_l(E_x,E') - f_r(E_x,E')\right] \\ &= \frac{em^*}{2\pi^2\hbar^3}\int_0^\infty dE_x T(E_x)\ln\left(\frac{1+e^{(E_{f,l}-E_x)/(k_BT)}}{1+e^{(E_{f,l}-eU-E_x)/(k_BT)}}\right) \end{aligned} \tag{5.1.1}$$

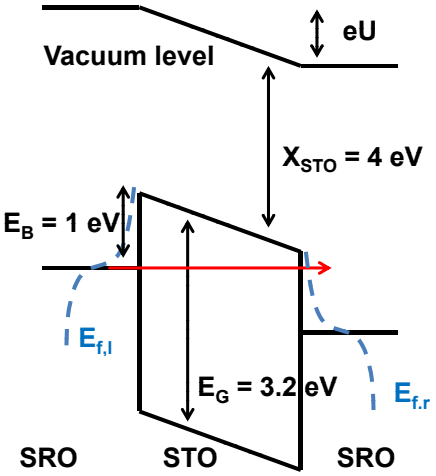

Figure 5.1: Schematic of a tunneling process through a thin SRO/STO/SRO capacitor, under applied bias.

where we denote with $E_{f,l}$ the Fermi energy level at the left injecting contact, U the applied bias and $T(E)$ the transmission coefficient. The transmission coefficient is defined as the probability flux between the transmitted wave package and the incident wave, at a potential discontinuity. Usually, for tunneling through barriers, the transmission coefficient is calculated from the ratio of the probability current densities. A common practice for computing $T(E)$ in arbitrary potential landscapes is to divide the potential barrier in a large number of infinitesimal rectangular potential barriers, for which the calculation of the transmission coefficient can be easily performed. This procedure is also the basis of the Wentzel-Kramers-Brillouin (WKB) [135] approximation that leads to the following expression for $T(E)$:

$$T(E) \approx \frac{e^{-2\int_{x_0}^{x_1} dx \sqrt{\frac{2m^*}{\hbar^2}(V(x)-E)}}}{\left(1+\frac{1}{4}e^{-2\int_{x_0}^{x_1} dx \sqrt{\frac{2m^*}{\hbar^2}(V(x)-E)}}\right)^2} \approx e^{-2\int_{x_0}^{x_1} dx \sqrt{\frac{2m^*}{\hbar^2}(V(x)-E)}}. \tag{5.1.2}$$

Some important remarks on the calculation of the tunneling current density still need to be made. The choice of the Tsu-Esaki formula, although confusing at first due to its complex form and increased effort to numerically evaluate it, has some advantages over simpler tunneling models. It can cover a large range of temperatures and electric fields [134]: for the high temperatures and

low electric fields regime, when one typically considers the Schottky emission as the dominant mechanism, the Tsu-Esaki expression is still a good approximation when compared to the Richard-Dushman equation:

$$j_{SE} = \frac{em^* k_B^2 T^2}{2\pi^2 \hbar^3} \exp\left[-\frac{1}{k_B T}\left(E_B - \sqrt{\frac{e^3 F}{4\pi\epsilon_0 \epsilon_{opt}}}\right)\right] \tag{5.1.3}$$

with E_B being the potential barrier seen by the charge carrier, between the injecting metal electrode and the oxide and F the applied electric field. Analogous, when considering high electric fields at moderate temperatures, one would typically consider Fowler-Nordheim tunneling as dominant:

$$j_{FN} = \frac{e^3 F^2}{8\pi h E_B} \exp\left(-\frac{4\sqrt{2m^* E_B^3}}{3\hbar e F}\right). \tag{5.1.4}$$

The Tsu-Esaki model includes these two corner cases and also the whole temperature and voltage interval in between, making it an attractive option for studying the tunneling currents through thin oxide layers.

5.1.2 Charge Injection from and Collection into Electrodes

As already mentioned, one main problem that remains to be solved is the defect free fabrication of high-k dielectric layers. Since, however, recent studies indicate that for STO large defect concentrations can be measured, their impact on the leakage behavior of o MIM structure needs to be analyzed. The first step that needs to be analyzed, when considering trap-assisted tunneling through a dielectric, is the charge injection from an electron reservoir or electrode and the charge collection at the other electrode. As one can observe in Figure 5.2, both elastic and inelastic electron injection/collection at the electrodes can be of importance. Let us first start with the elastic case.

Elastic Injection and Collection

We can start our analysis by assuming a metal electrode and a defect rich oxide. Then one can express the tunneling probability of an electron into a defect near

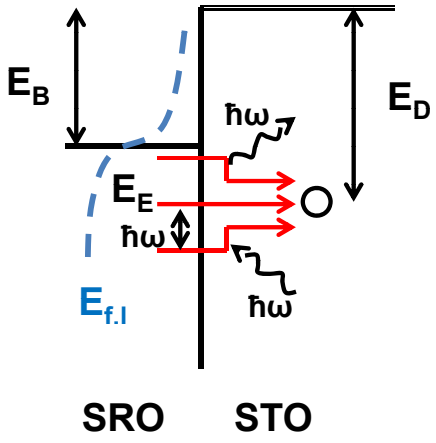

Figure 5.2: Elastic and inelastic (under emission/absorption of phonons) tunneling of electrons from a metal electrode (SRO) into a trap state of the (STO) dielectric layer:.

the electrode using the expression derived by Lundström *et al.* [136], and conveniently rearranged as in [137], to make use of the already calculated transmission coefficient:

$$P = \frac{4}{3}\frac{\hbar m_e k_0^3}{m_i^2 K} T(E_e) = \left(\frac{m_e}{m_i}\right)^{5/2} \left(\frac{8E_e^{3/2}}{3\hbar\sqrt{E_D}}\right) T(E_e) \tag{5.1.5}$$

where m_e and m_i are the electron mass in the metal and insulator, respectively, $K = \sqrt{2m_i E_D/\hbar^2}$ with E_D the energetic depth of the defect localized inside the insulator's bandgap, $k_0 = \sqrt{2m_e E_e/\hbar^2}$ and E_e the electron energy level in the electrode. To obtain a tunneling rate, one still has to multiply the above expression with the probability that there will be an electron in the electrode with E_e energy. This step implies nothing more than to multiply the expression with a Fermi-Dirac distribution $f(E_e)$:

$$T_{ED}^{el} = \frac{4}{3}\frac{\hbar m_e k_0^3}{m_i^2 K} T(E_e) = \left(\frac{m_e}{m_i}\right)^{5/2} \left(\frac{8E_e^{3/2}}{3\hbar\sqrt{E_D}}\right) T(E_e) f(E_e). \tag{5.1.6}$$

For electron collection, from a defect state into the metal electrode, one can similarly deduce:

$$T_{DE}^{el} = \frac{4}{3}\frac{\hbar m_e k_0^3}{m_i^2 K} T(E_e) = \left(\frac{m_e}{m_i}\right)^{5/2} \left(\frac{8E_e^{3/2}}{3\hbar\sqrt{E_D}}\right) T(E_e)(1 - f(E_e)). \tag{5.1.7}$$

Inelastic Injection and Collection

The inelastic case will treat the injection process as a multi-phonon assisted tunneling process. We will in the following use the derivation of Herrmann et al. [138], under the assumption of a single-mode coupling approximation of the phonons in the dielectric. Under this conditions the tunneling rates for an electron in the metal electrode into a defect T_{ED}^{inel} and the reverse process T_{DE}^{inel} can me modeled as:

$$\begin{aligned} T_{ED}^{inel} = &\sum_{p<0}^{\infty} c_0 N_E(E_p) f(E_p) T(E_p, x) P_p(z) \cdot e^{\frac{p\hbar\omega}{k_B T}} \\ &+ \sum_{p>0}^{\infty} c_0 N_E(E_p) f(E_p) T(E_p, x) P_p(z) \end{aligned} \tag{5.1.8}$$

$$\begin{aligned} T_{DE}^{inel} = &\sum_{p<0}^{\infty} c_0 N_E(E_p)[1 - f(E_p)] T(E_p, x) P_p(z) \\ &+ \sum_{p>0}^{\infty} c_0 N_E(E_p)[1 - f(E_p)] T(E_p, x) P_p(z) \cdot e^{\frac{p\hbar\omega}{k_B T}} \end{aligned} \tag{5.1.9}$$

where he have used the following quantities and functions:

$$N_E(E) = \frac{1}{2\pi^2}\left(\frac{2m_e}{\hbar^2}\right)^{3/2} \sqrt{E - E_c} \cdot \Theta(E - E_c) \tag{5.1.10}$$

for the density of states in the metal electrode, with Θ the Heaviside function and E_c the conduction band edge. The c_0 constant can be approximated with [139]:

$$c_0 = \frac{(4\pi)^2 r_D^3}{\hbar E_g} \frac{e^2 \hbar^2 F^2}{2m_i}. \tag{5.1.11}$$

Furthermore $r_D = \hbar/\sqrt{2m_i E_D}$ is the localization radius of a charge carrier trapped in a defect state, with the energetic depth E_D inside the insulator

bandgap E_G and F is the applied electric field. The Bose-Einstein distribution f_{BE} is defined as:

$$f_{BE} = \frac{1}{\exp\left(\frac{\hbar\omega}{k_B T}\right) - 1} \tag{5.1.12}$$

and finally the P_p term represents the is multiphonon transition probability

$$P_p(z) = \left(\frac{f_{BE}+1}{f_{BE}}\right)^{p/2} \exp[-S(2f_{BE}+1)] I_p(z) \tag{5.1.13}$$

with S denoting the Huang Rhys factor, $z = 2S\sqrt{f_{BE}(f_{BE}+1)}$ and I_p the modified Bessel function of order p.

5.1.3 Trap Assisted Tunneling

In the previous section, the process of injecting electrons into a defect state located in the dielectric layer and the collection of electrons from such defect states was been derived. The trap-assisted tunneling (TAT) process that can lead to an increased leakage current can also be an elastic process or an inelastic process, as depicted in Figure 5.3. Elastic TAT can take place either when no bias is applied, if we have a sharply defined defect level inside the bandgap of the dielectric or at applied bias, if our trap distribution can be described e.g. by a broad exponential function and we can find transitions between two defects where no phonon absorption or emission is needed. Inelastic TAT, on the other hand, can take place between any defect states independent of the biasing conditions and will be also discussed in the next section.

Elastic Trap Assisted Tunneling

The elastic TAT process can be viewed as a hopping process between localized defect states. It can be modeled accurately using Mott's transition rate [140]:

$$T_{DD}^{el} = \nu \cdot \exp\left(\frac{-2r_{ij}}{r_D}\right). \tag{5.1.14}$$

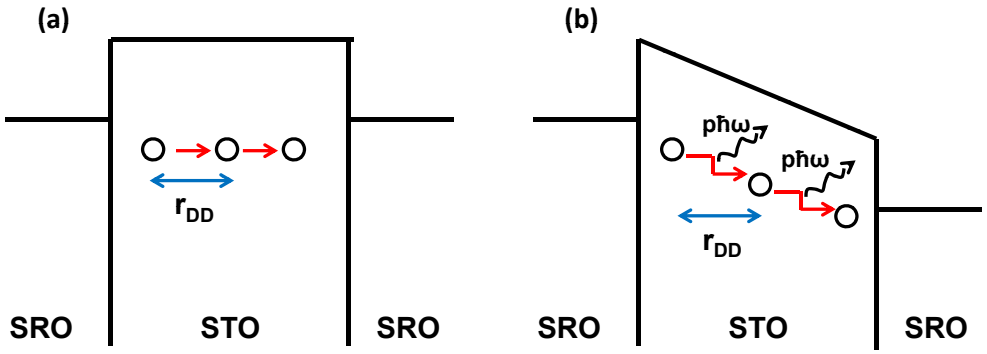

Figure 5.3: An elastic trap assisted tunneling (TAT) process (a) and an inelastic process under phonon emission (b).

In the upper formula ν is the typical attempt-to-escape phonon frequency, r_{ij} is the distance between two defects located at positions r_i and r_j and r_D the localization radius, as previously defined in equation 5.1.11:

$$r_D = \frac{\hbar}{\sqrt{2m_i E_D}}. \tag{5.1.15}$$

Inelastic Trap Assisted Tunneling

For the inelastic case, one must also take into account the electron-phonon interaction that lead to an energy exchange between the electron and the lattice of the dielectric. Ridley et al. [141] handled this situation and gave the following expression for this inelastic tunneling process:

$$T_{DD}^{inel} = T_{ij}(E_i, r_{ij}) c_{ij}(E_i, E_j). \tag{5.1.16}$$

The rate constant c_{ij} for the inelastic phonon-assisted trap-to-trap transition has been approximated in the same study with:

$$c_{ij}^{-} = R_0 (f_{BE} + 1)^p \exp(-2 f_{BE} S) \tag{5.1.17}$$

$$c_{ij}^{+} = R_0 f_{BE}^p \exp(-2 f_{BE} S) \tag{5.1.18}$$

depending whether the transition occurs under phonon emission c_{ij}^{-} or absorption c_{ij}^{+}. Here f_{BE} and S are the already mentioned Bose-Einstein distribution

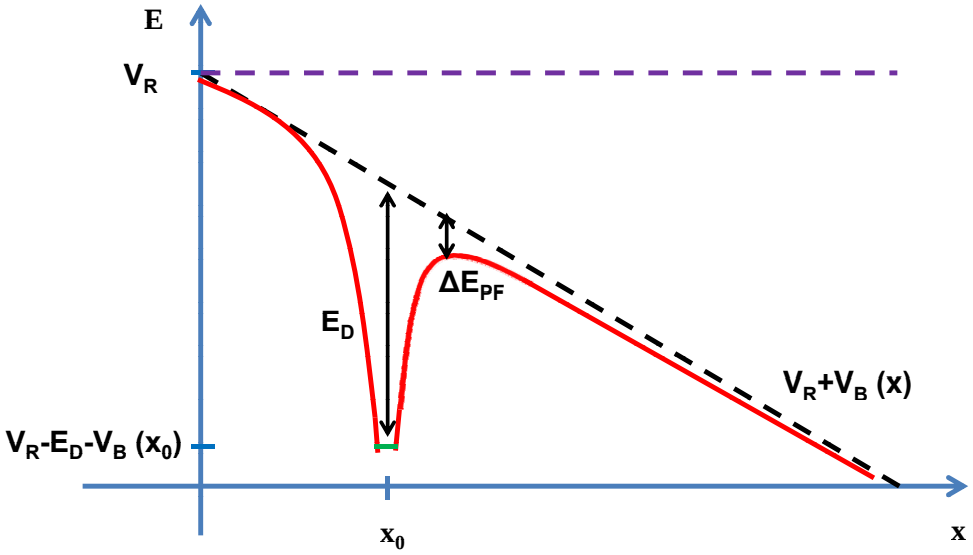

Figure 5.4: Electrostatic potential around a positively charged defect state, under applied bias V_B (a reference potential V_R is also sketched). The Coulomb potential leads to a reduction of the potential barrier for a trapped electron and thus an enhanced emission rate.

function and the Huang Rhys factor, respectively. Also, the R_0 coefficient can be computed as:

$$R_0 = \frac{\pi}{\hbar^2 \omega} \frac{S^{p-1} e^{-S}}{(p-1)!} \left[0.26 \left| V \right|^2 + 0.18 \frac{\left| V\Delta \right|^2}{S} (p-1) \right]. \tag{5.1.19}$$

5.1.4 Field Enhanced Emission

A trapped electron, in a defect state inside the dielectric layer, can also perform a transition that has not yet been discussed: it can reach the CB of the dielectric via thermal emission from the defect state. This process was first observed by Frenkel [142]; he succeeded to explain the increased leakage behavior of insulators at high applied voltages by a field-assisted barrier lowering for the trapped electrons. A schematic of this process can be observed in Figure 5.4. This barrier lowering process can be explained simply by the Coulomb interaction between an electron and the charged defect state inside the dielectric layer.

The barrier-lowering term, as derived by Frenkel, has a value of:

$$\Delta E_{PF} = \sqrt{\frac{e^3 F}{\pi \epsilon_0 \epsilon_{opt}}}. \tag{5.1.20}$$

Since we are considering a reduction of the potential barrier seen by an electron due to the Coulomb interaction, one can observe a resemblance to the thermionic emission (SE) process. This fact becomes more obvious when we inspect the two barrier-lowering terms and conclude that:

$$\Delta E_{PF} = 2\Delta E_{SE}. \tag{5.1.21}$$

The transition rate for a thermally activated electron, trapped in a defect state, to reach the conduction band of the dielectric can be resumed as [143]:

$$T_{PF} = \nu \cdot \exp\left[-\frac{1}{k_B T}\left(E_D - \sqrt{\frac{e^3 F}{\pi \epsilon_0 \epsilon_{opt}}}\right)\right]. \tag{5.1.22}$$

5.2 Trap Relaxation Energy

We have assumed until now that oxygen vacancies play the dominant role, due to the previously reported studies that bring direct physical evidence to support this statement [73, 144]. We should however clarify some properties of the vacancies we have used in our simulation before moving on to the simulation results. Experimental data to characterize vacancies is usually hard to find so one has to rely on ab initio calculation instead. Nevertheless, a very good first principle study on the topic of oxygen vacancies in STO layers has been recently performed by Alexandrov *et al.* [115]. In their work, the structural and electronic properties of both neutral – or so-called F centers – and charged oxygen vacancies – the $F+$ centers – have been analyzed, these two types of oxygen vacancies being the most common for the STO lattice. They rely on a hybrid Hartree-Fock density functional theory (HF-DFT) method using the linear combination of atomic orbital (LCAO) approach.

The most important conclusions and the parameters we have also implemented in our simulations will be discussed below. As already observed for other oxides, vacancies in the lattice will induce some structural distortions due to

Atom	Lattice constant	Coordinates	Displacements for F and F^+	
Ti	$a_0/2$	$0,\ 0,\ \pm a_0/2$	$-0.96a_0$	$2.40a_0$
O	$a_0/\sqrt{2}$	$\pm a_0/2,\ 0,\ \pm a_0/2$	$-1.05a_0$	$-1.57a_0$
		$0,\ \pm a_0/2,\ \pm a_0/2$		
Sr	$a_0/\sqrt{2}$	$\pm a_0/2,\ \pm a_0/2,\ 0$	$0.25a_0$	$0.52a_0$
O	a_0	$\pm a_0,\ 0,\ 0$	$0.37a_0$	$0.49a_0$
		$0,\ \pm a_0,\ 0$		
O	a_0	$0,\ 0,\ \pm a_0$	$0.58a_0$	$-0.36a_0$

Table 5.1: Displacements of atoms due to a neutral (F) or charged (F^+) oxygen vacancy in the STO crystal lattice; positive sign means outward displacement [115].

Vacancy	Energy level	Disperdion
F center	0.8 eV	0.13 eV
F^+ center	1.2 eV	0.05 eV

Table 5.2: Energetic level depth of the different oxygen vacancies inside the STO bandgap, with respect to the CB minima, and the associated dispersion [115].

the electrostatic interaction. The directions of the displacement for neighboring atoms of the STO lattice, in the case of an F center, are schematically shown in Figure 5.5.

As one can observe, the Sr atoms will be pushed outwards while the Ti and O atoms will be pushed inwards. The displacement for this case, as well as the $F+$ center is resumed in Table 5.1. For the positively charged Oxygen vacancy, the situation differs: the Ti atoms are also pushed outwards, together with the Sr atoms.

The calculated values for the position of these vacancies inside the bandgap and the dispersion of these defect bands are given in Table 5.2. What one will observe when analyzing the two tables is that the charged $F+$ center has a much larger impact on the dislocations in the STO lattice as compared to the F center; also the charged vacancies lie deeper in the bandgap, at approx. 1.2 eV from the conduction band minima, as compared to 0.8 for the neutral case.

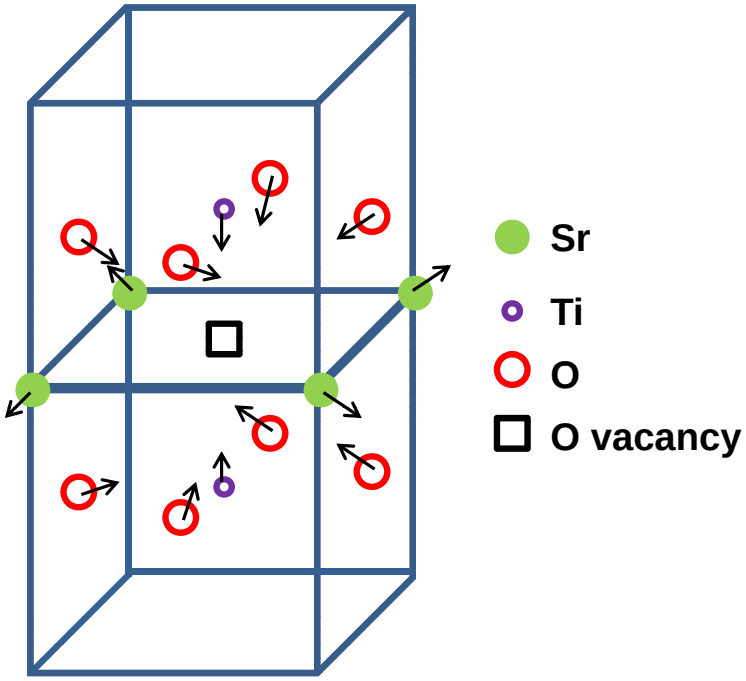

Figure 5.5: An STO lattice cell, with the direction of displacement due to the electrostatic interaction with a neutral *F* center (O vacancy). Fig. redrawn from [115].

Based on this study, we have used very similar values of 0.9 and 1.25 eV from the conduction band minima for the two cases. We can thus take into account also the change in electric charge of the oxygen vacancy, when an electron is trapped. Carrying out a number of simulations, we found out that the dominant trap-assisted tunneling process takes place in the following manner: electrons will most likely tunnel in the positively charged vacancy or defect state. Once occupied, this vacancy will become neutral and change its energy with respect to the conduction band minima. Afterwards, the electron can perform another tunneling process into an unoccupied defect. The so-called relaxation energy, which is the difference between the two possible vacancy states, charged and neutral, or unoccupied and occupied by an electron in other words, can have a significant impact on the behavior of the leakage current since it will affect the phonon-assisted, trap to trap tunneling inside the STO layer; this mechanism was therefore been added to the kMC simulator.

5.3 Field Dependence of the Dielectric Constant

One final physical process, implemented in the simulator, still needs to be discussed. Electric measurements of our STO samples reveal a dependence of the dielectric permittivity with the applied electric field. Figure 5.6 shows the measured data for a 10 nm thin STO sample. Since this behavior could have an impact on the electrostatic interactions inside the MIM structure, or on the image forces near the electrodes, this peculiarity has also been implemented in the simulation algorithm.

Nevertheless, let us spend also some more words on this interesting effect. Although puzzling at first sight, this effect can be easily explained. Fuchs *et al.* [145] perform a detailed characterization of the dielectric properties for STO films; they report the same electric field dependence for the epsilon value we observe. For such cubic perovskite structures the explicit relation between epsilon and the electric field can be formulated as [146]:

$$\epsilon(E) = \frac{\epsilon_0}{[1 + (E/E_0)^2]^{1/3}}. \tag{5.3.1}$$

The meaning of this parameter and its relationship to the paraelectric phase of the dielectric can be found again in [145]. As a remark, this dependency of the dielectric constant makes perovskite materials also very appealing for microwave applications, since a tunable phase-shifter can be very easily implemented with these materials.

5.4 Numerical Implementation

In the previous sections, a brief introduction into kMC techniques has been presented and all the possible leakage channels through our MIM structures have been described. In this section, we will give an overview of how the kMC simulations are carried out, with a basic structure of the simulation code employed. However, due to space limitations and to the fact that we cannot assume advanced programming skills for every reader, we will not discuss into detail the simulation code.

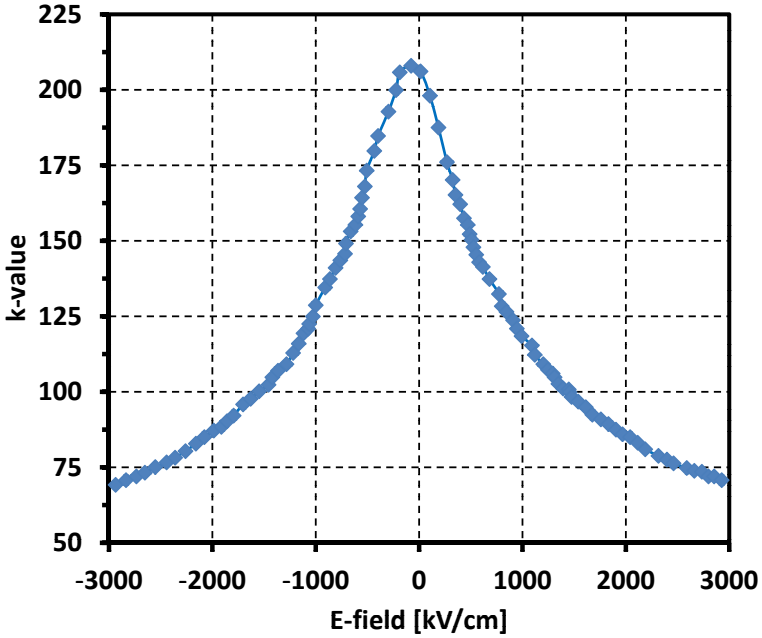

Figure 5.6: Measured dielectric permittivity of our 10 nm thin STO capacitors under applied electric field (taken from [147]).

The simulation code is written in the $C++$ programming language and uses the deal II library [148] for scientific computations. The functions and classes defined inside this library all rely on finite elements as a tool to solve the desired electrical, physical, mechanical or chemical problems. We will give a short description on how the desired MIM geometry is generated using the deal II library and show how a part of the code is implemented, namely computing the Poisson equation, a step that is performed after each incrementation of the bias voltage. This piece of the code should offer insights about the basic structure, steps that have to be performed and class and functions needed in generally all applications that make use of finite element methods for e.g. solving electrical problems.

In Figure 5.7 one can observe the main building blocks of a typical deal II program, blocks that will be used also for our implementation of the Poisson solver. Let us shortly comment on the functionality of each block:

Triangulation: a triangulation contains all cells of a modeled geometry and the boundary elements; cells are representations of the unit cell (hypercube) under the appropriate mapping in the deal II library. The triangulation thus stores information about the topology of the mesh, it knows how many vertices,

lines and faces a cell has (the number obviously depends on the cell dimension) and how cells are connected to each other. No information is stored in the triangulation – also referred to as mesh – about the finite elements one might use or even about the shape of the cells – this is the role of the mapping functions as we will see below.

Finite Element: depending on the finite element class, they will store the properties of the finite element space, such as degrees of freedom for the vertices, lines or cells of the triangulation, gradients and values for shape functions. Finite elements are again defined on the unit cell with the corresponding dimensionality.

Quadrature: quadrature elements are used for the numerical integration of quantities. They contain the position of quadrature points and the corresponding weights, as defined on the unit cell. A large variety of quadrature elements is available in the deal II library, that covers 1D, 2D or 3D elements with various levels of accuracy for the numerical integration.

DoFHandler: the Degrees of freedom (DoF) handler associates the finite elements to the triangulation elements (triangulation elements can be either vertices, lines, faces, cells or any combination of them). It also gives them a global iteration number; most operations that deal with triangulation and finite elements use DoF handlers and derived classes and functions.

Mapping: the quadrature points, the shape functions and the degrees of freedom of the finite elements are all defined on the unit cell, as already mentioned. In order to assemble our system, usually composed of a matrix and right hand side, we need to map all the above mentioned functions, points and elements from the unit cell on the real cells of the triangulation.

FEValues: the actual values of the shape functions in every point of the quadrature, applied on the real cell, can now be evaluated and stored in this class and derived members thereof.

Linear Systems: having calculated the FEvalues and with the help of the DoFHandlers, one can already build up the linear system that needs to be solved. The problem to be solved is usually brought in the bilinear form and

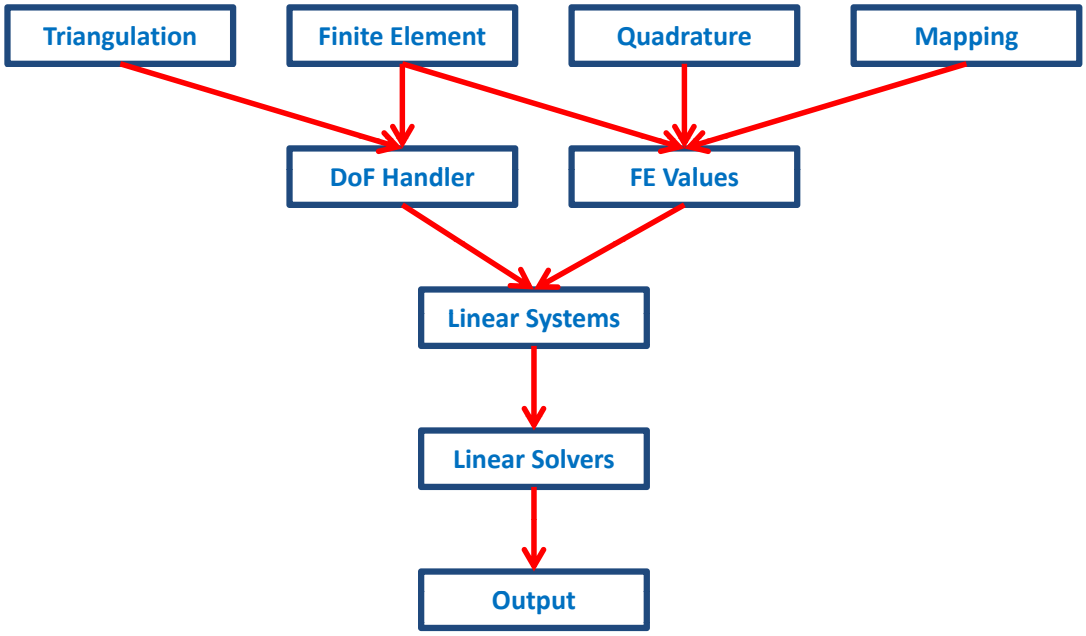

Figure 5.7: Building blocks of a finite element program, needed to compute the electrostatic potential inside the dielectric layer - since the transition rates of the kMC algorithm are field-dependent.

various classes and functions are used to manipulate and store matrix or vector elements.

Linear Solvers: the last step of a finite element program, after the system has been assembled, using the appropriate triangulation, finite elements, etc. is to actually solve the linear system. A variety of solvers, ranging from iterative solvers, preconditioned iterative solvers to direct or sparse solvers are available within the deal II library pack.

Output: a post processing step; after the system has been solved, the results are formatted in different output formats, which can later be opened and analyzed in open source or commercial visualization tools.

Let us now proceed and treat the Poisson equation and its finite element implementation in more detail. If we recall some basic electromagnetic theory, the Poisson equation – with zero boundary conditions, for simplicity in this example – can be written as:

$$\begin{aligned} \Delta\phi &= f \qquad \text{in } \Omega, \\ \phi &= 0 \qquad \text{on } \partial\Omega. \end{aligned} \tag{5.4.1}$$

For simplicity again, we will assume the right hand side constant, $f(x) = 1$, and we will calculate the problem only in the unit cell, in two dimensions, or in other words for $\Omega = [0,1]^2$. We will nevertheless come back on these simplifications after the main procedure for solving the Poisson equation within the deal II framework will be sketched. We can rewrite our equation in the weak form, multiplying it with the test function ψ and integrating it over the definition domain:

$$\int_\Omega \psi\Delta\phi = \int_\Omega \psi f \tag{5.4.2}$$

or after some algebraic manipulations:

$$\int_\Omega \nabla\psi \cdot \nabla\phi - \int_{\partial\Omega} \psi\mathbf{n} \cdot \nabla\phi = \int_\Omega \psi f. \tag{5.4.3}$$

The test function has to fulfill the same boundary conditions as our potential ϕ, so we can conclude that the weak form for the Poisson equation is:

$$\int_\Omega \nabla\psi \cdot \nabla\phi = \int_\Omega \psi f. \tag{5.4.4}$$

Our problem thus reduces to finding the function ϕ for which the above statement is true, for every test function ψ with appropriate characteristics (e.g. boundary conditions). Finding such a function is in general impossible, but there are some tricks that can help us. One can search instead for an approximate function $\phi_h(\mathbf{x}) = \sum_j \Phi_j \psi_j(\mathbf{x})$, where Φ_j are the expansion coefficients we need to determine and $\psi_j(\mathbf{x})$ are the finite element shape functions.

We have already mentioned the necessary elements needed to define these shape functions ψ_i: the triangulation, quadrature and mapping. Additionally we need the class of finite elements – the simplest choice in 2D would be the Lagrange elements of first degree or bilinear elements. In this case, the shape functions would be simply defined by interpolation on support points. We can now

rewrite the weak form of the Poisson equation, using now the shape functions and expansion coefficients:

$$\int_\Omega \nabla\psi_i \cdot \nabla\phi_h = \int_\Omega \psi_i f \tag{5.4.5}$$

or using the matrix form for the linear system:

$$A\Phi = F \tag{5.4.6}$$

Where A and F are defined as:

$$\begin{aligned} A_{ij} &= \int_\Omega \nabla\psi_i \cdot \nabla\psi_j \\ F_i &= \int_\Omega \psi_i f \end{aligned} \tag{5.4.7}$$

Thus, the matrix entries A_{ij} and the right hand side elements F_i need to be computed, in order to solve our electrostatic problem. Some remarks on the calculation of these entries: both the calculation of matrix elements and of RHS elements involves integration over the entire simulation domain. In order to numerically perform these integrations, one usually splits the integrals as sums over all cells of the triangulation and then uses some quadrature rule to numerically integrate the functions. In other words:

$$\begin{aligned} A_{ij} &= \sum_{K=1}^{N} \int_K \nabla\psi_i \cdot \nabla\psi_j \\ F_i &= \sum_{K=1}^{N} \int_K \psi_i f \end{aligned} \tag{5.4.8}$$

where N is the total number of triangulation cells K. Using a quadrature rule, we finally obtain for each cell a contribution to the integral of:

$$\begin{aligned} A_{ij}^K &= \int_K \nabla\psi_i \cdot \nabla\psi_j \approx \sum_q \nabla\psi_i(\mathbf{x}_q^K) \cdot \nabla\psi_j(\mathbf{x}_q^K) w_q^K \\ F_i^K &= \int_K \psi_i f \approx \sum_q \psi_i(\mathbf{x}_q^K) f(\mathbf{x}_q^K) w_q^K \end{aligned} \tag{5.4.9}$$

where $\mathbf{x}_q^K$ is the q^{th} quadrature point on cell K, and w_q^K the q^{th} quadrature weight. In our case, if Lagrange elements are to be used for the shape functions, a simple Gauss quatrature element is sufficient to perform the numerical integration with enough accuracy.

We stress again at this point that the FEValues class and its member elements are essential to the assembly of system, since they bring together the finite elements shape functions – which are continuous functions defined in the unit cell – with the mapping functions – that translate the elements onto the real cells – and with the quadrature elements – needed for the numerical approximation of the space integrals.

A few details on the actual implementation for this part of the simulation code: data encapsulation is used for many of the functions and members objects, which means that they are mostly defined as private – in fact the only public function is the run function. As described above, the main objects – implemented dimension independent with the help of templates – are of type Triangulation<dim>, FE_Q<dim> and DoFHandler<dim> (implicit, standard mapping functions are used). Also some matrix and vector elements are used, to perform the algebraic manipulations; they are needed in order to handle the sparsity pattern matrix, system matrix, right hand side vector and solution vector.

Some functions are used in order to implement the above described Poisson equation in a computer algorithm. The structure used is actually a general one, common for many finite element implementations of various physical problems. We definitely need for our code the following functions:

make_grid(): a typical preprocessing function, it creates the desired geometry and stores the triangulation object. It can read external files – this is how we actually define our MIM structure when simulating the leakage through the STO layer; also different boundary conditions can be declared here,

setup_system(): all objects and function members that will be needed are defined here. The desired finite elements are chosen, also the quadrature and mapping functions. The DoFHandler is initialized and memory is preallocated for all data structures.

assemble_system(): the system matrix and right hand side entries are computed by this function.

solve(): the linear system is solved by this function. Various preconditioning steps and solver properties are also defined here. The solution vector is stored for further processing.

output_results(): this last function can be seen as a postprocessing step. The solution vector is formatted for visualization in different third-party programs. Also derived quantities can be computed from the solution vector and stored.

This core structure is used for our kMC code to obtain the results shown in the next section. Due to space limitations and complexity issues, not all the simulation code can be discussed. We can however sketch the whole picture and give a few more details. The geometry, mesh and boundary values are all implemented using the procedure described above. An initial solution is calculated at zero bias voltage. Then defect states are randomly distributed across the modeled geometry, with properties like energy depth, charge state, relaxation energy. Beside the above described Poisson solver, the kMC code has two other main "blocks" that will be used. In the second block, the whole physical mechanisms deduced in the previous section are implemented. Field dependent transition rates are calculated for all possible processes that can take place inside the modeled MIM capacitor, including electron injection from the electrode into defect states, direct tunneling, trap-to-trap tunneling of electrons already in the dielectric, and so on. The third block contains the implementation of the stochastic procedure – the kinetic Monte Carlo algorithm. This code section chooses, after generating the random numbers and some other algebraic steps, which transition to execute from all the possible ones and with what value to increment the simulation time. After the transition is performed, the Poisson solver is called again, since e.g. a TAT transition in a defect state will change the charge distribution inside the dielectric film and thus the right hand side of the linear system. In this way, the electrostatic interactions can be computed self-consistently inside the simulator. The whole process is repeated at various voltages and the steady state current is recorded at these bias points until a whole IV characteristic is performed.

We can now observe some advantages of the code implementation described earlier. Since each computational step is performed by a different function, after each transition only the *assemble_system* and *solve* functions need to be recomputed, since the charge distribution is now different. Computational time and resources are thus saved.

5.5 Sensitivity Analysis

The best agreement between measured curves and simulation results is shown in Figure 5.8. We can observe a good voltage and temperature scaling of the simulated leakage current for the whole voltage range and over a 110 K temperature interval. The most important parameters for our kMC simulations are: the defect density inside the dielectric film, the depth of the defect level inside the bangap, the relaxation energy and the Shottky barrier between the SRO electrode and the STO film; they are given in Table 5.3 and will be discussed below.

Regarding the choice of the defect density, Pawlak *et al.* [73] report an oxygen vacancy density as high as 10^{13} cm^{-2} in the vicinity of the injecting electrode. In Ref. [122], Jeon *et al.* study the SRO/STO interface in the presence of oxygen vacancies. Their conclusion is that oxygen vacancies strongly lower the Schottky barrier at the interface, a first principle study resulting in a 1.15 eV barrier for the SRO/STO interface. However, Jeon *et al.* expect even lower values for the Schottky barrier in real materials, especially at high vacancy densities; since we think that this is the case for our samples, we consider the value of 1 eV as realistic. The values used in our simulations for the energy of the defect level inside the STO film and the relaxation energy are, as already mentioned, almost identical to the values reported by Alexandrov *et al.* in their first principles study: 0.8 eV, with 0.4 eV the difference between the charged and uncharged state. We therefore consider that our input parameters for the kMC simulation are physical and the obtained fit can confirm this assumption.

In Figure 5.9, the same leakage curves as in Figure 5.8, at different temperatures, are shown. Beside the total current – marked with a continuous line – also the different components that add up to this current are shown. Since the trajectory of each injected electron, as it travels between the two electrodes, is tracked by our simulator, we can also determine the impact of the different

Parameter	STO
Bandgap E_g	3.2 eV
Electron affinity	4 eV
Trap concentration N_T	$1.7 \cdot 10^{19}$ cm^{-3}
Trap depth E_T	0.9 eV
Relaxation energy E_R	0.35 eV
Conduction band offset CBO	1 eV

Table 5.3: Most important simulation parameters for the kMC simulations [84–86, 115, 122].

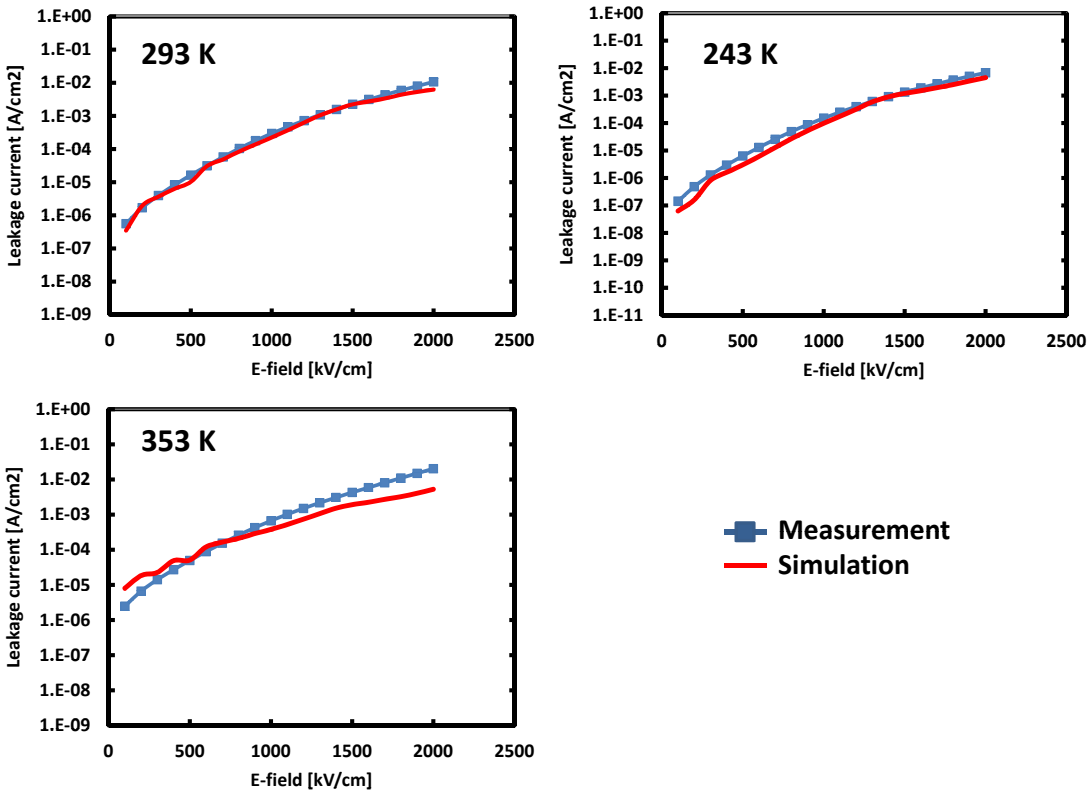

Figure 5.8: Measurement vs. simulation plots, for the best simulation fit obtained over the 110 K temperature interval (taken from [147]).

leakage mechanisms on the total result. We can observe that for all temperatures the trap-assisted tunneling is the dominant leakage mechanism, a finding that can be attributed to the large number of trap states inside the dielectric. The "direct tunneling" mechanism is the second-important leakage channel, but only has an increased value at higher temperatures (the direct/FN tunneling and

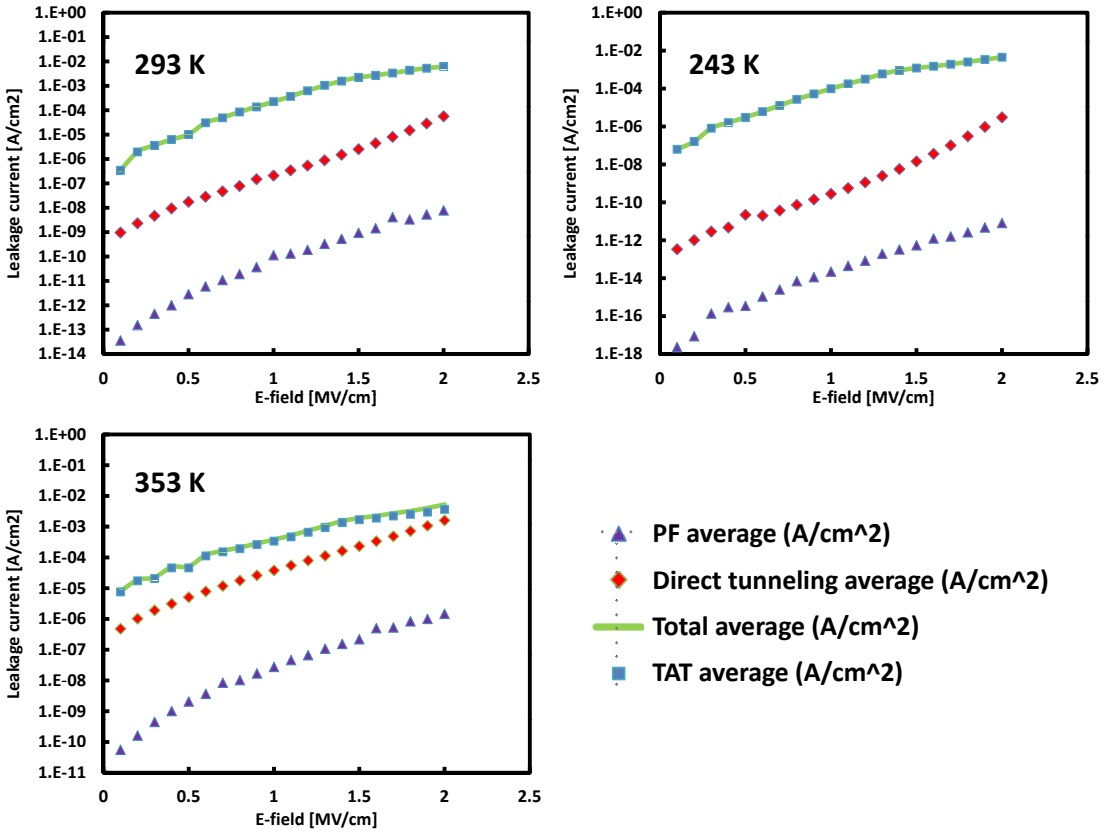

Figure 5.9: Simulated I-V-T behavior for the STO samples; total leakage current and its various components are shown (taken from [147]).

Schottky emission are all depicted in the "direct tunneling" component, since they are treated in a unified framework, see [38] for details). A PF-emission of the trapped charge carriers in the CB of the dielectric is unlikely due to the relatively large depth of these vacancies; also the PF emission channel is in tight competition with the TAT process, since both mechanism need electrons that tunnel from the electrode in defect states inside the dielectric film. It is obvious that both processes cannot have a dominant role at the same time and since for this choice of input parameters the trap-assisted tunneling seems to have the highest probability, the PF process is not surprisingly the less used leakage channel.

To better understand the role of the trap states in the conduction mechanism, some simulations are performed without any defects in the simulation volume; the obtained results are shown in Figure 5.10. Since no defects are present, the calculated leakage current is the intrinsic one, caused only by the direct/FN tunneling and the Shottky emission – especially at high temperatures. The most

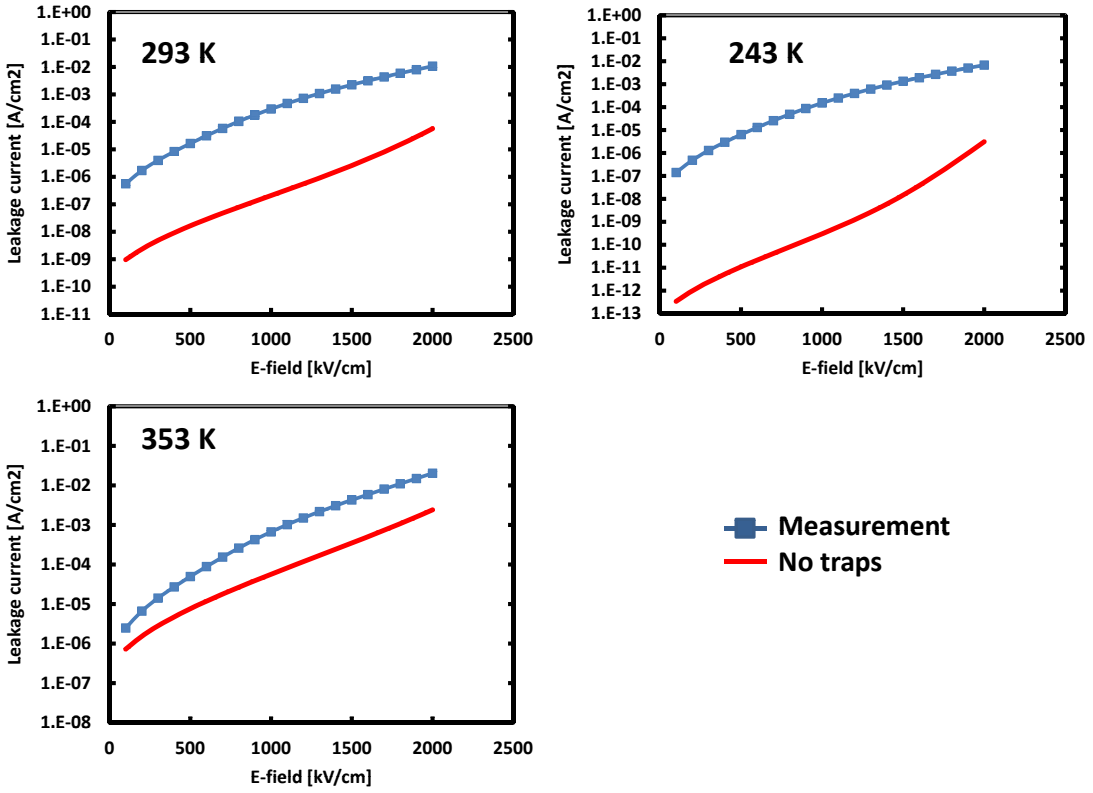

Figure 5.10: Simulated I-V characteristic for the measured sample, with no defect states inside the bandgap (taken from [147]).

relevant parameters for this leakage mechanism are thus the value of the CBO at the SRO/STO interface and the sample thickness. Again, from the same figure one can notice the pronounced temperature and field dependence of this channel. If at low temperatures the resulting current is several orders of magnitude smaller than our measured one, at high temperatures the misfit is of only one order of magnitude; over the whole simulated temperature and voltage range this process spans over more than 9 orders of magnitude.

Another interesting fact can be observed at a closer inspection of Figure 5.9 and Figure 5.10 – namely that the kMC algorithm indeed takes into account all possible leakage channels and thus the total current is a result of these competing processes. In Figure 5.9 one can observe that the "direct tunneling" component has a strong temperature dependence, being about 4 orders of magnitude lower at 243 K than the dominant "TAT" component. At room temperature, it is almost 2 orders of magnitude lower than the "TAT" component, which again determines the value of the total current. At higher temperature however, the

"direct tunneling" component is in the same order of magnitude as the "TAT" one. When no defects are present, as already mentioned, the leakage is due to the intrinsic mechanism of tunneling through or over the potential barrier at the SRO/STO interface. At low and room temperature one can notice that the curves in Figure 5.10 are identical to the "direct tunneling" component in Figure 5.9 because the intrinsic component is so small compared to the TAT that these two mechanisms don't interact at all. Even though our sample is relatively thin and the intrinsic leakage mechanisms have a high probability of being "picked" during our stochastic procedure, these channels have only a limited contribution to the total current – less than 1 percent at room temperature. At high temperature however, the total leakage current in the "no traps" simulation is slightly higher than the "direct tunneling" component in Figure 5.9. This fact can be explained in the following way: since the intrinsic channel is in the same order of magnitude as the extrinsic one – the trap-assisted tunneling – the two dominant mechanisms will interact. In the presence of defect states, the electrons will prefer the TAT process, so fewer will use the "direct tunneling" process; when no defects are available however, all available charge carriers will use the intrinsic channel at high temperature. This observation clearly shows that our simulator does not simply compute components of the leakage current caused by different mechanisms and then simply adds them to a total current; the total leakage is dynamically computed based on the available transport channels and also detects the dominant one.

The next analysis that we perform is intended to clarify the importance of the spatial distribution for the defects inside the STO layer. Pawlak *et al.* assume that a higher concentration should be present near the injecting electrode in order to obtain such high leakage currents. Our simulation results however, do not support this assumption. In Figure 5.11, we can observe the modeled structure with some key parameters like thickness of the STO layer, workfunction of the electrode or bandgap and electron affinity of the dielectric. We can also observe some symbolic defect states, represented by circles inside the dielectric layer and three different regions, separated by red dotted lines. In the following we will perform 3 more simulation sets, allowing defect states only in these specific regions of the dielectric film.

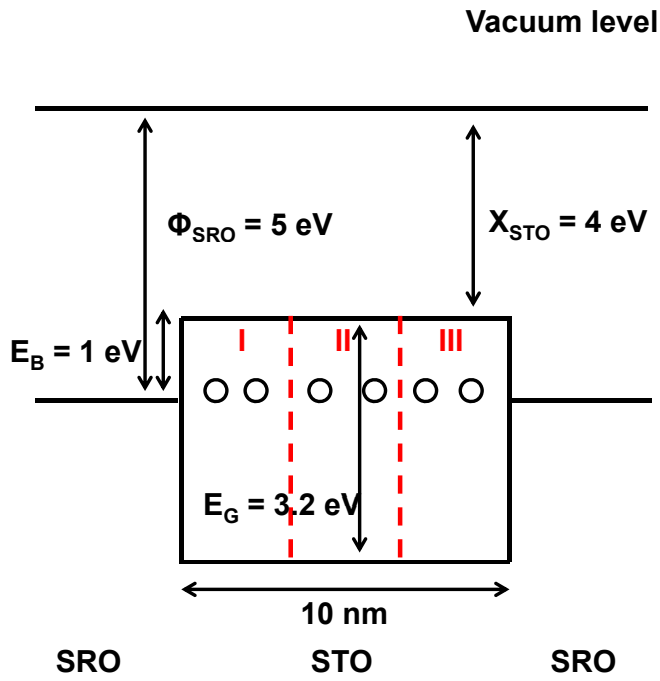

Figure 5.11: Schematic of the modeled STO samples, with different regions highlighted, in order to analyze the impact of different defect positions on the leakage behavior.

We allow defects in the first 3 nm of the STO layer – results denoted with "injecting electrode" – in the middle section of the dielectric – from 3.5 to 6.5 nm – and finally only on the last 3 nm – denoted "extracting electrode". In Figure 5.12 we can observe again the best obtained agreement between simulation and measurement but also the results of the three different simulation sets. We see that the defect states in the middle of the STO layer have the largest impact on the leakage behavior; when no trap states are allowed in that region, the curves "injecting" and "extracting" overlap and are identical to the "no traps" curves. Analyzing also the different leakage components for the three presented cases (not shown), confirms us that for the "injecting" and "extracting" cases, the intrinsic tunneling component is the dominant mechanism. While for the "injecting" case, a TAT component, 3 to 4 orders of magnitude lower than the direct tunneling component, is still computed suggesting that an injection process from the electrode into a nearby trap, followed by a tunneling process from the trap into the opposite electrode is unlikely but can still happen, for the "extracting" case only the direct tunneling component is different from zero. This demonstrates that a tunneling process into a trap situated at more than 6

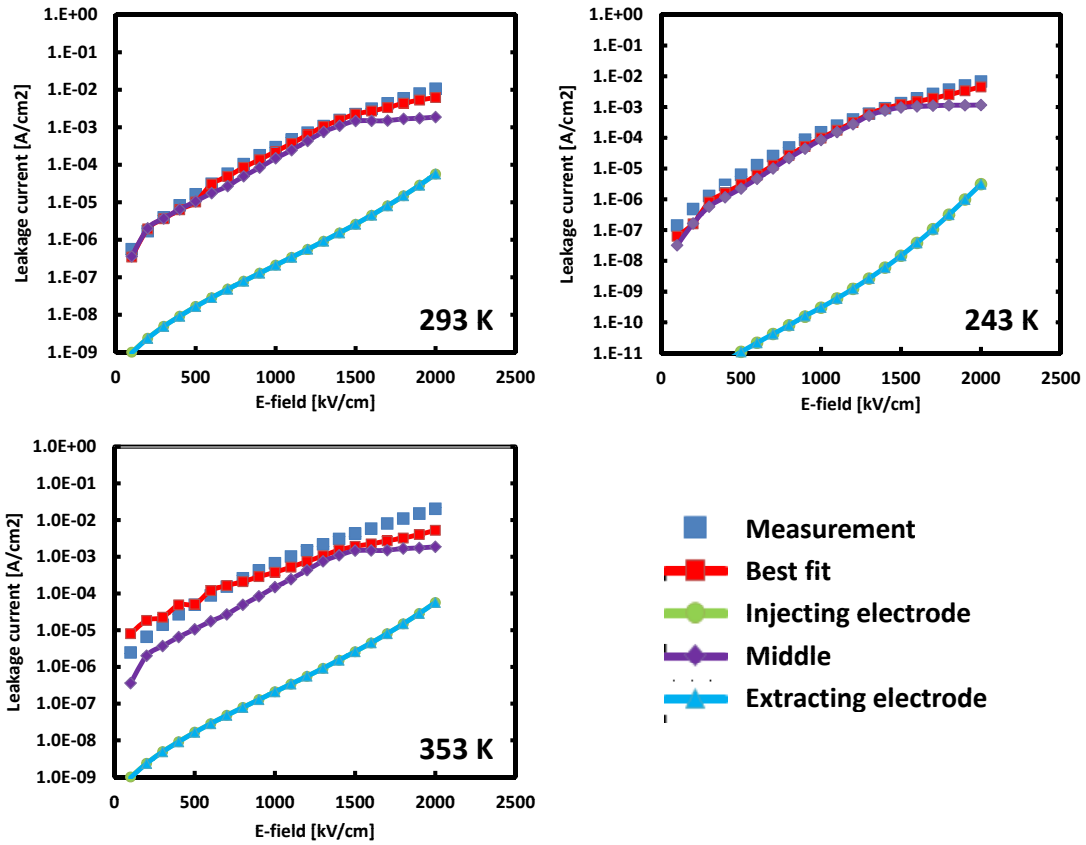

Figure 5.12: Simulated leakage current at different temperatures for various trap positions: either near the injecting electrode (region I in Figure 5.11), in the middle of the dielectric layer or near the collecting electrode(regions II and III in the same Figure), taken from [147].

nm away from the electrode, followed by a subsequent tunneling process into the opposite electrode is basically impossible.

We can conclude that the average tunneling length is around 3 nm and the defect states in the middle of the dielectric have the highest occupation probability. If no defects are present in the middle section, the extrinsic TAT process cannot take place and the leakage is dominated only by the intrinsic tunneling. We can therefore conclude that a typical hopping process needs at least two trapping sites and that a charge carrier cannot tunnel more than 3-4 nm between two defects.

Also interesting to observe is the effect of an increased CBO at the SRO/STO interface. This increase could be obtained experimentally by introducing an interface dipole, e.g. through doping or by changing the material of the injecting

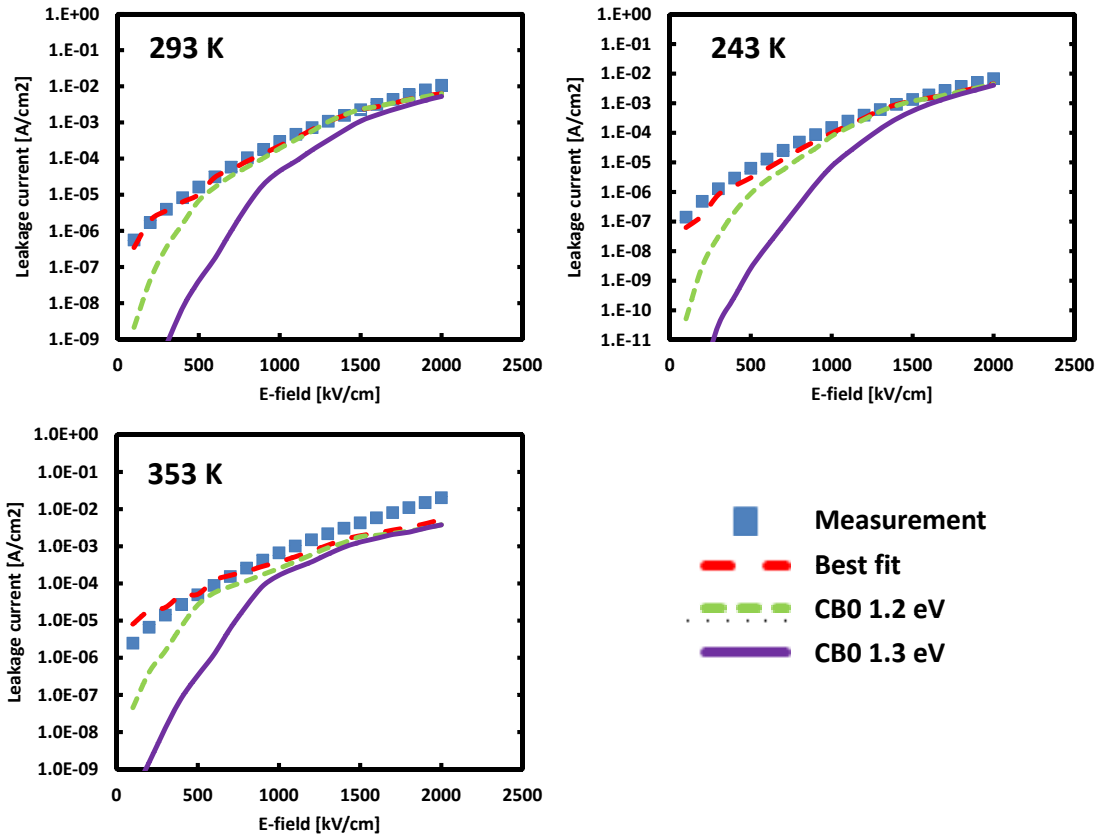

Figure 5.13: Influence of the potential barrier at the injecting electrode on the leakage current; different conduction band offsets (CBOs) have been analyzed (taken from [147]).

electrode. As one can observe in Figure 5.13, even a 0.3 eV increase of the CBO is not enough to reduce the leakage sufficiently. While both curves start at a significantly lower current value for small electric fields, the situation changes as soon as the electric field increases. For the 0.2 eV increased conduction band offset, the leakage curve overlaps with the standard case already at 500 kV/cm; for the 0.3 eV increased barrier this only happens above 1500kV/cm, but still the leakage is unacceptable high from about 1000 kV/cm.

If we recall the implemented physical processes that can lead to the undesired leakage for our samples, all described in the first part of this chapter, we can also find a reasonable explanation for this behavior. Increasing the Schottky barrier at the SRO/STO will indeed reduce the tunneling probability – for an electron tunneling across the whole dielectric as well as for an electron tunneling from the electrode into a trap state nearby. But since the tunneling is modeled in our

calculations as a field assisted process and the defect concentration is pretty high – which translates into small electrode-defect and defect-defect distances – the effect of the increased CBO will be marginal at higher electric fields. Starting with moderate bias voltages, the electrode-trap tunneling rate will increase dramatically and the defects close to the electrode will be occupied virtually all the time. Once the electrons are injected into the first defects, the classical trap-assisted tunneling leakage process can take place, the overlapping curves at higher fields confirming this theory.

On the other hand, the increased CBO will definitely affect the direct tunneling and Shottky emission, since the height of the potential barrier is crucial for an electron that tunnels across the whole dielectric layer or hops over the Schottky barrier. Analyzing the different components of the leakage current for the increased CBO cases (not shown in Figure 5.13) we can confirm that the "direct tunneling" component is shifted downwards due to the larger barrier. Since all possible channels compete in the kMC framework, it is no surprise that for this 2 cases the PF emission increases considerably (2 to 3 orders of magnitude) as compared with the standard case, becoming the second most-important leakage mechanism for this analyzed configuration.

Finally, a last case is treated, namely the influence of a $GdAlO_3$ (GAO) interlayer in the SRO/STO/SRO stack. The idea is suggested by Menou *et al.* [149] in an attempt to reduce the leakage through a 10 nm thin STO MIM capacitor. This technique, of inserting an interlayer in a high-*k* MIM structure, is already known in the DRAM industry, the most prominent example maybe being the incorporation of the Al_2O_3 layer between ZrO_2 layers. This so-called ZAZ films achieve remarkable performance in terms of EOT and leakage current and are currently manufactured by several DRAM producers. The idea behind this stacked high-*k* devices is that an appropriate interlayer would block the formation of grain boundaries and associated defects in the high-*k* film, improving thus the performance. But finding such an interlayer material is not a trivial task, it has to fulfill some criteria if a performance increase is desired: to retain its insulating properties, the interlayer – usually a metal oxide – must have a high enough crystallization temperature so that it can remain amorphous during processing. It also must not influence the crystallization temperature of the high-*k* dielectric nor intermix with it. Finally, it must have a high enough dielectric permittivity

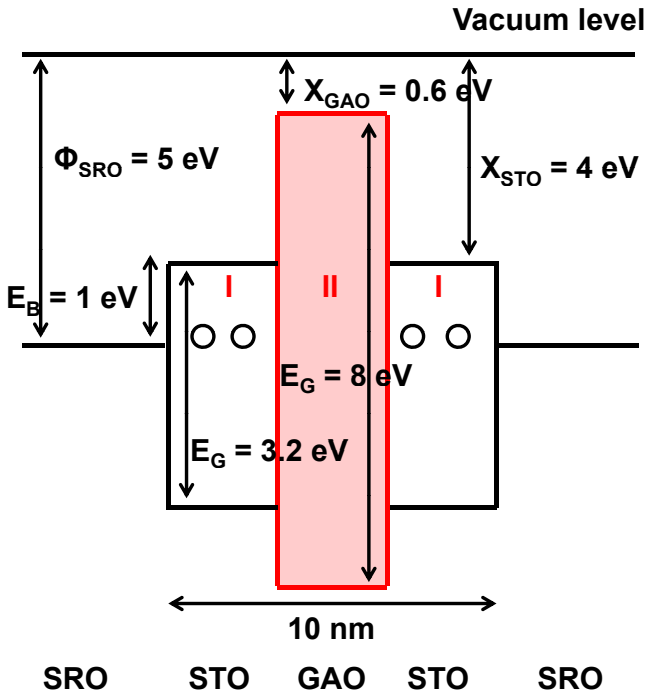

Figure 5.14: Schematic of the stacked capacitor structure, analyzed in order to reduce the unwanted leakage current.

so that it will not reduce the overall dielectric performance of the stack. The GAO metal oxide fulfills all this requirements; details can be found in [149] by the interested reader.

The proposed structure is presented in Figure 5.14: the GAO layer, depicted reddish, should be lattice matched to the STO layers and have a larger bangap of around 8 eV compared to the 3.2 eV for STO. The obtained experimental results are promising and we want to clarify the reason of this improvement; we thereby model the same structure in our kMC framework. Simulations are again performed for the stack structure at different temperatures. The simulated leakage currents at room temperature are shown in Figure 5.15 for two different interlayer thicknesses. Indeed a reduction is obtained, but having in mind the results of Figure 5.12 about the impact of the trap position on the leakage, the explanation is straightforward. We have assumed no defects in the GAO layer since Menou *et al.* choose this metal oxide precisely because of its high thermal stability, large k value and low intermixing probability during fabrication.

Analyzing the two curves for various interlayer thickness and the leakage components thereof (not shown in Figure 5.15) we can conclude: the 3 nm thick,

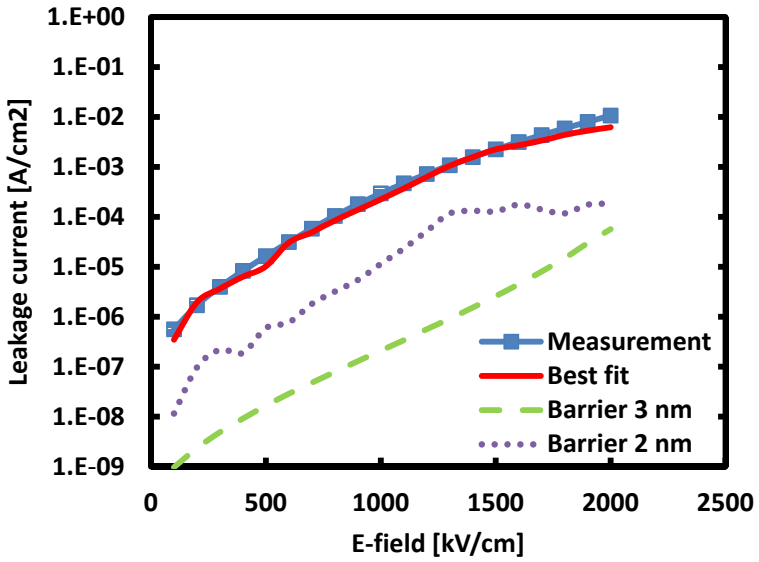

Figure 5.15: Obtained simulation results when inserting a defect-free GAO layer in our MIM structure; the current decrease makes such a stacked capacitor suitable for industry applications (taken from [147]).

defect-free GAO interlayer in the middle of the sample stops any defect-assisted percolating paths between electrodes and thus suppresses TAT. We have already seen that for a TAT process at least two defect states are needed, situated towards the middle of the dielectric layer, since the average tunneling distance is about 3 nm. The dominant transport mechanism in this case is the intrinsic tunneling/Schottky emission, but we can also observe another interesting effect. Since the thick interlayer blocks any trap-to-trap tunneling across it, the PF emission channel records a serious increase. It is not surprising, since all the defect states near the injecting electrode have a high occupation probability; once an electron occupies such a defect state, since tunneling across the GAO barrier is virtually impossible, it still can by emitted in the CB of the dielectric an thus reach the opposite electrode. Still this multi-step leakage channel is at least two orders of magnitude smaller than the direct tunneling component.

For the 2 nm GAO layer, the situation is different. We can note that the extrinsic leakage channel is again becoming the dominant one, but the total current is still more than one order of magnitude lower than without the interlayer. Also the direct tunneling component is not as negligible as in the standard case, this leakage channel profiting from the somewhat reduced probability of the TAT process over the GAO layer. On the other hand, since a trap-to-trap tunneling

across the interlayer is now possible, the PF emission rate has again dropped. As already explained above, since the TAT and the PF mechanism are both competing and use the same defect states inside the bandgap (at least for the first part of the PF process), we cannot have the case where both channels have a dominant impact at the same time.

5.6 Discussion

In this chapter we have analyzed the leakage mechanism through a fabricated SRO/STO/SRO high-*k* dielectric capacitor with the help of an in-house developed kMC simulator. Different physical mechanisms are implemented into the simulation framework and all these channels can compete and contribute to the total leakage current. Several simulation experiments allow us to identify the dominant leakage process through the dielectric film, namely: trap-assisted tunneling with an average tunneling length of 3-4 nm. We can duplicate the measured leakage data over a large temperature and voltage interval; our simulations also allow us to draw conclusions the several improvement strategies.

Of course, reducing the concentration of defects will significantly improve the performance of the dielectric layer under study. If no trap states would be present, the STO film would in fact fulfill the DRAM requirements for a maximum allowed leakage current, which should be smaller than 10^{-7} A/cm^2 @ 1 V. Increasing the CBO, by doping or by changing the material for the electrode, will not significantly improve the performance, due to the large defect states concentration and the fact that the tunneling process is field assisted; at higher electric fields an unacceptable current will still flow. Nevertheless, a defect-free interlayer will suppress the TAT process, since defects in the middle region of the dielectric layer are essential for the defect-assisted process.

Our study thus suggests that if a defect-free fabrication method for STO cannot be implemented or is to complex (expensive), an appropriate multilayer structure will reduce the leakage current values, making the SRO/STO/SRO material system suited for DRAM applications.

6 Applications of the kMC Framework for Organic Solar Cells

To show further applications of our kMC framework, the modeling and simulation of various organic solar cells is presented below. We thus underline that our developed stochastic framework is also flexible enough, allowing us to examine and better understand a wide range of electronic and optoelectronic devices. The excellent agreement between measurements and simulations - as will be shown below - are a standing proof that such stochastic approaches could, in the near future, take the place of established drift-diffusion simulators for a variety of electronic devices, delivering unique insights and information on the physical processes of importance.

6.1 Background

Since they were first reported in 1995 by Yu *et al.* [150], polymer solar cells have been the focus of intense research activity. The typical applications could be covering large area roof tops, greenhouses or large windows in office buildings. Due to their unique features, such as high mechanical flexibility and low weight, also unconventional applications can be imagined: smart clothing or mobile power units for consumer electronics. Although currently cell efficiencies for organic solar cells (OSCs) are not comparable with the mature silicon or gallium-arsenide technology, recent studies [151] have shown that lower efficiencies - between 5% and 10% - and shorter lifetimes of 5 to 10 years can be successfully compensated with low production cost. Various printing techniques, spray- or spincoating methods have been reported over the last years, all being characterized by low cost, high throughput and low temperature processes [152]. It is thus predicted that the threshold of 1/W [151, 152] of electricity will be reached

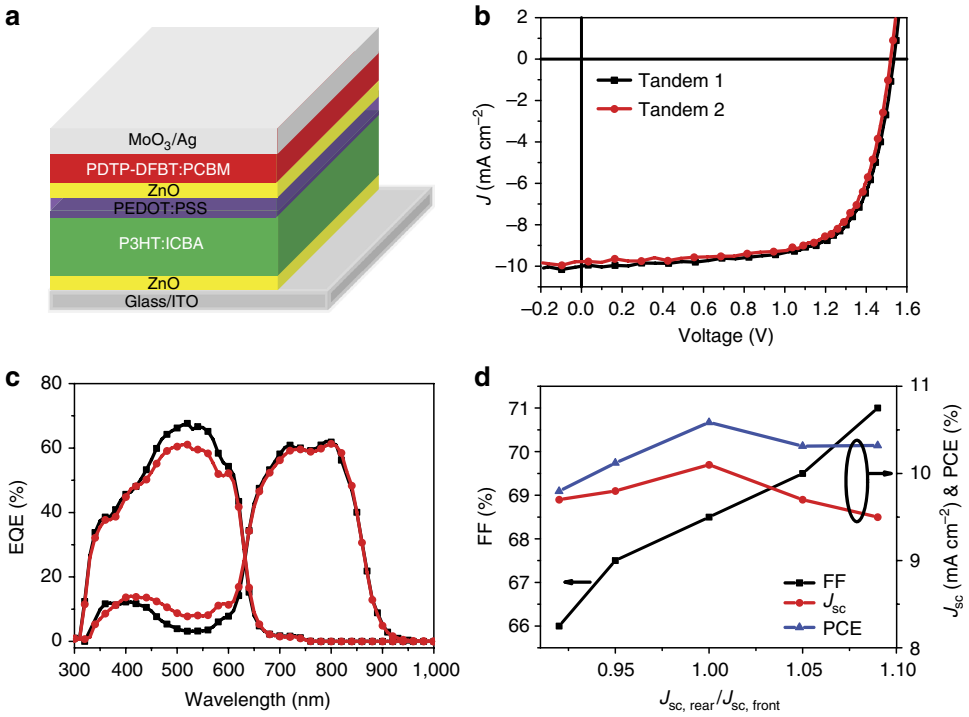

Figure 6.1: (a) Structure of the record tandem cell. (b) Measured J-V characteristic of the tandem solar cell with PC_61BM (tandem 1) and PC_71BM (tandem2). (c) EQE of the two OSCs. (d) Fill-factor and short-circuit current vs. rear and front cell current ratio. Taken from [157]

and expectations are that prices will even be significantly lower, making OSCs a viable and attractive economical option.

High efficiencies, exceeding 5%, have been presented by several groups. Chen *et al.* [153] reported an open circuit voltage as high as 0.76 V and a cell efficiency of 6.77% using a PBDTTT-PCBM system. Liang *et al.* [154] proved that more than 7.4% can be obtained by using PTB7 as donor polymer, while Chu *et al.* [155] reached almost the same performance - 7.3% - with PDTSTPD in the bulk heterojunction (BHJ) blend. Fluorinated P3HT can reach efficiencies of more than 7% as demonstrated by Zhou *et al.* [156] and finally You *et al.* [157] have demonstrated an efficiency exceeding 10% with their tandem organic solar cell. The key figures of merit for this OSC are shown in Figure 6.1.

Classical P3HT-PCBM bulk heterojunctions have also steadily improved, showing a figure of merit (η) of around 5% as in the studies of Irwin *et al.* [158] and Ma *et al.* [159]. Planar P3HT-PCBM heterojunctions are only slightly lower in

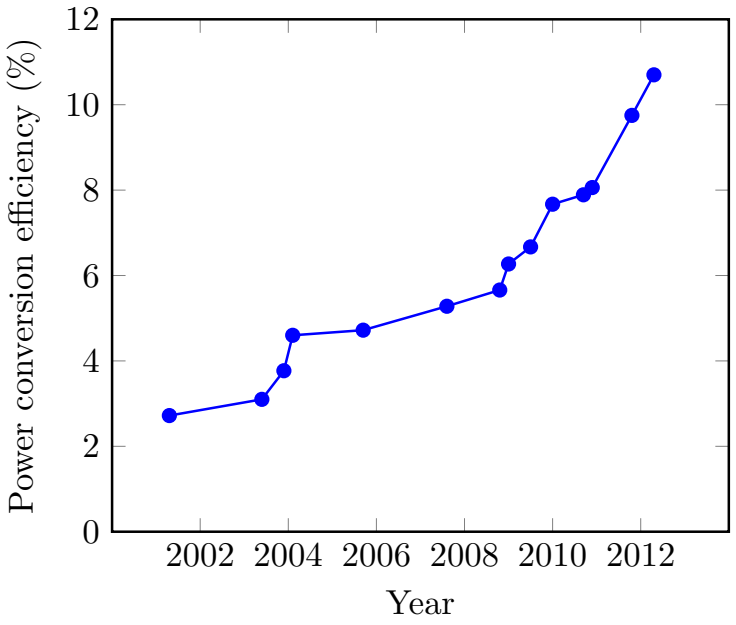

Figure 6.2: Efficiencies for state-of-the-art organic solar cells over the last decade (data from [161]).

performance as their BHJ alternative, with efficiencies of about 4%, as recently shown [160].

The constant improvement of organic solar cells efficiencies over the last decade is shown in Figure 6.2. As one can observe, almost 8% have been gained since 2002; if the same trend could be maintained over the next decade the OSCs could definitely gain a large market share worldwide.

To reach this goal and compete with silicon solar cells in terms of reliability and performance, a better understanding of the underlying physics is crucial. Computer simulations can deliver meaningful optimization strategies and help design the next generation OSCs.

We will show in the following how our kinetic Monte Carlo code can be adapted to simulate all important physical processes that are relevant for the operation of an OSC. Furthermore, we can study the impact of the morphology, the choice of the organic semiconductors or electrodes on the performance of the solar cells; such parametric analysis can give us hints for future OSC materials and architectures.

Only a few groups until now have tried to model the complex physics of polymer solar cells within a Monte Carlo framework; an early study in this direction is the one of Bler *et. al* [162], on the electronic transport in disordered organic material systems. They modeled this transport as a hopping process and achieved good agreements with measured samples. Watkins *et al.* [163] added some more physical processes to the kMC framework, like exciton dynamics to study the effect of OSC morphology on the device performance. Marsh *et al.* [164] add also the charge injection from the electrodes to the physical processes, in order to accurately study the impact of the charge carrier recombination on low illumination intensities. A first kMC framework that takes into account all important physical processes inside an OSC has been proposed by Meng *et al.* [165]; good agreements with experimental data is achieved and their study gives some first hints on device optimization.

Casalegno *et al.* [166] also include the complex physical picture in their kMC simulation framework, but they also make some improvements as compared to Meng *et al.* The most important one is the treatment of the Coulomb interactions inside the polymer solar cell. Since organic semiconductors generally have low dielectric constants, the Coulomb forces between charge carriers are not screened as efficiently as in classical semiconductors. The standard approach to use a cut-off radius when calculating the Coulomb interactions inside the OSC can be an important source of error. Therefore, Casalegno *et al.* propose a much more exact treatment of the electrostatic interactions, using the Ewald sums approach [167].

Finally, our work [168, 169] uses the same Ewald sums correction, but with an improved Monte Carlo code implementation. Rather than using the First Reaction Method (FRM), the classical choice for such stochastic frameworks, we rely on a robust implementation of the direct method [108]; we can thus avoid some sources of error when modeling the charge carrier transport through the OSC [170].

6.2 Physics of Organic Solar Cells

An organic solar cell works in the same way a standard silicon cell does, namely it converts absorbed light into energy - or better said electrical current that can

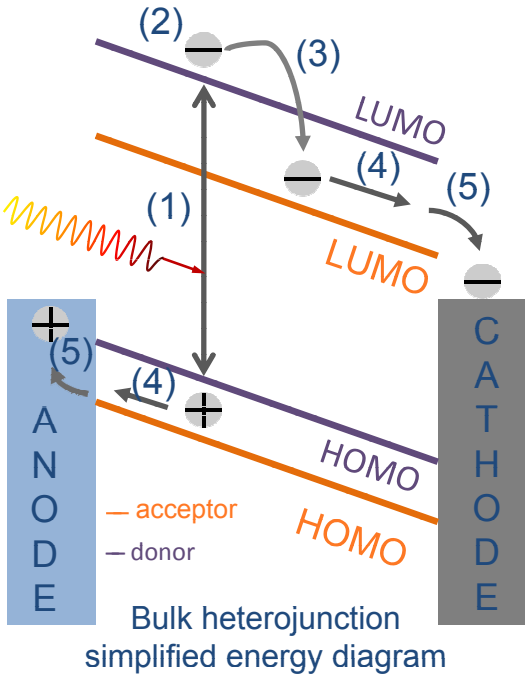

Figure 6.3: Schematic representation of all relevant physical processes in a heterojunction OSC.

then be used by commercial or private consumers. The details of the underlying physics are nevertheless a bit more complex than e. g. for a Si solar cell. In Figure 6.3 all physical processes that can take place inside an OSC are schematically shown, from the absorption of light to the production of external current:

1. Exciton generation from absorbed photon
2. (a) Exciton diffusion at the acceptor/donor interface
2. (b) Exciton decay if no interface encountered within the diffusion length
3. Exciton dissociation at the interface with charge transfer to donor and acceptor interfaces
4. (a) Charge transport (electrons and holes) via hopping between localized states
4. (b) Electron-hole recombination can also take place
5. (a) Charge extraction at the electrodes
5. (b) Charge injection at the electrodes

Let us briefly explain the above mentioned physical processes. One peculiarity of organic solar cells is that an incident photon will not generate a free electron and

a free hole (as would be the case for silicon and other typical materials), which can then be extracted via the semiconductors CB and VB, but will create a bound electron hole pair, a so-called exciton. Due to the low dielectric constant, the Coulomb interaction between the electron and hole will generate a large bonding energy of several hundreds meV, so the thermal energy at room temperature 25 meV will not be sufficient to separate them. The neutrally charged exciton can then diffuse in the organic semiconductor material, following a hopping process, and will eventually decay after a specific diffusion length.

The solution of splitting or dissociating this neutral particle was first proposed by Tang *et al.* [171] with the introduction of the heterojunction organic solar cell. Two materials are needed, with different energetic levels of the HOMO and LUMO the equivalent of the valence and conduction band in organic semiconductors. When an exciton meets such an interface, it will be energetically favorable for the electron to be transferred into the LUMO of one semiconductor the so-called acceptor material while for holes it will be energetically favorable to be transferred into the donor HOMO.

Several architectures have been developed for the implementation of the heterojunction concept, as one can observe in Figure 6.4. Both have some advantages and problems, when considering the exciton dissociation efficiency and the electron-hole recombination losses. While for the bilayer device [171] the acceptor and donor materials are stacked on top of each other, in the case of a bulk heterojunction (BHJ) [172–174] we can observe a blend of the two materials where the acceptor and donor phases intermix. A bilyer device has less acceptor/donor (A/D) interface area and therefore the efficiency of dissociating an exciton is low. On the other hand, once an exciton is dissociated the electron and hole can both be successfully extracted, the recombination losses are almost inexistent since the two types of charge carriers will never meet again inside the device. In the case of a BHJ the A/D interface area is larger, so we can expect that virtually all photogenerated exitons will be dissociated. However, due to the phase intermixing, there is a large probability that an e.g. electron, drifting in the build-in electric field towards the collecting electrode, will find itself in the vicinity of a hole and recombine. Therefore the recombination losses play an important role in the BHJ solar cells; one solution is the use of optimized

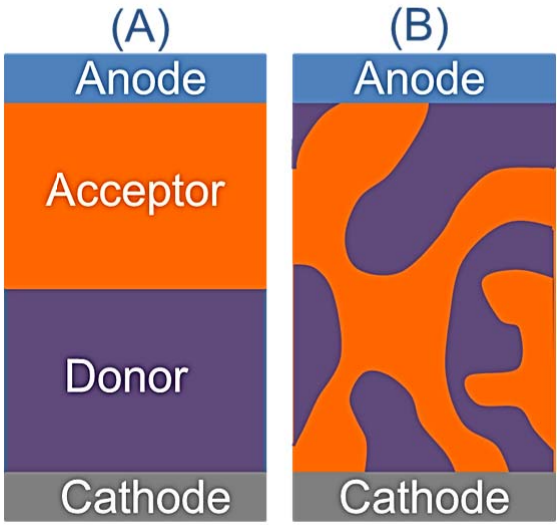

Figure 6.4: Two different implementations of the heterojunction OSC concept: (a) the bilayer and (b) the bulk heterojunction architecture.

contacts that lead to an increased build in electric field and thus a fast extraction of the charge carriers from the blend.

The transport of electron and holes through the acceptor and donor materials towards the collecting electrodes, once the exciton is successfully dissociated, has again some peculiarities compared to charge carrier transport in solid semiconductors. While the ordered crystal lattice of a classical semiconductor will lead to the formation of sharply defined conduction and valence bands, which can be used for charge carrier transport, in the case of organic semiconductors, mainly due to the disorder inherent to their amorphous state, the HOMO and LUMO can be described as a distribution of localized states rather than a continuous energy band. The charge carrier transport can be best described as a hopping process between these localized states, a fact first reported by Miller and Abrahams in their study [175]. This field and temperature dependent process explains the very low average mobilities reported for such organic semiconductors, at room temperature: 10^{-4} to 10^{-3} $cm^2/V \cdot s$ are typical [176–178].

As stated above, due to the low dielectric constant and the typically small intrinsic charge carrier densities inside organic semiconductors, the screening length of the electrostatic interactions between charge carriers is considerably larger than in classical semiconductors. This will lead to a long range attractive force between electron and holes, and depending on the morphology, it will

increase the risk of charge recombination. Photo-generated charge carriers are thus lost through this process, since they will not contribute to the external current of the solar cell.

Finally, the collection step at the electrodes is the last important physical process of the complex working principle of an OSC. Only the collected charge carriers effectively contribute to solar cells external current and are accounted when calculating figures of merit (FOM) like efficiency. The choice of the metal electrodes depends much on the desired application of the organic photodiode. For a solar cell, a large built-in voltage, at 0 applied bias, is highly desired; for an organic photodetector the requirements are not as strict, since a reverse bias will anyway be applied to the device. In both cases however, no energetic barrier should for the charge carriers at the corresponding electrode this means for electrons at the cathode and for holes at the anode. A careful choice of the electrode material is therefore necessary, taking into account the energetic levels of the acceptor and donor HOMO and LUMO. If a forward operation regime of the organic photodiode is desired, the injecting barriers have to be adjusted accordingly.

The interested reader can find more detailed reviews on the working principle and physics of OSC in recent literature [179–181].

6.3 Kinetic Monte Carlo Implementation

We have already drawn a picture of the charge generation, transport and collection inside an organic solar cell. Similar to Section 3.4, we will now shortly enumerate the actual physical rates, implemented in our simulator to model the physical process. We stress here again that our kMC framework is highly flexible and can be adapted for a large variety of problems. In the present case, we only need to implement the desired transition rates and make some modification to the geometry generation algorithm - we will come back to this point in the next sections - to be able to simulate the IV of an organic solar cell under illumination. The same routine will be executed, as depicted in Figure 3.3, and the next transition is again chosen based on the Gillespie algorithm and the generation of two random numbers, as was the case in the previous sections.

6.3.1 Exciton Physics

As mentioned above, when illuminated, bound electron-hole pairs - the excitons - will be generated inside an OSC. Depending on the thickness of the organic blend and the morphology, complex effects like interference or diffraction could play a role [182]. A complete optical model including these effects would be desirable, and a near-future implementation in our code seems feasible, but the model actually used to obtain the experimental fits relies on the simplification of a constant generation rate over the whole organic layer.

We can therefore write for the total exciton generation rate:

$$A_{exg} = a_{exg}(M_x - 1)(M_y - 1)(M_z - 1)l^3 - N_{occ} \tag{6.3.1}$$

where M_x, M_y and M_z are the total number of grid points for our discretized structure and N_{occ} the grid points already occupied by a photo-generated exciton. If we assume normal light incidence (with respect to the XY plane) and typical absorbtion coefficients [180], we can conclude that:

$$a_{exg} = j_{sat}\frac{10^{-17}}{2e(M_z - 2)} \tag{6.3.2}$$

with j_{sat} the material-dependent saturation current.

Once generated, the excitons can diffuse in the organic photolayer. The diffusion is modeled as a random hopping to nearest-neighbor grid-points, all directions $\pm$x, $\pm$y, $\pm$z are allowed, as long as the neighboring grip point is not occupied. The hopping rate is implemented as:

$$a_{exh} = \frac{1}{\tau_{hop}} = \frac{6D}{l^2} \tag{6.3.3}$$

We denote where with l the distance to the nearest neighbor grid point and with D:

$$D = \frac{L^2}{6T} \tag{6.3.4}$$

the diffusion coefficient [183] for the hopping process. L and T are the average diffusion length and time before a decay process can take place; typical values can be found in [181].

The exciton decay rate is constant and is defined as the inverse of the average exciton lifetime T:

$$a_{exd} = \frac{1}{\tau_{lifetime}} \tag{6.3.5}$$

We have used throughout the simulations a value of 500 ps for T [181].

Finally, we allow in our simulation code that excitons dissociate in free electrons and holes. Two conditions must be met for this process to happen: at least one neighbor grid point must belong to a different material than the current grid node and both nodes must be unoccupied. The dissociation rate is implemented as the inverse of the separation time, once a donor/acceptor interface is met:

$$a_{exs} = \frac{1}{\tau_{separation}} \tag{6.3.6}$$

Typical separation times are very small, in the order of 50 fs [184,185]

6.3.2 Electron and Hole Transport

Once an exciton is dissociated, the electron and hole can move freely inside the acceptor and donor materials. The transport is modeled as a Miller-Abrahams [175] hopping process. The hopping rate between node i and node j of our grid is then:

$$a_{hop} = a_0 \cdot \exp(-2\gamma r_{ij}) \begin{cases} \exp\left(-\frac{\Delta E_{ij}}{k_b T}\right) & : \Delta E_{ij} > 0 \\ 1 & : \Delta E_{ij} \leq 0 \end{cases} \tag{6.3.7}$$

The prefactor a_0 is refferd to as the attempt-to-escape frequency, with typical values in the order 10^{12} 10^{13} s^{-1} [166]. For the inverse localization radius γ again values from literature have been used [163] while r_{ij} is the distance between to neighboring grid nodes.

Finally, the exponential term, which basically accounts for hopping processes uphill in energy, has several components:

$$\Delta E_{ij} = E_i - E_j = \Delta E_{ij}^0 + \Delta E_{ij}^F + \Delta E_{ij}^C \tag{6.3.8}$$

Here the first term denotes the local energy difference of the LUMO (HOMO) level e.g. for electrons (holes); since for organic materials a sharp energy band cannot be assumed due to the inherent disorder, a Gaussian energy distribution of the hopping sites inside the LUMO (HOMO) has been assumed. The second term accounts for the externally applied electric fields, while finally the third term takes into account the Coulomb interactions between charge carriers inside the OSC. It can be computed as $\Delta E_{ij}^C = 1/2q(U_i - U_j)$, where U_i and U_j are computed using the Ewald sums approach. We will treat this topic in more detail in the next section.

Also important for the charge transport of electron and holes, the recombination processes are also included in our simulations. We rely on the extensive study by Marsh *et. al* [164] and use for the following a recombination rate $a_{rec} = 5 \times 10^5$ s^{-1}.

6.3.3 Charge Collection and Injection

In order to determine the actual generated photo-current and thus the efficiency of the OSC, together with other typical FOM, we need to know how many charge carriers have been successfully collected at the corresponding electrodes. A counter is responsible for keeping track of the charge carriers that reach the certain external grid nodes, marked as electrodes. The collection process is basically a hopping process with $\Delta E_{ij} \leq 0$, so typical collection rates are in the range $a_{col} = 1 \times 10^{10}$ s^{-1}.

To model our OSC as accurately as possible, the contribution of the dark current to the cells total current is also included. This dark current the current injected in the OSC in reverse bias is modeled as a hopping process from the electrode to the corresponding HOMO (LUMO), if this is the anode (cathode) and is based on the study by Wolf *et al.* [186].

We can therefore write for the electrode injection rate:

$$a_{inj} = a_0 \cdot \exp(-2\gamma) \sum_n \exp\left(-\frac{E_b^{(n)}}{k_B T}\right) \tag{6.3.9}$$

with $E_b^{(n)}$ the injection barrier seen by the charge carrier and γ the above mentioned delocalization radius. These contributions of the dark current are summed up for all nodes that have a neighboring electrode node, as the formula clearly shows.

6.3.4 Treatment of Electrostatic Interactions

Since organic semiconductors usually have a small dielectric constant ϵ, the electrostatic interaction between charge carriers and with the metallic electrodes cannot be ignored.

As already mentioned, most simulation studies until now make use of a cut-off radius to limit the calculation of the Coulomb interactions [163–165, 187]. We have opted for a more exact treatment of these interactions, following an approach similar to Casalegno *et al.* [166], making use of the Ewald sums.

We will make use of the image charge method [188, 189] to calculate the induced surface charge in the metal electrodes, by the hopping electrons and holes. For an organic layer of thickness Z, stacked between two metal electrodes, a main simulation box with a height of $2Z$ is necessary to compute the various mirror charge contributions; a proof of this statement can be found in the above given references.A graphical representation is sketched in Figure 6.5.

The electrostatic potential in each grid node i can therefore be written as:

$$U_i = \frac{1}{4\pi\epsilon_r\epsilon_0} \sum_n \sum_{j=1}^{2N} \frac{q_j}{|r_{ij} + n|} \tag{6.3.10}$$

where $n = (n_x X, n_y Y, 2n_z Z)$ accounts for the periodicity of the image charges and the second sum computes the Coulomb interactions between charge carriers in the main simulation box.

As one can imagine, the evaluation of the above sum is a complex task; on workaround that can help us ease the computational burden, while keeping the

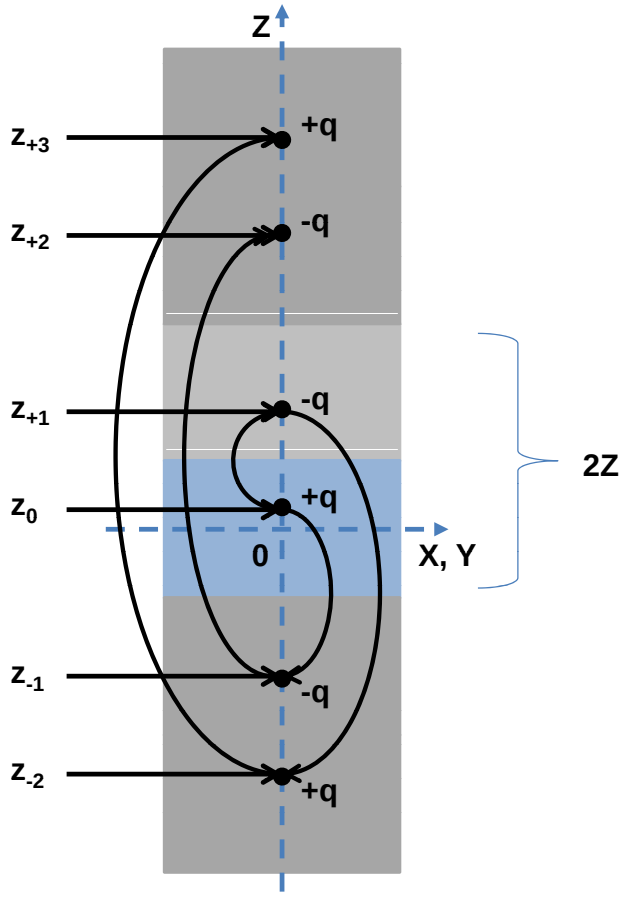

Figure 6.5: Concept of the image charge method: charge carriers inside the OSC induce mirror charges in the electrodes. Observing the periodic pattern and exploiting the periodic boundary conditions, the electrostatic problem can be solved only in a simulation box of size $X \cdot Y \cdot 2Z$. Figure redrawn from [166].

accuracy of the solution intact is the use of the Ewald sums [167]. A deduction of this method is outside the scope of this work, we can however shortly resume the procedure: the sum of Equation 6.3.10 is split into two sums accounting for the short- and long-range Coulomb interactions. Computing the short-range interactions in real space, the long-range in reciprocal space and paying attention to the summation order [190, 191], a fast convergence towards the exact solution can be achieved.

To improve the simulation time and resource handling, all node potentials are precomputed before the actual simulation, so their contribution to the total node

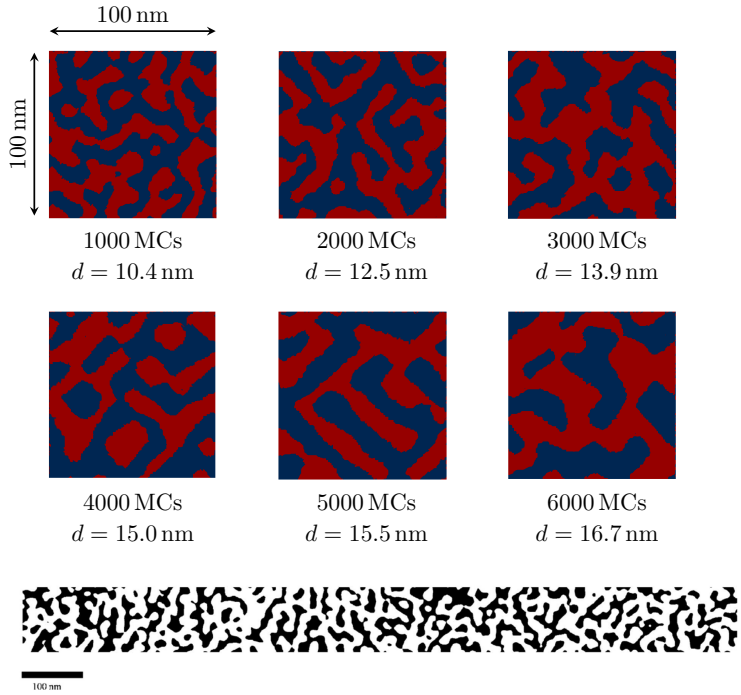

Figure 6.6: The morphology generated with the spin-exchange algorithm can be controlled and adjusted with the number of swaps, in order to fit an experimental TEM picture of a OSC blend (taken from [192]).

energy, $\Delta E_{ij}^{C} = 1/2q(U_i - U_j)$ can be easily added in the case of a hopping process.

6.4 Geometry Generation

We will concentrate in the following on the modeling and simulation of bulk heterojunction solar cells (BHJ); as can be already seen in Figure 6.4, a BHJ solar cell is characterized by a strong intermixing of the acceptor and donor phases, a fact confirmed by experimental observations.

One convenient way of generating such a structure is to use the Kawasaki spin-exchange algorithm [163]. It is based on a Metropolis Monte Carlo (MMC) procedure, and will try to obtain the relaxed energy state of a system after a number of runs. To apply the algorithm for our problem, virtual spins are assigned to grid nodes, namely spin up for donor sites and spin down for acceptor sites. An equal number of acceptor and donor sites is randomly attributed to our mesh grid in the initialization step.

From here on, the standard Ising model [193] is applied; the interested reader can find a detailed description in the given reference. The important points of the algorithm are: starting for a pair of opposite spins, the interactions to the nearest neighbors are computed. The calculation is redone, this time with swapped spins of the neighboring grid nodes. The difference in energy (each spin has equal reference energy, but of opposite sign) between the two spin configurations of the neighboring grid points is computed. As for most MMC algorithms, a configuration with lower total energy is accepted, while for higher total energy, the configuration is accepted with a random probability according to a Boltzmann distribution:

$$P(\Delta\epsilon) = \frac{\exp -\frac{\Delta\epsilon}{k_B T}}{1 + \exp -\frac{\Delta\epsilon}{k_B T}} \tag{6.4.1}$$

where $\Delta\epsilon$ is the difference between two swapped states.

The generated geometry and intermixing of the phases can be easily controlled, by allowing only a specific number of swaps to be carried out. Of course, for less swaps, a large, random intermixing is obtained, while allowing more swaps will I the limit lead to a complete phase separation, similar to the bilayer architecture. Some simulated morphologies, after different number of swaps are shown in Figure 6.6.

6.5 The P3HT-PCBM Solar Cell

The first OSC to be analyzed [169] is the maybe most common BHJ organic solar cell, namely the P3HT-PCBM one. In Figure 6.7, the modeled geometry is shown, together with a cut through the blend, in a plane parallel to the Z-axis. The two intermixing phases, depicted with distinct colors, can be clearly observed in the figure; also the different values of the HOMO and LUMO level of the acceptor and donor material can be noted in the same figure.

The set of simulation parameters for this OSC are largely taken from literature, as already mentioned in the physics sections and resumed in Figure 6.8. We choose a lattice constant of 1 nm in order to accurately resolve short-range processes, such as charge carrier hopping. The modeled cell thus has a thickness of the

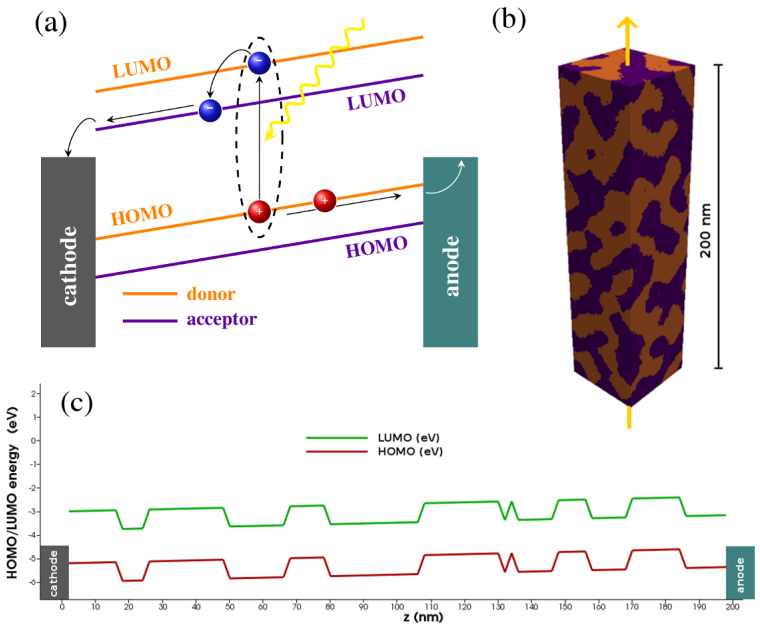

Figure 6.7: (a) Schematic of relevant physical processes for the OSC under study. (b) A 50 x 50 x 200 nm generated BHJ structure. (c) Band diagram of the generated structure along a cut-line parallel to the z-axis (taken from [169]).

organic blend of 200 nm, in good agreement with blend thicknesses measured in our laboratory.

One major advantage of kMC simulations, as opposed to rate-equation based simulations, is that they offer the possibility of real-time particle tracking inside the device. We can thus get a unique insight in the physical processes and interactions that are happening inside the OSC. This feature also allows us to extract FOM like exciton dissociation efficiency, internal quantum efficiency or recombination efficiency, since we keep track of each particle generated or diffused inside the solar cell. One interesting case is depicted in Figure 6.9: we can observe here the implemented exciton physics exemplified on three particles the exciton trajectories are colored green. An exciton in the upper part of our modeled geometry is photogenerated and starts hopping randomly. The simulation is carried out near open circuit voltage, but since the excitons are anyway neutral, no dependency on the electric field can be observed. This exciton will carry out a number of hopping processes and will eventually decay, because no acceptor/donor interface is met. Interesting to observe are also the periodic boundary conditions of our kMC simulator: an exciton that reaches a grid node

Parameter	Symbol	Value
Nodes x direction	M_x	50
Nodes y direction	M_y	50
Nodes z direction	M_z	200
Lattice constant	l	1 nm
Relative permittivity	ε_r	3 to 5
Work function cathode	ϕ_{cathode}	-4.3 eV
Work function anode	ϕ_{anode}	-4.95 eV
PCBM (acceptor) HOMO level	E_A^{HOMO}	-6.0 eV
PCBM (acceptor) LUMO level	E_A^{LUMO}	-3.8 eV
P3HT (donor) HOMO level	E_D^{HOMO}	-5.17 eV
P3HT (donor) LUMO level	E_D^{LUMO}	-3.0 eV
Cluster size	d	15.57 nm
External voltage range	V	-0.1 to 0.8 V
Simulation time	t_{stop}	1 ms

Figure 6.8: Some selected parameters used for the simulation of the P3HT-PCBM OSC.

with e.g. X-coordinate=0 and still continues to hop in a negative direction will appear at the other end of the device with the X-coordinate=x_{max}. The other two excitons in the lower part of our modeled OSC both meet an acceptor/donor interface and dissociate. The trajectories of the generated electrons and holes are colored blue and red, respectively. Since we are near open circuit voltage, the applied electric field is negligible, therefore the Coulomb attraction is a dominant effect. We can observe this fact by looking at the trajectories: in both cases, the electrons and holes move in following the same pattern, bound by the attracting Coulomb force.

The next case we will treat is a direct comparison of our simulation results with measured experimental data on a fabricated P3HT-PCBM solar cell of the same thickness. In Figure 6.10 we can observe a good agreement between the simulation and measured curve, validating our implemented physical model. We can report a simulated J_{sc}=9.2 mA/cm^2 vs. J_{sc}=9.4 mA/cm^2 for the measured OSC and a V_{oc}=0.63 V vs. V_{oc}=0.61 V again for the experimental one.

Also of interest are the FOM like the internal quantum efficiency and other related efficiencies. They can be read in Figure 6.11 for various applied bias

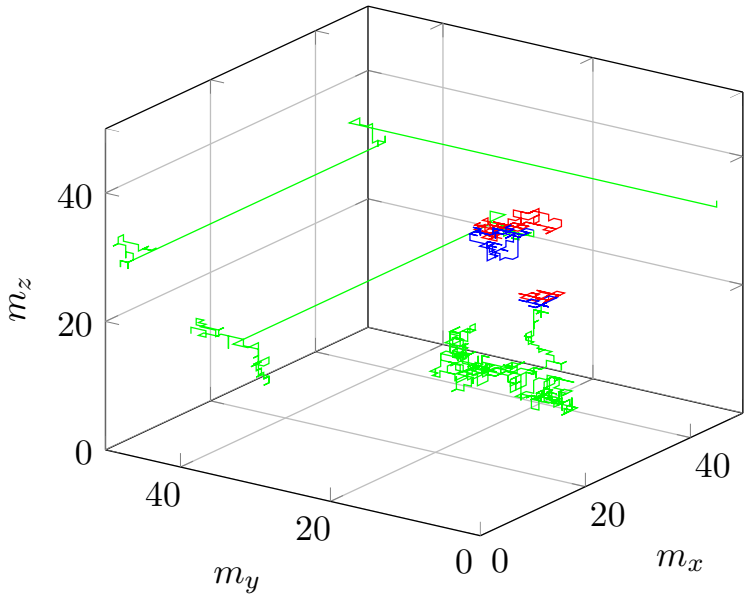

Figure 6.9: Trajectories of photo-generated excitons - green - that can decay or dissociate in electrons - blue. and holes - red (taken from [192]).

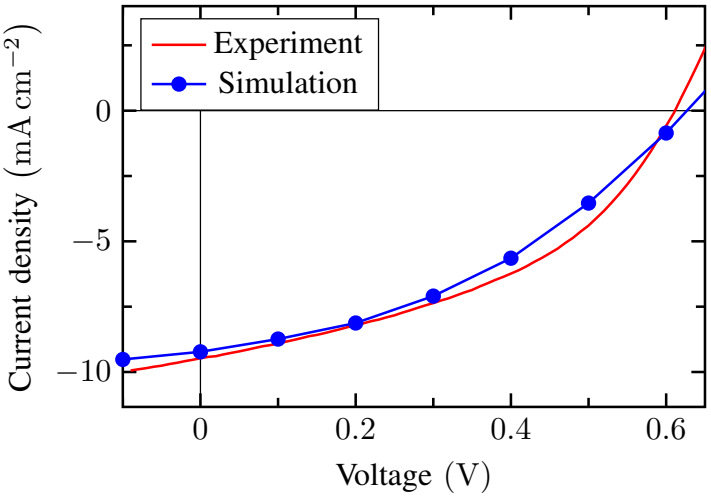

Figure 6.10: Good agreement between measured and simulated device is reached using our kMC simulation algorithm (taken from [169]).

voltages. As one could expect, the exciton dissociation efficiency η_{exs} remains constant for the whole voltage range; excitons are neutral and do not see the applied electric field. The only parameter that will influence the dissociation efficiency is the morphology of the cell, which remains constant for each incrementation of the voltage. The constant value of 95 % can be explained by the average size of l=15 nm of a phase cluster acceptor and donor for the modeled

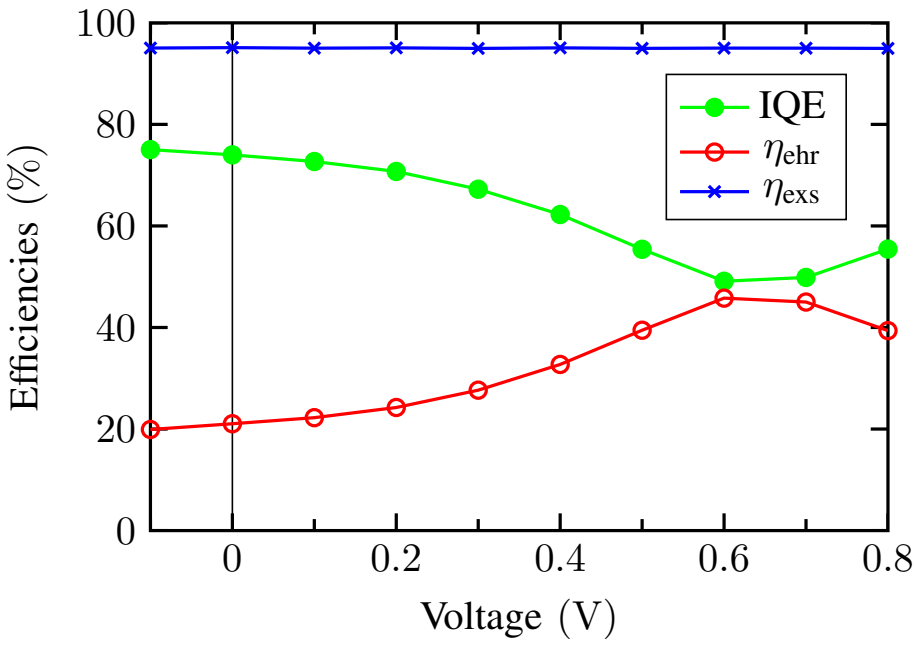

Figure 6.11: Internal quantum efficiency, exciton dissociation efficiency and recombination efficiency for the modeled OSC at various bias points (taken from [169]).

geometry. We can thus calculate that for an exciton diffusion length larger than $l/2$ virtually all excitons should meet an interface an dissociate; this is also the case, with an exciton diffusion length of 10 nm, larger than $l/2$=7.5 nm. Looking at the recombination efficiency η_{ehr}, we can observe that for low bias voltages it has a low value, it then increases, has a peak around the open circuit voltage and decreases then again. This behavior can be explained by the Coulomb interactions between the charge carriers and the internal electric field inside the device. At 0 V applied bias, a large built in electric field inside the device can increase the extracting efficiency since the charge carriers will rapidly drift at one electrode. Near the open circuit voltage however, the charge carrier are not exposed to any electric field; due to the low dielectric constant of the blend, the electrons and holes will experience a Coulomb attraction and will most likely recombine. The internal quantum efficiency (IQE) will then for sure also exhibit a voltage dependency, decreasing around the V_{oc}, since in this voltage range a lot of charge carriers get lost through the recombination channel.

Having understood the basic working principles of our OSC, a parametric analysis is carried out in order to improve the cell performance. The key parameters to

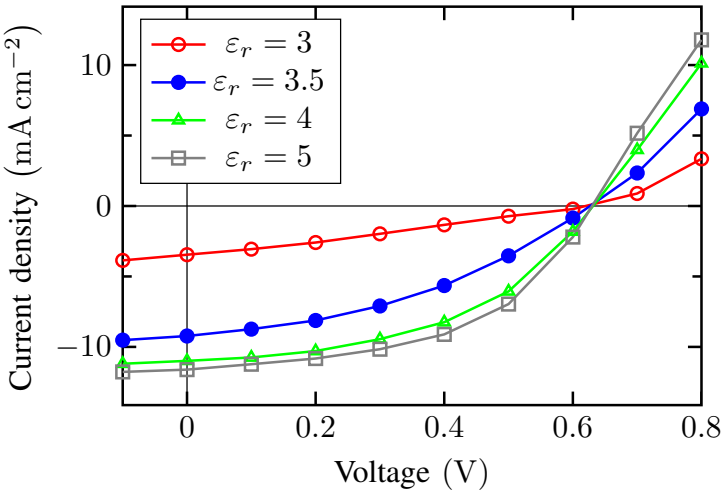

Figure 6.12: Simulated J-V characteristic for OSCs with different dielectric constant, ranging from 2 to 5 (taken from [169]).

influence are η_{exs} and η_{ehr} and we will study the effect of an increased dielectric permittivity of the blend on them. The simulated J-Vs for various dielectric constants are shown in Figure 6.12; a clear improvement can be observed for higher permittivities, with a calculated fill factor of more than 50 % for ϵ_r=5.

This result is not really surprising if we look als at Figure 6.13, where the different cell efficiencies are plotted. We can observe that the recombination efficiency decreases from 62 % to only 5 % when increasing the dielectric constant from 2 to 5. Also the peak around the open circuit voltage is largely suppressed in the case of higher permittivities. All these improvements can be explained by the efficient screening of the Coulomb interaction in the OSC with ϵ_r>3.5, leading to a much reduced carrier recombination inside the device an thus an increased internal quantum efficiency.

Our results are also in good agreement with a similar study on the impact of the dielectric constant on the performance of OSC, recently published by Koster et al. [194]. Using a modified drift-diffusion simulator, they also conclude that one very promising direction for the optimization of OSC is the use of new organic materials with large dielectric constants. This direction could lead to OSC reaching the theoretical limit of 25 % external quantum efficiency, making them maybe the best and cheapest alternative on the market.

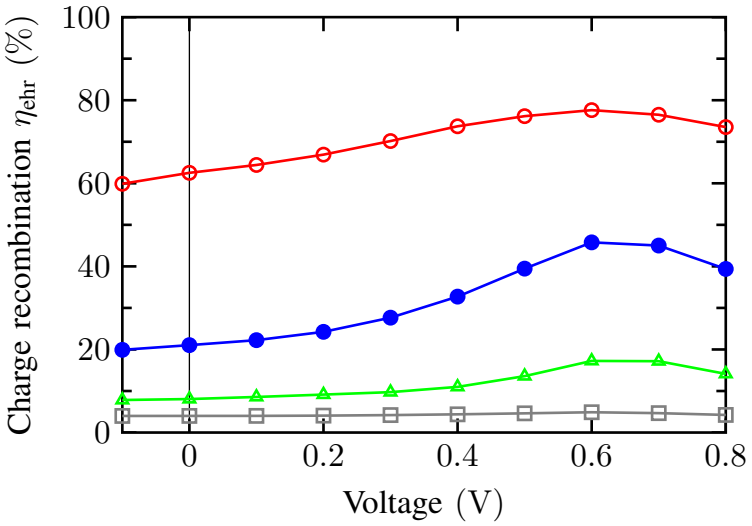

Figure 6.13: The recombination efficiency at various bias points for the analyzed OSC with different dielectric constant (taken from [169]).

6.6 The PCPDTBT-PCBM Solar Cell

The next OSC we will focus on [169] is a novel, low-bandgap BHJ solar cell. Recently, low-bandgap materials have attracted the attention of researchers because of their unique properties of absorbing light well into the infra-red region of the spectrum, increasing thus the amount of radiation that can be successfully converted into current and extracted an the terminals of a solar cell.

Using again our variation of the Kavasaki spin-exchange algorithm, we can generate various morphologies for the PCPDTBT-PCBM solar cell. Figure 6.14 shows four such morphologies, with average intermixing phases ranging from 2 to 30 nm. Since experimental data on the actual cluster size for such a low-bandgap BHJ is almost impossible to obtain, we will simply try to fit different morphologies to experimental data, in order to validate our assumption.

The parameters used for this section are again summarized in Figure 6.15. As a supplementary check, in Figure 6.16, a cross-section through the active layer shows the energetic level for the HOMO of the two organic materials of the blend. A large difference can be observed between the donor and the acceptor, not surprising if we recall that PCPDTBT is a low-bandgap polymer.

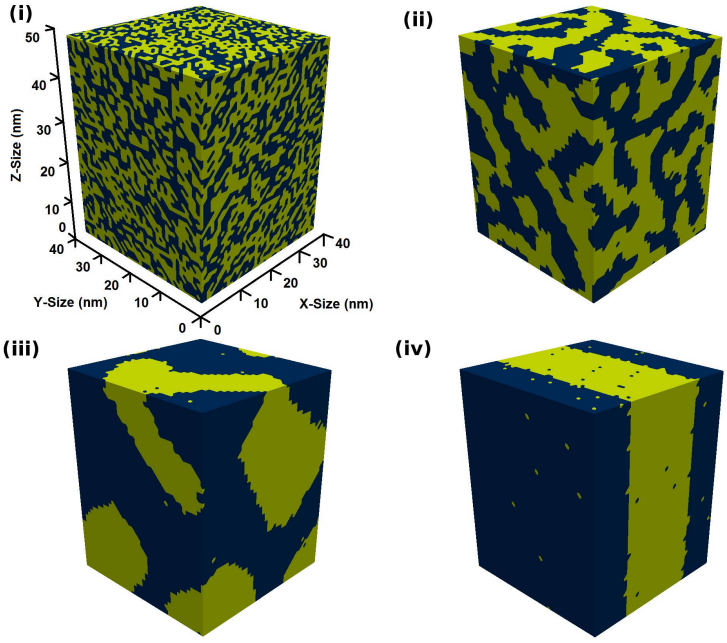

Figure 6.14: Generated morphologies of the low-bandgap OSC, with average cluster size of (i) 2 nm, (ii) 6 nm, (iii) 16 nm and (iv) 28 nm (taken from [168]).

Taking advantage of the unique features of the kMC simulation approach, we also analyze the charge carrier transport through the active layer, after the exciton dissociation, by recording the particles trajectories. We can observe in Figure 6.17 that the excitons trajectories marked green will dissociate after only a few hopping steps and the resulting electrons and holes will start hopping towards the collecting electrodes. Nevertheless, the the charge carriers seem to need a lot of hopping processes until they find a percolating path to one of the electrodes. The fast exciton dissociation and slow charge carrier extraction can be explained if we take into account the average cluster size of about 3 nm for the above given example. Such a morphology will translate into a high probability of a photo-generated exciton to find an acceptor/donor interface and dissociate, but will also mean that percolating paths for electrons or holes to reach their collecting electrodes will be very long.

To validate our theoretical model, a direct comparison with a measured low-bandgap BHJ solar cell is shown in Figure 6.18. A very good agreement is achieved for this 50 nm thin OSC; the morphology best fitting the experimental data has a cluster size of 5 nm. The shape of the J-V characteristic can be

Parameter	Symbol	Value
Nodes x direction	M_x	50
Nodes y direction	M_y	50
Nodes z direction	M_z	50 to 200
Lattice constant	l	1 nm
Relative permittivity	ε_r	3.5
Work function cathode	ϕ_{cathode}	-4.25 eV
Work function anode	ϕ_{anode}	-5.0 eV
PCBM (acceptor) HOMO level	E_A^{HOMO}	-6.0 eV
PCBM (acceptor) LUMO level	E_A^{LUMO}	-3.8 eV
PCPDTBT (donor) HOMO level	E_D^{HOMO}	-5.28 eV
PCPDTBT (donor) LUMO level	E_D^{LUMO}	-3.6 eV
Monte Carlo steps	MCs	20
External voltage range	V	-0.1 to 0.8 V
Simulation time	t_{stop}	1 ms

Figure 6.15: Some selected parameters used for the simulation of the low-bandgap OSC (taken from [168]).

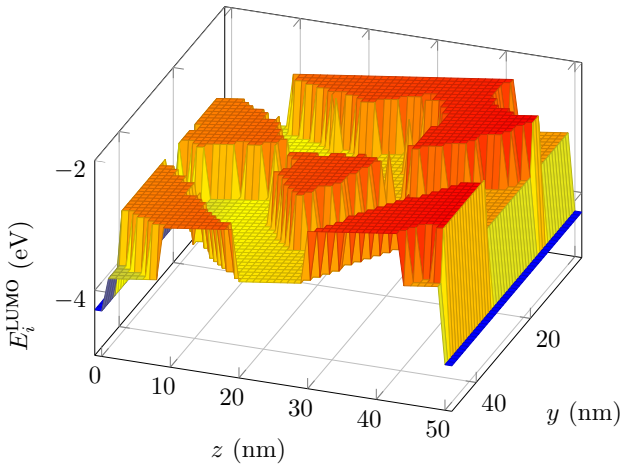

Figure 6.16: Energetic levels of the HOMO for a slice of the generated morphology (taken from [168]).

explained by analyzing also the internal processes of the solar cell: we can note that the exciton dissociation efficiency is above 95 %, a high value that can be expected due to the large acceptor/donor interface area of the modeled morphology. The recombination losses however are also large, again due to the phase intermixing: the probability that e.g. an electron will find itself in

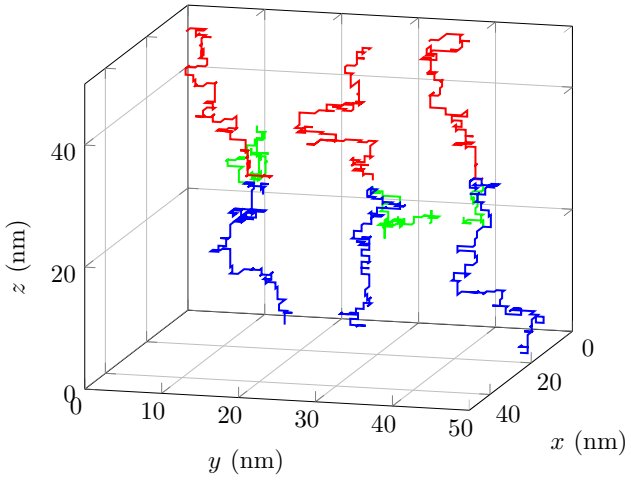

Figure 6.17: Trajectories of tracked photo-generated excitons, electrons and holes inside the organic device - marked green, blue and red (taken from [168]).

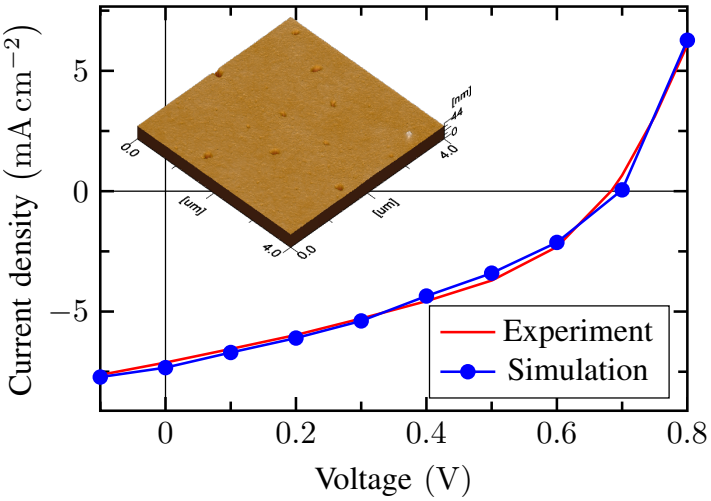

Figure 6.18: Best agreement obtained between our modeled device and the measured OSC (taken from [168]).

the vicinity of a hole, on his way to the collecting electrode, is very large. The recombination losses also explain why the current of the OSC does not saturate in reverse bias: even at low negative voltages, when the internal field is large, the morphology prevents an efficient extraction of the charge carriers.

A further test for the validity of our model is to try and model the impact of various device thicknesses on the J-V characteristic. In Figure 6.19 we qualita-

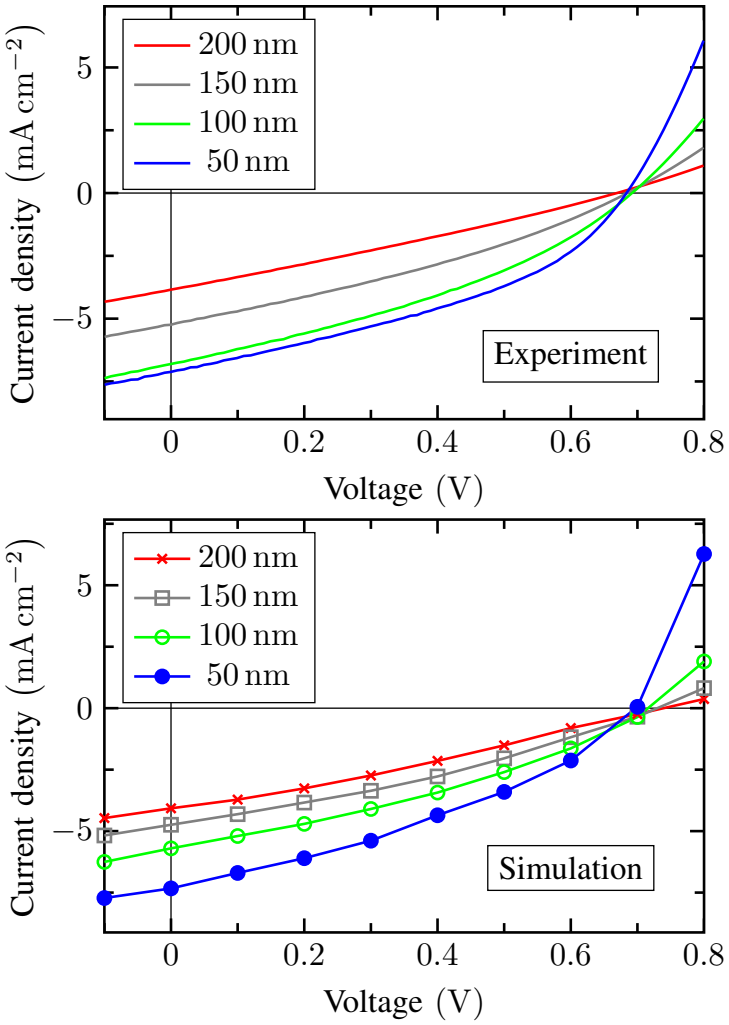

Figure 6.19: Measured vs. simulated results for low-bandgap OSCs with increasing thickness of the organic blend (taken from [168]).

tively show that the same trend can be observed for our modeled devices as can be for the experimentally fabricated ones. With increasing the device thickness, the short-circuit current J_{sc} decreases together with the fill-factor, while the V_{oc} remains constant. The agreement also justifies the choice for our morphology; all the results have been obtained keeping the average cluster size and all other model parameters constant, while only varying the thickness of the modeled geometry.

In order to completely clarify the observed behavior a look at the IQE for the devices with various thicknesses could be interesting. These IQEs are plotted in Figure 6.20 for the thicknesses ranging from 50 nm to 200 nm. A drop in the

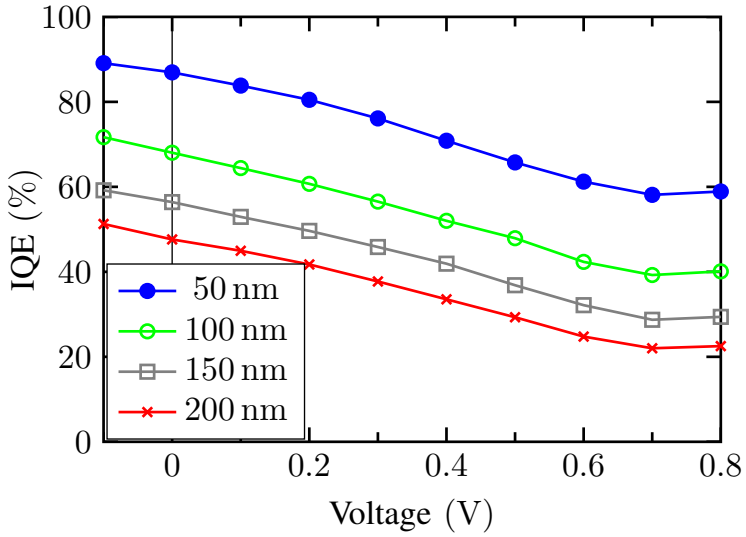

Figure 6.20: Internal quantum efficiency for the same family of low-bandgap OSCs with varying device thickness (taken from [168]).

IQE can be observed, as the devices become thicker, explaining also the drop in current and fill-factor. Since the morphology is identical, we can exclude that the exciton dissociation efficiency has dropped. The most probable mechanism responsible for this drop is the recombination loss: indeed when the thickness of the devices is increased, the internal electric field, at the same externally applied bias voltage, will decrease. A reduced internal electric field coupled with longer percolating paths needed by the charge carriers to reach the electrodes is our best explanation of the phenomenon.

6.7 Conclusion

We have shown in this section that the kMC algorithm is a versatile tool, capable of simulating also various other physical processes. We have shown how the simulation code can be easily changed to include mechanisms that are relevant for state-of-the-art organic solar cells.

Making use of a modified spin-exchange algorithm, realistic morphologies for bulk heterojunction solar cells can be generated and analyzed. We can successfully reproduce standard measured OSC J-V characteristics, as well as novel low-bandgap solar cells.

Our simulation approach gives as a unique insight into the internal processes that determine the performance of such OSCs. Trajectories of single particles can be tracked and recorded, local charge accumulations can be observed and mobilities extracted from repeated hopping processes. Understanding the limiting factors can help us propose optimization techniques that can make OSC an attractive alternative to standard solar cells now available on the market.

7 Conclusion and Outlook

We have focused in this work on the development of a simulation framework that can successfully duplicate, but can also help us explain the leakage behavior in ultra high-*k* dielectrics.

The need for new and improved dielectric materials – as stated in recent ITRS roadmaps – that can keep the peace with Moor's law, has brought material scientists and development engineers in front of new challenges. While it has become clear that downscaling the electronic devices, especially in the case of DRAM capacitors, will not be possible by keeping the established material systems – like Silicon and Silicon oxide – the new high-*k* material systems, with increased charge retention capabilities, still face serious reliability problems. Especially the very high leakage currents, reported by experimental measurements on various novel dielectric layers, confirm that further study is needed in order to understand the mechanisms responsible for this behavior and thus to optimize future devices.

Simulations could provide a versatile tool, helping process engineers in understanding what physical phenomena play a role in the observed I-V characteristics for different measured MIM capacitors. But as already stated in the introduction of this thesis, most of the available simulation studies focus on one dominant leakage mechanism – sometimes two, depending on the temperature and bias regime. They rely on analytical models for e.g. trap-assisted-tunneling processes and fail to deliver meaningful results if two or more competing leakage channels are responsible for the measured I-V characteristics, or they interact strongly.

We have chosen to implement a stochastic framework, where we can take into account a variety of physical processes, without having to assume a dominant mechanism in advance. Once all the possible transport mechanisms are defined, a kinetic Monte Carlo algorithm will choose the next transition and increment

the simulation time with the help of random numbers. We are thus able to reproduce measured leakage vs. voltage curves for the novel high-*k* material system SRO/STO/SRO over a large temperature interval. We can extract in a physical manner quantities that are difficult to determine by experimental measurements and can only be approximated, like exact energetic depth of defect states inside the dielectric bandgap or their concentration. The dominant transport mechanisms in the dielectric layer can be successfully identified. Furthermore, carrying out a parametric analysis, we can see the influence of different electrode materials on the leakage properties and we can quantify the impact of a defect state reduction in the STO layer on the current. Optimization techniques are also analyzed, with the finding that a defect free interlayer, as suggested by [149] would greatly improve the performance of our MIM capacitor, making it a suitable choice for DRAM applications.

Until now, we have showed the advantages of using a stochastic approach in order to model and explain the leakage current in high-*k* materials. There are however some problems when trying to apply this procedure on e.g. realistic, deep trench capacitor structures. The main limitation is the long simulation time, since a MC approach will calculate each possible transition, from a wide range of physical processes, starting from a defined initial state; after a transition has occurred, the transitions need to be recalculated and so on. Another disadvantage would be the limited applicability of a MC technique on larger, complex structures.

We therefore decided to combine the high prediction capabilities of the Monte Carlo tool with the flexibility and robustness of a drift diffusion simulator. In this work, we have showed how using data extracted from complex kMC simulation, as input information for our DD model, can deliver accurate results again in good agreement with the measurements. Electronic properties of the dielectric layer, as enumerated above and the successful identification of the dominant transport mechanisms can thus be used to implement a very physical model in commercially available TCAD frameworks.

Modern DD simulators already support the implementation of complex transport phenomena, like TAT over nonlocal meshes. The main problem for such simulators remains the still “empirical” fitting procedure of the simulated vs. measured data curves, since input parameters and calibration data can be found,

at best, for traditional Silicon based devices. Using our kMC results and gained knowledge allows us to activate and initialize an accurate physical model, while keeping all the advantages of the DD framework. Complex 3D geometries can be modeled, the mathematical solvers are highly optimized and various visualization and post-processing capabilities already exist.

Of course, we have to stress out that the transition from kMC to DD cannot take place without the loss of possibly important information. While the total simulated leakage behavior is almost identical in both approaches, the information about the contribution of single transport mechanisms and their behavior over different bias and temperature ranges is not available anymore in the DD framework. The competing leakage channels are not modeled as independent processes – a fact that can lead to the under- or overestimation of the total leakage current. One easy to imagine example is to switch off a leakage model in a DD simulation at e.g. high temperature: the direct effect would be a reduction of the total current, since one term that contributes to the generation-recombination rates inside the dielectric is now equal to zero while all other terms remain unchanged. In the kMC framework, switching off one transport process will not necessarily decrease the total leakage current – since the competing channels are treated and computed individually, if one channel becomes unavailable to the charge carrier they will be most certainly redirected over the remaining channels, for which the transition rates are recomputed, resulting maybe in a comparable total current.

Also the local contribution of the specific defect states, inside the dielectric, to the total current cannot be evaluated, since only the kMC approach simulates the real trajectories of charge carriers through the defect rich dielectric. In the case of lower quality films, with increased RMS roughness, such local effects could have a serious impact, especially for defect states located near to the rough electrode – which would then have an increased tunneling probability.

Nevertheless, we think that this bottom up approach, going from highly physical simulations, capable of predicting the electrical behavior of the samples under study – but also very time and resource consuming – to a more general, but fast and efficient DD model is a good strategy for the feasibility study of future material systems. A unique combination of relevant information about the

physical processes governing the new devices, but also about their readiness for use in real applications, can be gained.

To conclude, the results presented in this study confirmed our belief that oxygen vacancies inside the STO film are responsible for the undesired leaky behavior, but also helped us demonstrate that under certain assumptions the SRO/STO/SRO capacitors can be an attractive high-*k* alternative to other established materials like SiO_2 or HfO_2.

We have shown until now results obtained within our coupled kMC-DD framework, which can deliver useful insights of the physical processes inside responsible for unwanted, large leakage currents in novel high-*k* material systems. Also feasibility studies can be performed on realistic device architectures, paving the way for virtual prototyping and reduction of the learn curve for process engineers.

However, we think that our developed framework could do also a lot more after some minor modifications. Besides simulating the leakage current vs. voltage characteristic for the samples of interest and giving valuable information on the reasons thereof, reliability and degradation are also two other important aspects when considering the implementation of new electronic devices.

Recently Larcher *et al.* have published a few simulation studies that explain the defect formation and performance degradation in HfO_x memory devices, but also clarify the physics of the switching mechanism in the high-*k* resistive RAMs. Inspired by this work and having the inelastic, phonon assisted tunneling processes already implemented in our framework, the next logical step would be to record this power dissipation – that will eventually lead to a temperature increase in the dielectric layer – and add the (temperature activated) defect formation process to the already existing physical mechanisms in our kMC simulator. Reliability and device degradation after repeated read/write cycles could thus be further studied and optimization strategies explored.

Furthermore, a coupling of the two frameworks could be imagined in the midterm future. The MC simulations would not be delivering only physical input data to the commercial TCAD environment; instead a real-time coupling of the two codes could be achieved e.g. through the Sentaurus Physical Model Interface. This feature enables users to define custom physical models and

include them in standard DD simulations. Local effects of TAT could be thus included, by modifying the generation-recombination terms of specific mesh vertices – to account for the local elastic/inelastic tunneling of charge carriers into trap states located in the vicinity of those vertices.

Following the idea of a close coupling between the two approaches, a final implementation could be achieved after the above mentioned steps will be followed, namely: the calculation and inclusion of the local kMC trap to trap tunneling rates also for the gate/channel region of the DRAM pass transistor. Thus the whole DRAM device could be modeled and simulated in a realistic, 3D geometry, as presented in Chapter 4, but solving self-consistently the complex tunneling behavior with our kMC framework in the areas of interest – the deep trench capacitor and channel region of the NMOS and importing them in real time during the DD simulation.

Bibliography

[1] G. E. Moore, "Cramming more components onto integrated circuits," *Electronics*, vol. 38, no. 8, pp. 114–117, 1965.

[2] J. Czochralski, "Ein neues Verfahren zur Messung der Kristallisationsgeschwindigkeit der Metalle," *Zeitschrift für Physikalische Chemie*, vol. 92, no. 1, pp. 219–221, 1918.

[3] W. A. Pliskin and H. S. Lehman, "Structural Evaluation of Silicon Oxide Films," *Journal of The Electrochemical Society*, vol. 112, no. 10, pp. 1013–1019, 1965.

[4] M. Armacost, A. Augustin, P. Felsner, Y. Feng, G. Friese, J. Heidenreich, G. Hueckel, O. Prigge, and K. Stein, "A high reliability metal insulator metal capacitor for 0.18 /spl mu/m copper technology," in *Electron Devices Meeting, 2000. IEDM '00. Technical Digest. International*, Dec 2000, pp. 157–160.

[5] P. Zurcher, P. Alluri, P. Chu, A. Duvallet, C. Happ, R. Henderson, J. Mendonca, M. Kim, M. Petras, M. Raymond, T. Remmel, D. Roberts, B. Steimle, J. Stipanuk, S. Straub, T. Sparks, M. Tarabbia, H. Thibieroz, and M. Miller, "Integration of thin film MIM capacitors and resistors into copper metallization based RF-CMOS and Bi-CMOS technologies," in *Electron Devices Meeting, 2000. IEDM '00. Technical Digest. International*, Dec 2000, pp. 153–156.

[6] Z. X. He, D. Daley, R. Bolam, D. Vanslette, F. Chen, E. Cooney, D. Mosher, N. Feilchenfeld, K. Newton, E. Eshun, R. Rassel, J. Benoit, D. Coolbaugh, S. St Onge, and J. Dunn, "High and low density complimentary MIM capacitors fabricated simultaneously in advanced RFCMOS and BiCMOS

technologies," in *Bipolar/BiCMOS Circuits and Technology Meeting, 2008. BCTM 2008. IEEE*, Oct 2008, pp. 212–215.

[7] R. Bolam, V. Ramachandran, D. Coolbaugh, and K. Watson, "Electrical characteristics and reliability of UV transparent Si3N4 metal-insulator-metal (MIM) capacitors," *Electron Devices, IEEE Transactions on*, vol. 50, no. 4, pp. 941–944, April 2003.

[8] D. Cheskis, "IC technologies for mixed-signal and RF SIP," *Solid State Technology*, vol. 50, no. 4, pp. 46–47, April 2007.

[9] K. Kim, "Perspectives on giga-bit scaled DRAM technology generation," *Microelectronics Reliability*, vol. 40, no. 2, pp. 191–206, 2000.

[10] M. Thomas, A. Farcy, N. Gaillard, C. Perrot, M. Gros-Jean, I. Matko, M. Cordeau, W. Saikaly, M. Proust, P. Caubet, E. Deloffre, S. Crémer, S. Bruyère, B. Chenevier, and J. Torres, "Integration of a high density Ta2O5 MIM capacitor following 3D damascene architecture compatible with copper interconnects," *Microelectronic Engineering*, vol. 83, no. 11–12, pp. 2163 – 2168, 2006, materials for Advanced Metallization (MAM 2006).

[11] K. Boucart and A. Ionescu, "Double-Gate Tunnel FET With High-k Gate Dielectric," *Electron Devices, IEEE Transactions on*, vol. 54, no. 7, pp. 1725–1733, July 2007.

[12] "Available online: http://www.itrs.net."

[13] V. Narayanan, S. Guha, M. Copel, N. Bojarczuk, P. Flaitz, and M. Gribelyuk, "Interfacial oxide formation and oxygen diffusion in rare earth oxide-silicon epitaxial heterostructures," *Applied Physics Letters*, vol. 81, no. 22, pp. 4183–4185, Nov 2002.

[14] M. V. Fischetti, D. A. Neumayer, and E. A. Cartier, "Effective electron mobility in Si inversion layers in metal–oxide–semiconductor systems with a high- insulator: The role of remote phonon scattering," *Journal of Applied Physics*, vol. 90, no. 9, pp. 4587–4608, 2001.

[15] K. Shiraishi, K. Yamada, K. Torii, Y. Akasaka, K. Nakajima, M. Kohno, T. Chikyo, H. Kitajima, and T. Arikado, "Physics in Fermi level pinning

at the polySi/Hf-based high-k oxide interface," in *VLSI Technology, 2004. Digest of Technical Papers. 2004 Symposium on*, June 2004, pp. 108–109.

[16] K. Tse and J. Robertson, "Defect passivation in HfO2 gate oxide by fluorine," *Applied Physics Letters*, vol. 89, no. 14, pp. –, 2006.

[17] G. D. Wilk and D. A. Muller, "Correlation of annealing effects on local electronic structure and macroscopic electrical properties for HfO2 deposited by atomic layer deposition," *Applied Physics Letters*, vol. 83, no. 19, pp. 3984–3986, 2003.

[18] J. Kittl, K. Opsomer, M. Popovici, N. Menou, B. Kaczer, X. Wang, C. Adelmann, M. Pawlak, K. Tomida, A. Rothschild, B. Govoreanu, R. Degraeve, M. Schaekers, M. Zahid, A. Delabie, J. Meersschaut, W. Polspoel, S. Clima, G. Pourtois, W. Knaepen, C. Detavernier, V. Afanas'ev, T. Blomberg, D. Pierreux, J. Swerts, P. Fischer, J. Maes, D. Manger, W. Vandervorst, T. Conard, A. Franquet, P. Favia, H. Bender, B. Brijs, S. Van Elshocht, M. Jurczak, J. Van Houdt, and D. Wouters, "High-k dielectrics for future generation memory devices (Invited Paper)," *MICROELECTRONIC ENGINEERING*, vol. 86, no. 7-9, pp. 1789–1795, 2009.

[19] S. Monaghan, K. Cherkaoui, E. O'Connor, V. Djara, P. Hurley, L. Oberbeck, E. Tois, L. Wilde, and S. Teichert, "TiN/ZrO2 /Ti/Al Metal/Insulator/Metal Capacitors With Subnanometer CET Using ALD-Deposited ZrO2 for DRAM Applications," *Electron Device Letters, IEEE*, vol. 30, no. 3, pp. 219–221, March 2009.

[20] H. J. Cho, Y. D. Kim, D. S. Park, E. Lee, C. H. Park, J. S. Jang, K. B. Lee, H. W. Kim, S. J. Chae, Y. J. Ki, I. K. Han, and Y. W. Song, "New TIT Capacitor with ZrO2/Al2O3/ZrO2 dielectrics for 60nm and below DRAMs," in *Solid-State Device Research Conference, 2006. ESSDERC 2006. Proceeding of the 36th European*, Sept 2006, pp. 146–149.

[21] K. Mistry, C. Allen, C. Auth, B. Beattie, D. Bergstrom, M. Bost, M. Brazier, M. Buehler, A. Cappellani, R. Chau, C.-H. Choi, G. Ding, K. Fischer, T. Ghani, R. Grover, W. Han, D. Hanken, M. Hattendorf, J. He, J. Hicks, R. Huessner, D. Ingerly, P. Jain, R. James, L. Jong, S. Joshi, C. Kenyon, K. Kuhn, K. Lee, H. Liu, J. Maiz, B. Mcintyre, P. Moon, J. Neirynck,

S. Pae, C. Parker, D. Parsons, C. Prasad, L. Pipes, M. Prince, P. Ranade, T. Reynolds, J. Sandford, L. Shifren, J. Sebastian, J. Seiple, D. Simon, S. Sivakumar, P. Smith, C. Thomas, T. Troeger, P. Vandervoorn, S. Williams, and K. Zawadzki, "A 45nm Logic Technology with High-k+Metal Gate Transistors, Strained Silicon, 9 Cu Interconnect Layers, 193nm Dry Patterning, and 100 Pb-free Packaging," in *Electron Devices Meeting, 2007. IEDM 2007. IEEE International*, Dec 2007, pp. 247–250.

[22] S. W. Lee, O. S. Kwon, J. H. Han, and C. S. Hwang, "Enhanced electrical properties of SrTiO3 thin films grown by atomic layer deposition at high temperature for dynamic random access memory applications," *Applied Physics Letters*, vol. 92, no. 22, pp. –, 2008.

[23] W. Lee, J. H. Han, W. Jeon, Y. W. Yoo, S. W. Lee, S. K. Kim, C.-H. Ko, C. Lansalot-Matras, and C. S. Hwang, "Atomic Layer Deposition of SrTiO3 Films with Cyclopentadienyl-Based Precursors for Metal–Insulator–Metal Capacitors," *Chemistry of Materials*, vol. 25, no. 6, pp. 953–961, 2013.

[24] S. Schmelzer, D. Brauhaus, S. Hoffmann-Eifert, P. Meuffels, U. Bottger, L. Oberbeck, P. Reinig, U. Schroder, and R. Waser, "SrTiO3 thin film capacitors on silicon substrates with insignificant interfacial passive layers," *Applied Physics Letters*, vol. 97, no. 13, pp. 132 907–132 907–3, Sep 2010.

[25] S. Schmidt, J. Lu, S. P. Keane, L. D. Bregante, D. O. Klenov, and S. Stemmer, "Microstructure and Dielectric Properties of Textured SrTiO3 Thin Films," *Journal of the American Ceramic Society*, vol. 88, no. 4, pp. 789–801, 2005.

[26] M. S. Tsai, S. C. Sun, and T.-Y. Tseng, "Effect of bottom electrode materials on the electrical and reliability characteristics of (Ba, Sr)TiO3 capacitors," *Electron Devices, IEEE Transactions on*, vol. 46, no. 9, pp. 1829–1838, Sep 1999.

[27] G. W. Dietz, W. Antpöhler, M. Klee, and R. Waser, "Electrode influence on the charge transport through SrTiO3 thin films," *Journal of Applied Physics*, vol. 78, no. 10, pp. 6113–6121, 1995.

[28] J. H. Han, W. Lee, W. Jeon, S. W. Lee, C. S. Hwang, C. Ko, and J. Gatineau, "Growth of Conductive SrRuO3 Films by Combining Atomic Layer De-

posited SrO and Chemical Vapor Deposited RuO2 Layers," *Chemistry of Materials*, vol. 24, no. 24, pp. 4686–4692, 2012.

[29] R. Lake, G. Klimeck, R. C. Bowen, and D. Jovanovic, "Single and multiband modeling of quantum electron transport through layered semiconductor devices," *Journal of Applied Physics*, vol. 81, no. 12, pp. 7845–7869, 1997.

[30] M. Luisier, A. Schenk, and W. Fichtner, "Quantum transport in two-and three-dimensional nanoscale transistors: coupled mode effects in the nonequilibrium Green's function formalism," *Journal of applied physics*, vol. 100, no. 4, p. 043713, 2006.

[31] A. Asenov, A. R. Brown, G. Roy, B. Cheng, C. Alexander, C. Riddet, U. Kovac, A. Martinez, N. Seoane, and S. Roy, "Simulation of statistical variability in nano-CMOS transistors using drift-diffusion, Monte Carlo and non-equilibrium Green's function techniques," *Journal of computational electronics*, vol. 8, no. 3-4, pp. 349–373, 2009.

[32] C. Jacoboni and P. Lugli, *The Monte Carlo method for semiconductor device simulation*. Springer, 1989, vol. 3.

[33] M. V. Fischetti and S. E. Laux, "Monte Carlo analysis of electron transport in small semiconductor devices including band-structure and space-charge effects," *Physical Review B*, vol. 38, no. 14, p. 9721, 1988.

[34] P. D. Yoder, K. Gartner, U. Krumbein, and W. Fichtner, "Optimized terminal current calculation for Monte Carlo device simulation," *Computer-Aided Design of Integrated Circuits and Systems, IEEE Transactions on*, vol. 16, no. 10, pp. 1082–1087, 1997.

[35] G. Wachutka, "An extended thermodynamic model for the simultaneous simulation of the thermal and electrical behavior of semiconductor devices," in *Proc. Sixth Int. NASECODE Conf.* Boole Press Ltd, 1989, pp. 409–414.

[36] R. Stratton, "Diffusion of hot and cold electrons in semiconductor barriers," *Physical Review*, vol. 126, no. 6, p. 2002, 1962.

[37] Y. Apanovich, P. Blakey, R. Cottle, E. Lyumkis, B. Polsky, A. Shur, and A. Tcherniaev, "Numerical simulation of submicrometer devices including coupled nonlocal transport and nonisothermal effects," *Electron Devices, IEEE Transactions on*, vol. 42, no. 5, pp. 890–898, 1995.

[38] G. Jegert, A. Kersch, W. Weinreich, U. Schröder, and P. Lugli, "Modeling of leakage currents in high-k dielectrics: Three-dimensional approach via kinetic Monte Carlo," *Applied Physics Letters*, vol. 96, no. 6, pp. –, 2010.

[39] G. Jegert, A. Kersch, W. Weinreich, and P. Lugli, "Monte Carlo Simulation of Leakage Currents in Capacitors," *Electron Devices, IEEE Transactions on*, vol. 58, no. 2, pp. 327–334, Feb 2011.

[40] G. Jegert, D. Popescu, P. Lugli, M. J. Häufel, W. Weinreich, and A. Kersch, "Role of defect relaxation for trap-assisted tunneling in high-κ thin films: A first-principles kinetic Monte Carlo study," *Phys. Rev. B*, vol. 85, p. 045303, Jan 2012.

[41] K. S. I. Sveshnikova, G. S. and V. B. Aleskovskii, "Interaction of titanium tetrachloride with hydroxylated silicon surfaces," *J. Appl. Cem. USSR*, vol. 43, no. 2, pp. 432–434, 1970.

[42] V. B. Aleskovskii, "Matrix hypothesis and way of synthesis of some active solid compounds," *Doctoral thesis*, 1952.

[43] ——, "Chemistry and technology of solids," *J. Appl. Cem. USSR*, vol. 47, no. 10, pp. 2145–2157, 1974.

[44] H. Kattelus, H. Ronkainen, and T. Riihisaari, "Passive integration process on standard and high resistivity silicon," *The International Journal of Microcircuits and Electronic Packaging*, vol. 22, no. 3, pp. 254–261, Sept 1999.

[45] K. Ellis and R. Buhrman, "Time-dependent diffusivity of boron in silicon oxide and oxynitride," *Applied Physics Letters*, vol. 74, no. 7, pp. 967–969, Feb 1999.

[46] K. Kumar, A. I. Chou, C. Lin, P. Choudhury, J. C. Lee, and J. K. Lowell, "Optimization of sub 3 nm gate dielectrics grown by rapid thermal oxidation in a nitric oxide ambient," *Applied Physics Letters*, vol. 70, no. 3, pp. 384–386, 1997.

[47] M. Thomas, A. Farcy, N. Gaillard, C. Perrot, M. Gros-Jean, I. Matko, M. Cordeau, W. Saikaly, M. Proust, P. Caubet, E. Deloffre, S. Crémer, S. Bruyère, B. Chenevier, and J. Torres, "Integration of a high density Ta2O5 MIM capacitor following 3D damascene architecture compatible with copper interconnects," *Microelectronic Engineering*, vol. 83, no. 11–12, pp. 2163 – 2168, 2006, materials for Advanced Metallization (MAM 2006).

[48] Y. K. Park, Y. S. Ahn, S. B. Kim, K. H. Lee, C. H. Cho, T. Y. Chung, and K. Kim, "Effective Capacitance Enhancement Methods for 90-nm DRAM Capacitors," *Journal of the Korean Physical Society*, vol. 44, no. 1, pp. 112 – 116, 2004.

[49] J. Amon, A. Kieslich, L. Heineck, T. Schuster, J. Faul, J. Luetzen, C. Fan, C. Huang, B. Fischer, G. Enders *et al.*, "A highly manufacturable deep trench based DRAM cell layout with a planar array device in a 70nm technology," in *Electron Devices Meeting, 2004. IEDM Technical Digest. IEEE International*. IEEE, 2004, pp. 73–76.

[50] R. Courtland, "3-D transistors for all," *Spectrum, IEEE*, vol. 50, no. 1, pp. 11–12, Jan 2013.

[51] C. Auth, C. Allen, A. Blattner, D. Bergstrom, M. Brazier, M. Bost, M. Buehler, V. Chikarmane, T. Ghani, T. Glassman, R. Grover, W. Han, D. Hanken, M. Hattendorf, P. Hentges, R. Heussner, J. Hicks, D. Ingerly, P. Jain, S. Jaloviar, R. James, D. Jones, J. Jopling, S. Joshi, C. Kenyon, H. Liu, R. McFadden, B. Mcintyre, J. Neirynck, C. Parker, L. Pipes, I. Post, S. Pradhan, M. Prince, S. Ramey, T. Reynolds, J. Roesler, J. Sandford, J. Seiple, P. Smith, C. Thomas, D. Towner, T. Troeger, C. Weber, P. Yashar, K. Zawadzki, and K. Mistry, "A 22nm high performance and low-power CMOS technology featuring fully-depleted tri-gate transistors, self-aligned contacts and high density MIM capacitors," in *VLSI Technology (VLSIT), 2012 Symposium on*, June 2012, pp. 131–132.

[52] K. Seshan, *Handbook of Thin Film Deposition Processes and Techniques (Second Edition)*. William Andrew Publishing/Noyes, 2002.

[53] J. E. Crowell, "Chemical methods of thin film deposition: Chemical vapor deposition, atomic layer deposition, and related technologies," *Journal of Vacuum Science Technology A*, vol. 21, no. 5, pp. S88–S95, 2003.

[54] O. Sundaram, *Thin Film Techniques and Applications*. Allied Publishers: New Delphi, 2004.

[55] F. Vaz, N. Martin, and M. Fenker, *Metallic Oxynitride Thin Films by Reactive Sputtering and Related Deposition Methods: Processes, Properties and Applications*. Bentham Science Publishers, 2013.

[56] J. Hwan Han, W. Lee, S. W. Lee, and C. Seong Hwang, "Higher-k dielectrics and conductive oxide electrodes for next generation DRAMs with a design rule of 20 nm," pp. 1–2, Dec 2011.

[57] B. Kiyoo Itoh, "The History of DRAM Circuit Designs - At the Forefront of DRAM Development;," *Solid-State Circuits Society Newsletter, IEEE*, vol. 13, no. 1, pp. 27–31, Winter 2008.

[58] K. Itoh, M. Horiguchi, and H. Tanaka, *Ultra-Low Voltage Nano-Scale Memories*, ser. Integrated Circuits and Systems. Springer, 2007.

[59] "Available online: http://en.wikipedia.org/wiki/Dynamic-random-access-memory."

[60] D. W. Bruce Jacob, Spencer Ng, in *Memory Systems: Cache, DRAM, Disk*. Morgan Kaufmann, 2008.

[61] R. D. Adams, in *High Performance Memory Testing: Design Principles, Fault Modeling and Self-Test*. Springer, 2002.

[62] G. R. Ralph Stair, in *Principles of Information Systems*. Cengage Learning, 2013.

[63] G. He and Z. Sun, *High-k Gate Dielectrics for CMOS Technology*, ser. High-k Gate Dielectrics for CMOS Technology. Wiley, 2012.

[64] A. Shelykh and B. Melekh, "CeAlO3 crystals: Preparation and study of their electrical and optical characteristics," *Physics of the Solid State*, vol. 45, no. 2, pp. 248–252, 2003.

[65] Y.-I. Kim, P. M. Woodward, K. Z. Baba-Kishi, and C. W. Tai, "Characterization of the Structural, Optical, and Dielectric Properties of Oxynitride Perovskites AMO2N (A = Ba, Sr, Ca; M = Ta, Nb)," *Chemistry of Materials*, vol. 16, no. 7, pp. 1267–1276, 2004.

[66] T.-L. Ren, X.-N. Wang, J.-S. Liu, H.-J. Zhao, T.-Q. Shao, L.-T. Liu, and Z.-J. Li, "Characteristics of silicon-based BaxSr(1-x)TiO3 thin films prepared by a sol-gel method," *Journal of Physics D: Applied Physics*, vol. 35, no. 9, p. 923, 2002.

[67] A. Hushur, G. Shabbir, J.-H. Ko, and S. Kojima, "The phase transitions of ferroelectric Sr2Ta2O7 crystals by MDSC, Brillouin and dielectric spectroscopy," *Journal of Physics D: Applied Physics*, vol. 37, no. 7, p. 1127, 2004.

[68] L. Goux, H. Vander Meeren, and D. J. Wouters, "Metallorganic Chemical Vapor Deposition of Sr-Ta-O and Bi-Ta-O Films for Backend Integration of High-k Capacitors," *Journal of The Electrochemical Society*, vol. 153, no. 7, pp. F132–F136, 2006.

[69] D. Popescu, B. Popescu, G. Jegert, S. Schmelzer, U. Boettger, and P. Lugli, "Feasibility Study of SrRuO/SrTiO3/SrRuO3 Thin Film Capacitors in DRAM Applications," *Electron Devices, IEEE Transactions on*, vol. 61, no. 6, pp. 2130–2135, June 2014.

[70] S. Schmidt, J. Lu, S. P. Keane, L. D. Bregante, D. O. Klenov, and S. Stemmer, "Microstructure and Dielectric Properties of Textured SrTiO3 Thin Films," *Journal of the American Ceramic Society*, vol. 88, no. 4, pp. 789–801, 2005.

[71] M. S. Tsai, S. C. Sun, and T.-Y. Tseng, "Effect of bottom electrode materials on the electrical and reliability characteristics of (Ba, Sr)TiO3 capacitors," *Electron Devices, IEEE Transactions on*, vol. 46, no. 9, pp. 1829–1838, Sep 1999.

[72] G. W. Dietz, W. Antpöhler, M. Klee, and R. Waser, "Electrode influence on the charge transport through SrTiO3 thin films," *Journal of Applied Physics*, vol. 78, no. 10, pp. 6113–6121, 1995.

[73] M. Pawlak, J. Swerts, M. Popovici, B. Kaczer, M. S. Kim, W. C. Wang, K. Tomida, B. Govoreanu, J. Delmotte, V. Afanasev, M. Schaekers, W. Vandervorst, and J. Kittl, "Direct physical evidence of mechanisms of leakage and equivalent oxide thickness reduction in metal-insulator-metal capacitors based on RuOx/TiOx/SrxTiyOz/TiN stacks," *Applied Physics Letters*, vol. 101, no. 4, pp. 042 901–042 901–3, Jul 2012.

[74] F. Pontes, E. Lee, E. Leite, E. Longo, and J. Varela, "High dielectric constant of SrTiO3 thin films prepared by chemical process," *Journal of Materials Science*, vol. 35, no. 19, pp. 4783–4787, 2000.

[75] W. Hofman, S. Hoffmann, and R. Waser, "Dopant influence on dielectric losses, leakage behaviour, and resistance degradation of SrTiO3 thin films," *Thin Solid Films*, vol. 305, no. 1–2, pp. 66 – 73, 1997.

[76] K. C. Chiang, J. W. Lin, H. C. Pan, C. N. Hsiao, W. J. Chen, H. L. Kao, I. J. Hsieh, and A. Chin, "Very High Density (44 fFm2) SrTiO3 MIM Capacitors for RF Applications," *Journal of The Electrochemical Society*, vol. 154, no. 3, pp. H214–H216, 2007.

[77] W. Wang, N. Gu, J. Sun, and P. Mazumder, "Gate current modeling of high-k stack nanoscale MOSFETs," *Solid-State Electronics*, vol. 50, no. 9–10, pp. 1489 – 1494, 2006.

[78] S. Goswami and A. Biswas, "Modeling and numerical simulation of gate leakage current in strained-Si channel nMOSFETs with highk gate dielectrics," in *Emerging Trends in Grown on Ru Electrode by Atomic and Photonic Devices Systems, 2009. ELECTRO '09. International Conference on*. IEEE, 2009, pp. 33–36.

[79] M.-T. Wang, T.-H. Wang, and J. Y.-m. Lee, "Electrical Conduction Mechanism in Metal- ZrO2-Silicon Capacitor Structures," *Journal of The Electrochemical Society*, vol. 152, no. 3, pp. G182–G185, 2005.

[80] Z. Xu, M. Houssa, S. De Gendt, and M. Heyns, "Polarity effect on the temperature dependence of leakage current through HfO2/SiO2 gate dielectric stacks," *Applied Physics Letters*, vol. 80, no. 11, pp. 1975–1977, 2002.

[81] D. S. Jeong and C. S. Hwang, "Tunneling-assisted Poole-Frenkel conduction mechanism in HfO2 thin films," *Journal of Applied Physics*, vol. 98, no. 11, pp. –, 2005.

[82] O. Blank, H. Reisinger, R. Stengl, M. Gutsche, F. Wiest, V. Capodieci, J. Schulze, and I. Eisele, "A model for multistep trap-assisted tunneling in thin high-k dielectrics," *Journal of applied physics*, vol. 97, no. 4, pp. 044 107–044 107, 2005.

[83] H. Schroeder, S. Schmitz, and P. Meuffels, "Leakage currents in high-permittivity thin films," *Applied Physics Letters*, vol. 82, no. 5, pp. 781–783, 2003.

[84] S. W. Lee, J. H. Han, and C. S. Hwang, "Electronic conduction mechanism of SrTiO3 thin film grown on Ru electrode by atomic layer deposition," *Electrochemical and Solid-State Letters*, vol. 12, no. 11, pp. G69–G71, 2009.

[85] B. Kaczer, S. Clima, K. Tomida, B. Govoreanu, M. Popovici, M.-S. Kim, J. Swerts, A. Belmonte, W.-C. Wang, V. V. Afanasapos;ev, A. S. Verhulst, G. Pourtois, G. Groeseneken, and M. Jurczak, "Considerations for further scaling of metal–insulator–metal DRAM capacitors," *Journal of Vacuum Science Technology B*, vol. 31, no. 1, pp. –, 2013.

[86] D. Manger, B. Kaczer, N. Menou, S. Clima, D. Wouters, V. Afanas'ev, and J. Kittl, "Comprehensive investigation of trap-assisted conduction in ultra-thin SrTiO3 layers," *Microelectronic Engineering*, vol. 86, no. 7–9, pp. 1815 – 1817, 2009, {INFOS} 2009.

[87] Y. Okuyama, S. Kamohara, Y. Manabe, K. Okuyama, Y. Kubota, T. Kobayashi, and K. Kimura, "Monte Carlo simulation of stress-induced leakage current by hopping conduction via multi-traps in oxide," in *Electron Devices Meeting, 1998. IEDM '98. Technical Digest., International*. IEEE, Dec 1998, pp. 905–908.

[88] L. Vandelli, A. Padovani, L. Larcher, R. Southwick, W. Knowlton, and G. Bersuker, "A Physical Model of the Temperature Dependence of the Current Through Stacks," *Electron Devices, IEEE Transactions on*, vol. 58, no. 9, pp. 2878–2887, 2011.

[89] B. Borrell, "Power play," *Nature*, vol. 451, no. 7176, pp. 240–243, 2008.

[90] H. Watanabe, M. Suzuki, and N. Ito, "Huge-scale molecular dynamics simulation of multibubble nuclei," *Computer Physics Communications*, vol. 184, no. 12, pp. 2775 – 2784, 2013.

[91] P. Kelires and J. Tersoff, "Equilibrium alloy properties by direct simulation: Oscillatory segregation at the Si-Ge (100) $2\times$ 1 surface," *Physical review letters*, vol. 63, no. 11, p. 1164, 1989.

[92] J. Tersoff, "Enhanced solubility of impurities and enhanced diffusion near crystal surfaces," *Physical review letters*, vol. 74, no. 25, p. 5080, 1995.

[93] N. Metropolis and S. Ulam, "The Monte Carlo Method," *Journal of the American Statistical Association*, vol. 44, no. 247, pp. pp. 335–341, 1949.

[94] N. Metropolis, A. Rosenbluth, M. Rosenbluth, A. Teller, and E. Teller, "Equation of State Calculations by Fast Computing Machines," *The Journal of Chemical Physics*, vol. 21, no. 6, pp. 1087–1092, 1953.

[95] P. A. Flinn and G. M. McManus, "Monte Carlo Calculation of the Order-Disorder Transformation in the Body-Centered Cubic Lattice," *Phys. Rev.*, vol. 124, pp. 54–59, Oct 1961.

[96] W. M. Young and E. W. Elcock, "Monte Carlo studies of vacancy migration in binary ordered alloys: I," *Proceedings of the Physical Society*, vol. 89, no. 3, p. 735, 1966.

[97] A. B. Bortz, M. Kalos, and J. Lebowitz, "A New Algorithm for Monte Carlo Simulation of Ising Spin Systems," *The Journal of Computational Physics*, vol. 17, no. 6, pp. 10–18, 1975.

[98] J. R. Beeler, "Displacement Spikes in Cubic Metals. I. α-Iron, Copper, and Tungsten," *Phys. Rev.*, vol. 150, pp. 470–487, Oct 1966.

[99] D. G. Doran, "Computer simulation of displacement spike annealing," *Radiation Effects*, vol. 2, no. 4, pp. 249–267, 1970.

[100] H. L. Heinisch, "Defect production in simulated cascades: Cascade quenching and short term annealing," *J. Nucl. Mater.*, vol. 117, pp. 46–54, 1983.

[101] A. F. Voter, "Classically exact overlayer dynamics: Diffusion of rhodium clusters on Rh (100)," *Physical Review B*, vol. 34, no. 10, p. 6819, 1986.

[102] C. Kohli and M. Ives, "Computer simulation of crystal dissolution morphology," *Journal of Crystal Growth*, vol. 16, no. 2, pp. 123 – 130, 1972.

[103] F. Abraham and G. White, "Computer simulation of vapor deposition on two-dimensional lattices," *J. Appl. Phys.*, vol. 41, pp. 1841–1849, 1970.

[104] E. S. Hood, B. H. Toby, and W. Weinberg, "Precursor-mediated molecular chemisorption and thermal desorption: The interrelationships among energetics, kinetics, and adsorbate lattice structure," *Physical review letters*, vol. 55, no. 22, p. 2437, 1985.

[105] D. A. Reed and G. Ehrlich, "Surface diffusivity and the time correlation of concentration fluctuations," *Surface Science*, vol. 105, no. 2, pp. 603–628, 1981.

[106] G. H. Gilmer, "Computer simulation of crystal growth," *Journal of Crystal Growth*, vol. 42, pp. 3–10, 1977.

[107] K. A. Fichthorn and W. H. Weinberg, "Theoretical foundations of dynamical Monte Carlo simulations," *The Journal of chemical physics*, vol. 95, no. 2, pp. 1090–1096, 1991.

[108] D. T. Gillespie, "A general method for numerically simulating the stochastic time evolution of coupled chemical reactions," *Journal of computational physics*, vol. 22, no. 4, pp. 403–434, 1976.

[109] ——, "Exact stochastic simulation of coupled chemical reactions," *The journal of physical chemistry*, vol. 81, no. 25, pp. 2340–2361, 1977.

[110] D. A. McQuarrie, "Stochastic Approach to Chemical Kinetics," *Journal of Applied Probability*, vol. 4, no. 3, pp. pp. 413–478, 1967.

[111] D. T. Gillespie, "The Monte Carlo method of evaluating integrals," DTIC Document, Tech. Rep., 1975.

[112] "Available online: http://www.synopsys.com/tools/tcad/Pages/default.aspx."

[113] X. Wang, X. Lu, C. Zhang, X. Wu, W. Cai, S. Peng, H. Bo, Y. Kan, F. Huang, and J. Zhu, "Oxygen-vacancy-related high-temperature dielectric relaxation in SrTiO3 ceramics," *Journal of Applied Physics*, vol. 107, no. 11, p. 114101, 2010.

[114] C. Wang, C. Lei, G. Wang, X. Sun, T. Li, S. Huang, H. Wang, and Y. Li, "Oxygen-vacancy-related dielectric relaxations in SrTiO3 at high temperatures," *Journal of Applied Physics*, vol. 113, no. 9, p. 094103, 2013.

[115] V. E. Alexandrov, E. A. Kotomin, J. Maier, and R. A. Evarestov, "First-principles study of bulk and surface oxygen vacancies in SrTiO3 crystal," *The European Physical Journal B*, vol. 72, no. 1, pp. 53–57, 2009.

[116] M. Ieong, P. M. Solomon, S. Laux, H.-S. Wong, and D. Chidambarrao, "Comparison of raised and Schottky source/drain MOSFETs using a novel tunneling contact model," in *Electron Devices Meeting, 1998. IEDM'98. Technical Digest., International*. IEEE, 1998, pp. 733–736.

[117] F. L. Mudanai, S. Y.-Y. F. Register, and S. LF Banerjee, "Compact model of MOSFET electron tunneling current through ultra-thin SiO2 and high-k gate stacks." Device Research Conference, 2003, 2003.

[118] S. Makram-Ebeid and M. Lannoo, "Quantum model for phonon-assisted tunnel ionization of deep levels in a semiconductor," *Physical Review B*, vol. 25, no. 10, p. 6406, 1982.

[119] L. Colalongo, M. Valdinoci, G. Baccarani, P. Migliorato, G. Tallarida, and C. Reita, "Numerical analysis of poly-TFTs under off conditions," *Solid-State Electronics*, vol. 41, no. 4, pp. 627–633, 1997.

[120] *Sentaurus Device User Guide*. Synopsys, March 3013, vol. Version H-2013.03.

[121] P. George and H. Borouchaki, *Delaunay Triangulation and Meshing: Application to Finite Elements*. Butterworth-Heinemann, 1998.

[122] S. H. Jeon, B. H. Park, J. Lee, B. Lee, and S. Han, "First-principles modeling of resistance switching in perovskite oxide material," *Applied Physics Letters*, vol. 89, no. 4, pp. –, 2006.

[123] R. E. Bank, D. J. Rose, and W. Fichtner, "Numerical methods for semiconductor device simulation," *Electron Devices, IEEE Transactions on*, vol. 30, no. 9, pp. 1031–1041, 1983.

[124] G. Wang, D. Anand, N. Butt, A. Cestero, M. Chudzik, J. Ervin, S. Fang, G. Freeman, H. Ho, B. Khan *et al.*, "Scaling deep trench based eDRAM on SOI to 32nm and Beyond," in *Electron Devices Meeting (IEDM), 2009 IEEE International*. IEEE, 2009, pp. 1–4.

[125] J. G. Fossum, "Computer-aided numerical analysis of silicon solar cells," *Solid-State Electronics*, vol. 19, no. 4, pp. 269–277, 1976.

[126] J. Fossum and D. Lee, "A physical model for the dependence of carrier lifetime on doping density in nondegenerate silicon," *Solid-State Electronics*, vol. 25, no. 8, pp. 741–747, 1982.

[127] D. Roulston, N. Arora, and S. G. Chamberlain, "Modeling and measurement of minority-carrier lifetime versus doping in diffused layers of n+-p silicon diodes," *Electron Devices, IEEE Transactions on*, vol. 29, no. 2, pp. 284–291, 1982.

[128] G. Masetti, M. Severi, and S. Solmi, "Modeling of carrier mobility against carrier concentration in arsenic-, phosphorus-, and boron-doped silicon," *Electron Devices, IEEE Transactions on*, vol. 30, no. 7, pp. 764–769, 1983.

[129] C. Canali, G. Majni, R. Minder, and G. Ottaviani, "Electron and hole drift velocity measurements in silicon and their empirical relation to electric field and temperature," *Electron Devices, IEEE Transactions on*, vol. 22, no. 11, pp. 1045–1047, 1975.

[130] C. Lombardi, S. Manzini, A. Saporito, and M. Vanzi, "A physically based mobility model for numerical simulation of nonplanar devices," *Computer-Aided Design of Integrated Circuits and Systems, IEEE Transactions on*, vol. 7, no. 11, pp. 1164–1171, 1988.

[131] M. Ancona and H. Tiersten, "Macroscopic physics of the silicon inversion layer," *Physical Review B*, vol. 35, no. 15, p. 7959, 1987.

[132] M. Ancona and G. Iafrate, "Quantum correction to the equation of state of an electron gas in a semiconductor," *Physical Review B*, vol. 39, no. 13, p. 9536, 1989.

[133] R. Tsu and L. Esaki, "Tunneling in a finite superlattice," *Applied Physics Letters*, vol. 22, no. 11, pp. 562–564, 1973.

[134] D. Ferry, S. Goodnick, and J. Bird, *Transport in Nanostructures*, ser. Transport in Nanostructures. Cambridge University Press, 2009.

[135] V. Magnasco, *Elementary Methods of Molecular Quantum Mechanics*. Elsevier Science, 2006.

[136] I. Lundström and C. Svensson, "Tunneling to traps in insulators," *Journal of Applied Physics*, vol. 43, no. 12, pp. 5045–5047, 1972.

[137] L. Lundkvist, I. Lundström, and C. Svensson, "Discharge of MNOS structures," *Solid-State Electronics*, vol. 16, no. 7, pp. 811–IN1, 1973.

[138] M. Herrmann and A. Schenk, "Field and high-temperature dependence of the long term charge loss in erasable programmable read only memories: Measurements and modeling," *Journal of applied physics*, vol. 77, no. 9, pp. 4522–4540, 1995.

[139] G. Lucovsky, "On the photoionization of deep impurity centers in semiconductors," *Solid State Communications*, vol. 3, no. 9, pp. 299–302, 1965.

[140] N. F. Mott, in *Advances in Solid State Physics 33*. Ed. Akademie-Verlag, 1969, vol. 9.

[141] B. K. Ridley, "On the multiphonon capture rate in semiconductors," *Solid-State Electronics*, vol. 21, no. 11–12, pp. 1319 – 1323, 1978.

[142] J. Frenkel, "On pre-breakdown phenomena in insulators and electronic semi-conductors," *Physical Review*, vol. 54, no. 8, p. 647, 1938.

[143] J. Hartke, "The Three-Dimensional Poole-Frenkel Effect," *Journal of Applied Physics*, vol. 39, no. 10, pp. 4871–4873, 1968.

[144] M. A. Pawlak, B. Kaczer, M.-S. Kim, M. Popovici, J. Swerts, W.-C. Wang, K. Opsomer, P. Favia, K. Tomida, A. Belmonte, B. Govoreanu, C. Vrancken, C. Demeurisse, H. Bender, V. V. Afanas'ev, I. Debusschere, L. Altimime, and J. A. Kittl, "Impact of bottom electrode and SrxTiyOz film formation on physical and electrical properties of metal-insulator-metal capacitors," *Applied Physics Letters*, vol. 98, no. 18, pp. –, 2011.

[145] D. Fuchs, C. W. Schneider, R. Schneider, and H. Rietschel, "High dielectric constant and tunability of epitaxial SrTiO3 thin film capacitors," *Journal of Applied Physics*, vol. 85, no. 10, pp. 7362–7369, 1999.

[146] A. F. Devonshire, "XCVI. Theory of barium titanate: Part I," *Philosophical Magazine*, vol. 40, no. 309, pp. 1040–1063, 1949.

[147] D. Popescu, B. Popescu, G. Jegert, S. Schmelzer, U. Boettger, and P. Lugli, "Kinetic Monte Carlo Simulation of $SrRuO_3/SrTiO_3/SrRuO_3$ Thin Film Capacitors," *Electron Devices, IEEE Transactions on*, SUBMITTED.

[148] "Available online: http://www.dealii.org/."

[149] N. Menou, M. Popovici, K. Opsomer, B. Kaczer, M. A. Pawlak, C. Adelmann, A. Franquet, P. Favia, H. Bender, C. Detavernier, S. V. Elshocht, D. J. Wouters, S. Biesemans, and J. A. Kittl, "Seed Layer and Multistack Approaches to Reduce Leakage in SrTiO 3 -Based Metal–Insulator–Metal Capacitors Using TiN Bottom Electrode," *Japanese Journal of Applied Physics*, vol. 49, no. 4S, p. 04DD01, 2010.

[150] G. Yu, J. Gao, J. Hummelen, F. Wudl, and A. Heeger, "Polymer photovoltaic cells: enhanced efficiencies via a network of internal donor-acceptor heterojunctions," *Science-AAAS-Weekly Paper Edition*, vol. 270, no. 5243, pp. 1789–1790, 1995.

[151] G. Dennler, M. C. Scharber, and C. J. Brabec, "Polymer-Fullerene Bulk-Heterojunction Solar Cells," *Advanced Materials*, vol. 21, no. 13, pp. 1323–1338, 2009.

[152] R. Gaudiana and C. Brabec, "Organic materials: Fantastic plastic," *Nature Photonics*, vol. 2, no. 5, pp. 287–289, 2008.

[153] H.-Y. Chen, J. Hou, S. Zhang, Y. Liang, G. Yang, Y. Yang, L. Yu, Y. Wu, and G. Li, "Polymer solar cells with enhanced open-circuit voltage and efficiency," *Nature Photonics*, vol. 3, no. 11, pp. 649–653, 2009.

[154] Y. Liang, Z. Xu, J. Xia, S.-T. Tsai, Y. Wu, G. Li, C. Ray, and L. Yu, "For the bright future—bulk heterojunction polymer solar cells with power conversion efficiency of 7.4%," *Advanced Materials*, vol. 22, no. 20, pp. E135–E138, 2010.

[155] T.-Y. Chu, J. Lu, S. Beaupré, Y. Zhang, J.-R. Pouliot, S. Wakim, J. Zhou, M. Leclerc, Z. Li, J. Ding *et al.*, "Bulk heterojunction solar cells using thieno [3, 4-c] pyrrole-4, 6-dione and dithieno [3, 2-b: 2, 3-d] silole copolymer with a power conversion efficiency of 7.3%," *Journal of the American Chemical Society*, vol. 133, no. 12, pp. 4250–4253, 2011.

[156] H. Zhou, L. Yang, A. C. Stuart, S. C. Price, S. Liu, and W. You, "Development of fluorinated benzothiadiazole as a structural unit for a polymer solar cell of 7% efficiency," *Angewandte Chemie*, vol. 123, no. 13, pp. 3051–3054, 2011.

[157] J. You, L. Dou, K. Yoshimura, T. Kato, K. Ohya, T. Moriarty, K. Emery, C.-C. Chen, J. Gao, G. Li *et al.*, "A polymer tandem solar cell with 10.6% power conversion efficiency," *Nature communications*, vol. 4, p. 1446, 2013.

[158] M. D. Irwin, D. B. Buchholz, A. W. Hains, R. P. Chang, and T. J. Marks, "p-Type semiconducting nickel oxide as an efficiency-enhancing anode interfacial layer in polymer bulk-heterojunction solar cells," *Proceedings of the National Academy of Sciences*, vol. 105, no. 8, pp. 2783–2787, 2008.

[159] W. Ma, C. Yang, X. Gong, K. Lee, and A. J. Heeger, "Thermally stable, efficient polymer solar cells with nanoscale control of the interpenetrating network morphology," *Advanced Functional Materials*, vol. 15, no. 10, pp. 1617–1622, 2005.

[160] V. Vohra, G. Arrighetti, L. Barba, K. Higashimine, W. Porzio, and H. Murata, "Enhanced Vertical Concentration Gradient in Rubbed P3HT: PCBM Graded Bilayer Solar Cells," *The Journal of Physical Chemistry Letters*, vol. 3, no. 13, pp. 1820–1823, 2012.

[161] "Available online: http://www.nrel.gov/."

[162] B. Ries and H. Bässler, "Monte Carlo study of dispersive charge-carrier transport in spatially random systems with and without energetic disorder," *Physical Review B*, vol. 35, no. 5, p. 2295, 1987.

[163] P. K. Watkins, A. B. Walker, and G. L. Verschoor, "Dynamical Monte Carlo modelling of organic solar cells: The dependence of internal quantum efficiency on morphology," *Nano letters*, vol. 5, no. 9, pp. 1814–1818, 2005.

[164] R. Marsh, C. Groves, and N. Greenham, "A microscopic model for the behavior of nanostructured organic photovoltaic devices," *Journal of Applied Physics*, vol. 101, no. 8, p. 083509, 2007.

[165] L. Meng, Y. Shang, Q. Li, Y. Li, X. Zhan, Z. Shuai, R. G. Kimber, and A. B. Walker, "Dynamic Monte Carlo simulation for highly efficient polymer blend photovoltaics," *The Journal of Physical Chemistry B*, vol. 114, no. 1, pp. 36–41, 2009.

[166] M. Casalegno, G. Raos, and R. Po, "Methodological assessment of kinetic Monte Carlo simulations of organic photovoltaic devices: The treatment of electrostatic interactions," *The Journal of chemical physics*, vol. 132, no. 9, p. 094705, 2010.

[167] P. P. Ewald, "Die Berechnung optischer und elektrostatischer Gitterpotentiale," *Annalen der Physik*, vol. 369, no. 3, pp. 253–287, 1921.

[168] T. Albes, B. Popescu, D. Popescu, M. Loch, F. Arca, and P. Lugli, "Kinetic Monte Carlo modeling of low-bandgap polymer solar cells," in *Photovoltaic Specialist Conference (PVSC), 2014 IEEE 40th*. IEEE, 2014, pp. 0057–0062.

[169] T. Albes, B. Popescu, D. Popescu, F. Arca, and P. Lugli, "Optimization of organic solar cells by kinetic Monte Carlo simulations," in *Nanotechnology (IEEE-NANO), 2014 IEEE 14th International Conference on*. IEEE, 2014, pp. 1023–1028.

[170] C. Groves, R. G. Kimber, and A. B. Walker, "Simulation of loss mechanisms in organic solar cells: A description of the mesoscopic Monte Carlo technique and an evaluation of the first reaction method," *The Journal of chemical physics*, vol. 133, no. 14, p. 144110, 2010.

[171] C. W. Tang, "Two-layer organic photovoltaic cell," *Applied Physics Letters*, vol. 48, no. 2, pp. 183–185, 1986.

[172] G. Yu, J. Gao, J. Hummelen, F. Wudl, and A. Heeger, "Polymer photovoltaic cells: enhanced efficiencies via a network of internal donor-acceptor heterojunctions," *Science-AAAS-Weekly Paper Edition*, vol. 270, no. 5243, pp. 1789–1790, 1995.

[173] G. Li, V. Shrotriya, J. Huang, Y. Yao, T. Moriarty, K. Emery, and Y. Yang, "High-efficiency solution processable polymer photovoltaic cells by self-organization of polymer blends," *Nature materials*, vol. 4, no. 11, pp. 864–868, 2005.

[174] W. Ma, C. Yang, X. Gong, K. Lee, and A. J. Heeger, "Thermally stable, efficient polymer solar cells with nanoscale control of the interpenetrating network morphology," *Advanced Functional Materials*, vol. 15, no. 10, pp. 1617–1622, 2005.

[175] A. Miller and E. Abrahams, "Impurity conduction at low concentrations," *Physical Review*, vol. 120, no. 3, p. 745, 1960.

[176] B. C. Thompson and J. M. Fréchet, "Polymer–fullerene composite solar cells," *Angewandte Chemie International Edition*, vol. 47, no. 1, pp. 58–77, 2008.

[177] E. Von Hauff, V. Dyakonov, and J. Parisi, "Study of field effect mobility in PCBM films and P3HT: PCBM blends," *Solar energy materials and solar cells*, vol. 87, no. 1, pp. 149–156, 2005.

[178] M. Lenes, M. Morana, C. J. Brabec, and P. W. Blom, "Recombination-Limited Photocurrents in Low Bandgap Polymer/Fullerene Solar Cells," *Advanced Functional Materials*, vol. 19, no. 7, pp. 1106–1111, 2009.

[179] H. Hoppe and N. S. Sariciftci, "Organic solar cells: An overview," *Journal of Materials Research*, vol. 19, no. 07, pp. 1924–1945, 2004.

[180] G. Dennler, M. C. Scharber, and C. J. Brabec, "Polymer-Fullerene Bulk-Heterojunction Solar Cells," *Advanced Materials*, vol. 21, no. 13, pp. 1323–1338, 2009.

[181] S. Günes, H. Neugebauer, and N. S. Sariciftci, "Conjugated polymer-based organic solar cells," *Chemical reviews*, vol. 107, no. 4, pp. 1324–1338, 2007.

[182] P. Peumans, A. Yakimov, and S. R. Forrest, "Small molecular weight organic thin-film photodetectors and solar cells," *Journal of Applied Physics*, vol. 93, no. 7, pp. 3693–3723, 2003.

[183] M. Von Smoluchowski, "Zur kinetischen Theorie der brownschen Molekularbewegung und der Suspensionen," *Annalen der physik*, vol. 326, no. 14, pp. 756–780, 1906.

[184] I.-W. Hwang, D. Moses, and A. J. Heeger, "Photoinduced carrier generation in P3HT/PCBM bulk heterojunction materials," *The Journal of Physical Chemistry C*, vol. 112, no. 11, pp. 4350–4354, 2008.

[185] C. J. Brabec, N. S. Sariciftci, J. C. Hummelen *et al.*, "Plastic solar cells," *Advanced Functional Materials*, vol. 11, no. 1, pp. 15–26, 2001.

[186] U. Wolf, V. Arkhipov, and H. Bässler, "Current injection from a metal to a disordered hopping system. I. Monte Carlo simulation," *Physical Review B*, vol. 59, no. 11, p. 7507, 1999.

[187] F. Yang, K. Sun, and S. R. Forrest, "Efficient Solar Cells Using All-Organic Nanocrystalline Networks," *Advanced Materials*, vol. 19, no. 23, pp. 4166–4171, 2007.

[188] D. J. Griffiths and R. College, *Introduction to electrodynamics*. Prentice hall Upper Saddle River, NJ, 1999, vol. 3.

[189] J. D. Jackson and J. D. Jackson, *Classical electrodynamics*. Wiley New York etc., 1962, vol. 3.

[190] J. Grotendorst, D. Marx, and A. Muramatsu, "Quantum Simulations of Complex Many-Body Systems: From Theory to Algorithms," *NIC Series*, vol. 10, 2002.

[191] A. J. Heeger, "Nobel Lecture: Semiconducting and metallic polymers: The fourth generation of polymeric materials," *Reviews of Modern Physics*, vol. 73, no. 3, pp. 681–700, 2001.

[192] T. Albes, *Kinetic Monte Carlo Modeling of Bulk-Heterojunction Organic Solar Cells*. unpublished.

[193] E. Ising, "Beitrag zur theorie des ferromagnetismus," *Zeitschrift für Physik A Hadrons and Nuclei*, vol. 31, no. 1, pp. 253–258, 1925.

[194] L. Koster, S. E. Shaheen, and J. C. Hummelen, "Pathways to a new efficiency regime for organic solar cells," *Advanced Energy Materials*, vol. 2, no. 10, pp. 1246–1253, 2012.

List of Publications

[1] D. Popescu, B. Popescu, G. Jegert, S. Schmelzer, U. Boettger, and P. Lugli, "Kinetic Monte Carlo Simulation of $SrRuO_3/SrTiO_3/SrRuO_3$ Thin Film Capacitors," *Electron Devices, IEEE Transactions on*, SUBMITTED.

[2] B. Popescu, D. Popescu, and P. Lugli, "Full Band 3D Monte Carlo Simulation of InAs Nanowires and High Frequency Analysis," *Electron Devices, IEEE Transactions on*, vol. 62, no. 6, pp. 1848–1854, June 2015.

[3] T. Albes, B. Popescu, D. Popescu, F. Arca, and P. Lugli, "Optimization of Organic Solar Cells by Kinetic Monte Carlo Simulations," in *International Conference on Nanotechnology (NANO), 2014 IEEE 14th*, August 2014.

[4] K. Melzer, M. Brandlein, B. Popescu, D. Popescu, P. Lugli, and G. Scarpa, "Characterization and simulation of electrolyte-gated organic field-effect transistors," *Faraday Discuss.*, pp. –, 2014. [Online]. Available: http://dx.doi.org/10.1039/C4FD00095A

[5] T. Albes, B. Popescu, D. Popescu, M. Loch, F. Arca, and P. Lugli, "Kinetic Monte Carlo modeling of low-bandgap polymer solar cells," in *Photovoltaic Specialist Conference (PVSC), 2014 IEEE 40th*, June 2014, pp. 0057–0062.

[6] D. Popescu, B. Popescu, G. Jegert, S. Schmelzer, U. Boettger, and P. Lugli, "Feasibility Study of $SrRuO_3/SrTiO_3/SrRuO_3$ Thin Film Capacitors in DRAM Applications," *Electron Devices, IEEE Transactions on*, vol. 61, no. 6, pp. 2130–2135, June 2014.

[7] B. Popescu, D. Popescu, and P. Lugli, "Modeling and High-Frequency Simulation of InAs Nanowires," *Nanotechnology, IEEE Transactions on*, vol. 13, no. 4, pp. 850–856, July 2014.

[8] D. Popescu, B. Popescu, P. Lugli, C. Varone, and W. Jiang, "Effect of morphology on the performance of organic solar cells," in *Nanotechnology (IEEE-NANO), 2013 13th IEEE Conference on*, Aug 2013, pp. 258–261.

[9] B. Popescu, D. Popescu, P. Lugli, S. Locci, F. Arca, S. Tedde, M. Sramek, and O. Hayden, "Modeling and Simulation of Organic Photodetectors for Low Light Intensity Applications," *Electron Devices, IEEE Transactions on*, vol. 60, no. 6, pp. 1975–1981, June 2013.

[10] D. Popescu, B. Popescu, P. Lugli, and S. Locci, "A Magnetic Manipulation System Using an Active Filter for Electronic Detection of Target Cells," *Biomedical Circuits and Systems, IEEE Transactions on*, vol. 6, no. 4, pp. 319–325, Aug 2012.

[11] L. Roselli, F. Alimenti, M. Virili, F. Lolli, B. Popescu, D. Popescu, S. Locci, and P. Lugli, "Feasibility study of a fully organic frequency doubler for harmonic RFID applications," in *Silicon Monolithic Integrated Circuits in RF Systems (SiRF), 2012 IEEE 12th Topical Meeting on*, Jan 2012, pp. 203–206.

[12] G. Jegert, D. Popescu, P. Lugli, M. J. Häufel, W. Weinreich, and A. Kersch, "Role of defect relaxation for trap-assisted tunneling in high-κ thin films: A first-principles kinetic Monte Carlo study," *Phys. Rev. B*, vol. 85, p. 045303, Jan 2012. [Online]. Available: http://link.aps.org/doi/10.1103/PhysRevB.85.045303

Acknowledgments

The possibility and success of this work would not have been likely without the trust, patience and support of several individuals and organizations. I hereby thank all those who contributed to this work in any way.

Special thanks goes to:

- Prof.Dr. Paolo Lugli for his cooperation and support for allowing me to conduct this thesis under his supervision. His continuous valuable advices had a great contribution in the success of this work
- Mrs Lucia Weik for her kind cooperation in many administrative issues
- TUM International Graduate School for Science and Engineering and TUM Institute of Advanced Study for their partial financial support

Furthermore, I want to express my gratitude to my friends Simone Colasanti, Tim Albes, Aniello Falco, Engin Cagatay, Florin Loghin, Katharina Melzer, Bernhard Fabel, Farook Mokhtar, Alaa Abdellah and Ahmed Abdelhalim for their company and emotional support throughout the study period.
Finally, I would like to thank my family for their continuous support.